Advances in Cd and Fe isotope cosmochemistry

I n a u g u r a l - D i s s e r t a t i o n

zur

Erlangung des Doktorgrades

der Mathematisch-Naturwissenschaftlichen Fakultät

der Universität zu Köln

vorgelegt von

Victoria Elisabeth Zippmann

aus Eisenstadt

Köln, 2019

Advances in Cd and Fe isotope cosmochemistry

I n a u g u r a l - D i s s e r t a t i o n

zur

Erlangung des Doktorgrades

der Mathematisch-Naturwissenschaftlichen Fakultät

der Universität zu Köln

vorgelegt von

Victoria Elisabeth Zippmann

aus Eisenstadt

Köln, 2019

Gutachter:	Prof. Dr. Carsten Münker
	Dr. Daniel Herwartz
Tag der mündlichen Prüfung:	29.04.2019

“WITH YOUR MIND POWER,

YOUR DETERMINATION,

YOUR INSTINCT,

AND THE EXPERIENCE AS WELL,

YOU CAN FLY VERY HIGH.”

— Ayrton Senna

Content

Abstract

The question about how our solar system was formed is central in cosmochemistry. Within this thesis, I follow two different approaches that relate to this central question. First, mass-dependent Cd stable isotope fractionation was studied experimentally in order to improve our understanding of the stable isotope fractionation effects associated with evaporation and condensation processes. A thorough understanding of such stable isotope effects is required to interpret natural variations, for example in meteorites. Second, Fe isotope compositions were studied in chondrite leachates and residues at high precision in order to reveal potential isotope heterogeneities due to the uneven distribution of materials with different stellar origins within chondrite samples as well as on the planetary scale.

To investigate volatile element stable isotope effects related to evaporation and condensation under reduced and oxidized conditions, two experiments were implemented, experiment 1 in CO-CO_2 and experiment 2 in air. Samples were taken from evaporating silicate melts at the bottom of a furnace tube and from plates placed on the furnace wall where Cd vapor recondensed. Cadmium was separated from evaporation and condensation samples and analyzed using MC-ICPMS. For $^{114}Cd/^{110}Cd$ measurement precision (2 s.d.) was ±0.03 ‰. Results show that the loss of volatile elements during evaporation can proceed with neglectable isotope fractionation under reduced conditions. It is assumed that in experiment 1, the isotope fractionation is suppressed by a saturated boundary layer on top of the melt surface. Back reaction of evaporated material with the melt occurs and equilibrated material evaporates from the layer. Samples leached from condensation plates reveal an enrichment of light Cd isotopes closer to the melt surface and an enrichment of heavier Cd isotopes at the top of the plates. As expected from their higher collision frequency due to their higher velocity, the light Cd isotopes condensed preferentially. In experiment 2, the fractionation factor is in good agreement with what is expected from purely kinetic condensation. In experiment 1, it is likely that back reaction altered the fractionation.

Deviations from terrestrial isotope ratios in solar system materials such as meteorites are called nucleosynthetic anomalies and can be detected via high-precision isotope analyses Since Fe isotope measurements increased in precision over the last decades, high-precision MC-ICP-MS Fe isotope analyses of chondritic material were implemented in this thesis. Leachates and residues of six different bulk chondrites and bulk rock samples were analyzed for their Fe

isotope composition with a measurement precision (2 s.d.) of 13 ppm for $^{56}Fe/^{54}Fe$ and 16 ppm for $^{58}Fe/^{54}Fe$. No nucleosynthetic Fe isotope anomalies were found in the analyzed samples. In contrast to homogenous Fe, other Fe-peak elements like Cr or Ti show nucleosynthetic anomalies on the bulk rock scale and planetary scale. Theories to explain this phenomenon are 1) secondary redistribution of anomalous refractory Fe-peak element carrier phases beside less refractory Fe carrier phases which could not survive high-temperature events and got homogenously mixed throughout the solar system as gas, or 2) an initially homogeneous molecular cloud or protosolar disk into which anomalous material was injected and heterogeneously distributed, while Fe is carried by thermally unstable phases that evaporated and mixed homogeneously throughout the solar system. A small amount of anomalous Fe in rare grains survived high-temperature events but cannot be detected on bulk rock scale due to the mass budget of Fe in the solar system.

Kurzzusammenfassung

Eine zentrale Frage in der Kosmochemie ist die, nach der Entstehung unseres Sonnensystems. In dieser Arbeit zeige ich zwei verschiedene Herangehensweisen auf, die sich auf diese zentrale Frage beziehen. Zuerst wurden massenabhängige stabile Cd-Isotopenfraktionierungen experimentell untersucht, um ein besseres Verständnis für die Fraktionierung stabiler Isotope in Verbindung mit Verdampfung und Kondensation zu erlangen. Ein umfassendes Verständnis für diese Isotopeneffekte ist notwendig um natürliche Variationen, wie zum Beispiel in Meteoriten, zu interpretieren. Als zweites wurden hoch-präzise Analysen der Fe-Isotopenzusammensetzungen von Säureauszügen und Residuen von Chondriten untersucht, um potenzielle Isotopen-Heterogenitäten aufgrund von ungleicher Verteilung von Material mit unterschiedlicher stellarer Herkunft in Chondrit-Proben und auf planetarer Ebene zu beleuchten.

Um die Effekte in stabilen Isotopen flüchtiger Elemente bei Verdampfung und Kondensation unter reduzierenden und oxidierenden Bedingungen untersuchen zu können, wurden zwei Experimente durchgeführt, Experiment 1 in CO-CO_2 und Experiment 2 in Luft. Es wurden abdampfende Silikatschmelzen, die am Boden eines Rohrofen platziert waren, und an der Ofenwandung platzierte Kondensationsplatten beprobt, an welchen Cadmiumdampf kondensiert ist. Cadmium wurde von den Schmelzproben sowie den Kondensaten chemisch abgetrennt und mittels MC-ICP-MS analysiert. Für $^{114}Cd/^{110}Cd$ wurde eine Messgenauigkeit (2 s.d.) von ±0.03 ‰ erreicht. Die Ergebnisse zeigen, dass der Verlust flüchtiger Elemente durch Verdampfung in reduzierendem Gas mit nur vernachlässigbar geringer Isotopenfraktionierung auftreten kann. Es wird angenommen, dass die Isotopenfraktionierung in Experiment 1 durch eine Cd-Dampf gesättigte Grenzschicht auf der Oberfläche der Schmelze unterdrückt wird. Die mit Säure aus den Kondensationsplatten geätzten Proben zeigen eine Anreicherung von leichten Cd-Isotopen nahe der Schmelzoberfläche und eine Anreicherung von schweren Cd-Isotopen am oberen Ende der Platten. Aufgrund der höheren Geschwindigkeit der leichten Isotope ist ihre Kollisionsfrequenz höher und sie kondensieren somit bevorzugt. Der Fraktionierungsfaktor aus Experiment 2 zeigt eine rein kinetische Kondensation an. In Experiment 1 verringern vermutlich Rückreaktionen die Isotopenfraktionierung.

Deutliche massenunabhängige Abweichungen von terrestrischen Isotopenverhältnissen in Materialien des Sonnensystems, wie zum Beispiel Meteoriten, werden als nukleosynthetische

Anomalien bezeichnet und können über hochpräzise Isotopenanalysen nachgewiesen werden. Da die Fe-Isotopenanalyse in den letzten Jahrzehnten an Präzision gewann, wurden in dieser Arbeit hochpräzise MC-ICP-MS Fe-Isotopenanalysen an chondritischem Material durchgeführt. Es wurde die Fe-Isotopie von Säureauszügen und Residuen von sechs verschiedenen Chondriten und Gesamtgesteinsproben analysiert und dabei eine Messgenauigkeit (2 s.d.) von 13 ppm für $\mu^{56}Fe/^{54}Fe$ und 16 ppm für $\mu^{58}Fe/^{54}Fe$ erreicht. In den untersuchten Proben konnten keine nukleosynthetischen Fe-Isotopenanomalien nachgewiesen werden. Andere Fe-Peak Elemente wie Cr oder Ti weisen, im Gegensatz zum homogenen Fe, sowohl auf der Gesamtgesteinsebene als auch auf planetarer Ebene nukleosynthetische Isotopenanomalien auf. Theorien zur Erklärung dieses Phänomens sind 1) die sekundäre Umverteilung von isotopisch anomalen refraktären Fe-Peak Element-Trägerphasen, während weniger refraktäre Fe-Trägerphasen Hochtemperaturereignisse nicht überstehen konnten und in der Gasphase homogen im Sonnensystem verteilt wurden, oder 2) eine initial homogene Molekülwolke oder protosolare Scheibe, in welche isotopisch abweichendes Material eingebracht und heterogen verteilt wurde. Dieses anomale Material müsste an Fe verarmt sein um aufgrund des Fe-Massenbudgets nicht im Sonnensystem nachweißbar zu sein, oder es wäre in thermisch unstabilen Phasen gebunden, die während Hochtemperaturphasen verdampften und homogen im Sonnensystem verteilt wurden.

I. Introduction

1. EVOLUTION OF A STAR AND THE SYNTHESIS OF ELEMENTS

1.1. Star formation

In the interstellar medium (ISM), cold areas (~7-15 K) of gas and dust, with densities that exceed the point where the formation of molecules is possible (~10^3 – 10^5 mol cm^{-3}), are called molecular clouds. They mainly consist of molecular hydrogen, helium and molecules like CO (Boss and Ciesla, 2013). Areas with the highest densities in these clouds represent the earliest evolutionary stage of a stellar system (Alexander, 2001). Materials in the ISM from which the solar system formed are assemblages of debris from different stars born in different molecular clouds at different times (Busso et al., 1999). High-density regions in molecular clouds are the only place in the universe where stars can be formed. When the mass of the dense region reaches the Jeans mass (Jeans, 1902), which is a certain value depending on temperature and density, the hydrostatic equilibrium becomes unstable. The potential energy of the gravitational force exceeds the kinetic energy of the internal gas pressure hence the cloud undergoes gravitational collapse. Also, compression of dense molecular cloud regions due to cloud collisions or shock waves from nearby supernova explosions can trigger a molecular cloud collapse.

A rotating core, that evolves towards hydrostatic equilibrium, arises which represents the first stage of a protostar and is surrounded by a dense accretion disc (McSween and Huss, 2010). The newly formed young protostar has an initial size of about 1-10 AU and accretes infalling material while its temperature increases (Boss and Ciesla, 2013; Goodwin, 2013). Processes within the accretion disk and ejection of material from the protostar via bipolar outflows (jets) are mechanisms by which angular momentum is removed from the system, aiding accretion of the protostar (McSween and Huss, 2010). Thermal energy prevents a collapse of the protostar due to its mass and density (Goodwin, 2013). When the core temperature reaches ~ 2000 K, enough energy is available to dissociate molecular hydrogen. The temperature drops and causes a rapid collapse of the protostar to stellar density. Further dissociation of all molecular hydrogen, further accretion of surrounding cloud material and an increasing central density and temperature due to contraction leads to ignition of hydrogen fusion reactions and completes the formation of the star. This path does not apply for brown dwarfs. They can only reach a mass of $\geq 0.8\ M_{\odot}$ and are unable to ignite the nuclear fusion of hydrogen.

1.2. Stellar evolution and burning stages

The mass of a star determines its evolutionary path and life span. After the ignition of hydrogen burning in the core, the star joins the main sequence of the Hertzsprung-Russell diagram (HRD) (Figure 1.1, Australia Telescope National Facility, n.d.).

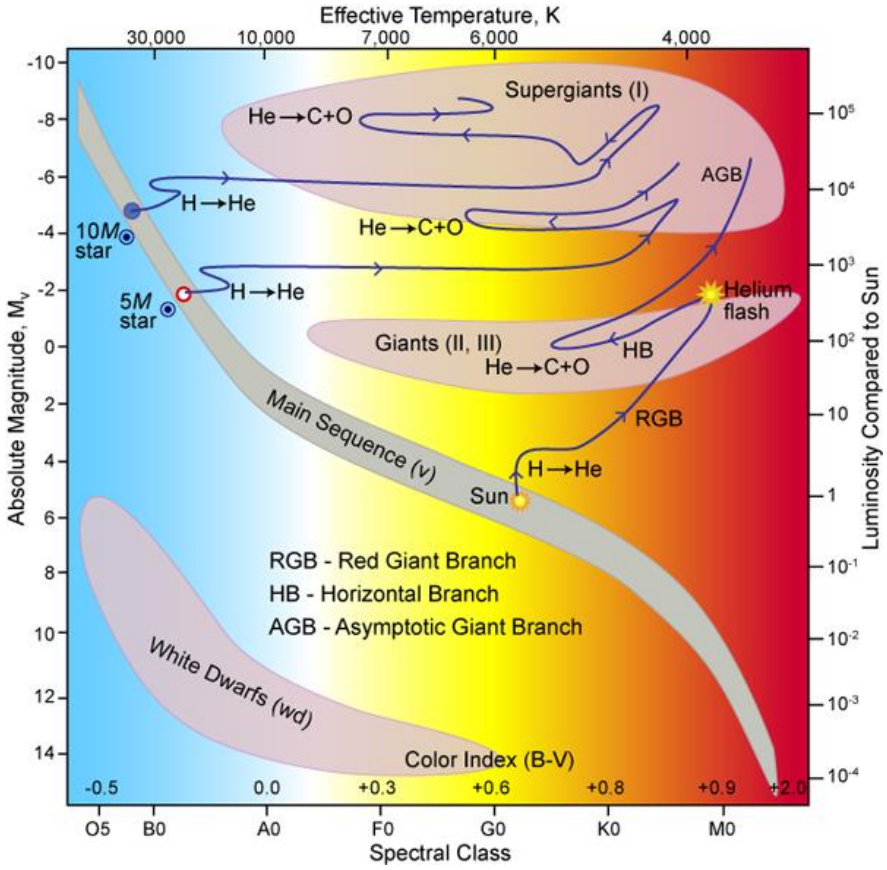

Figure 1.1. Hertzsprung-Russell diagram showing the post-main sequence evolutionary tracks of stars with 10 $M_\odot$, 5 $M_\odot$ and 1 $M_\odot$. The fusion of H into He in the core is the first burning stage of a star. It is dependent on solar mass, how far a star can evolve before its life ends. Figure taken from Australia Telescope National Facility (n.d.).

Due to the ignition of nuclear fusion of hydrogen, helium is produced from the reaction of four hydrogen atoms to form ^{4}He. This fusion reaction is exothermic and represents the main source of nuclear energy in the Sun (McSween and Huss, 2010). When all hydrogen in the star's core is fused to helium, thus exhausted, the core contracts and heats up due to compression. This leads to a further hydrogen fusion in the zone around the helium core and establishes a burning shell around the hydrogen-depleted core. Due to increasing thermal pressure the shell expands, cools on the outside, and turns the star into a red giant. Due to a rising core temperature, helium fusion ignites, further contraction stops and the balance between thermal pressure and

gravitational compression is established again. Three ^{4}He atoms (α-particles) react to ^{12}C (and four to ^{16}O) in the core until exhaustion of helium. A star with a solar mass < ~10 $M_{\odot}$ evolves to an AGB star, undergoes the process described in chapter II/3.1.3. and ends up as a white dwarf (Figure 1.2, NASA Jet Propulsion Laboratory (n.d.)). If the star has a mass > ~10 $M_{\odot}$, the process of contraction and heating, as described above, reoccurs including a new ^{4}He-burning shell. Subsequently, fusion of ^{12}C ignites, resulting in ^{24}Mg, ^{20}Ne and ^{16}O production in the core. This burning stage lasts until exhaustion of carbon and the formation of another burning shell from products produced outside the core. It follows the Ne-burning stage where mainly ^{28}Si, ^{16}O and ^{24}Mg are produced. Then oxygen reacts with itself during the O-burning stage, producing ^{28}Si and ^{32}S. In the final burning stage, main nucleosynthesis is driven by photodisintegration which ejects α-particles, protons and neutrons from stable nuclei. Free particles are then consumed by the production of various nuclei up to the mass of iron. Nuclei much heavier than iron cannot be produced via exothermic fusion reactions. The Si-burning stage lasts about one day until the star's life ends due to disintegration of iron in the core followed by a core collapse which induces a shock wave. The result is a supernova that ejects material into the interstellar medium (ISM). Depending on the initial stellar mass, a black hole, a neutron star or only gas and dust without a remnant remains after the explosion (Figure 1.2) (see chapter II/1.1).

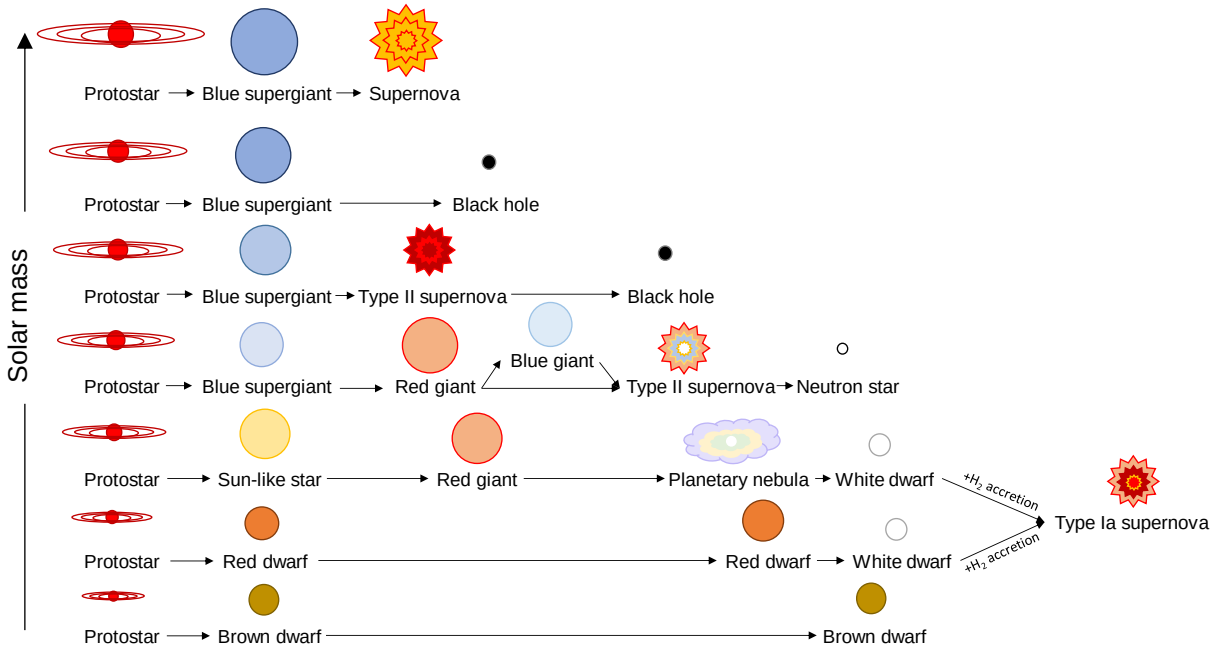

Figure 1.2. Evolution of a star depending on its solar mass. Graphic adapted and redrawn after NASA Jet Propulsion Laboratory (n.d.).

2. FORMATION OF THE SOLAR SYSTEM

Our solar system (Figure 1.3 after Shipman et al. (2012)) formed 4.57 Ga years ago (Scherstén et al., 2006; Bouvier and Wadhwa, 2010) from the rotating accretion disk consisting of dust and gas that surrounded a protostar which evolved to our sun (Boss and Ciesla, 2013).

Figure 1.3. Solar system objects with their distance to the sun to scale using data by Shipman et al. (2012).
1 AU = 149597801,7 km (International Astronomical Union, 2012)

The protosolar accretion disk underwent a thermodynamical and cosmochemical evolution which is not fully understood to this day due to complex chemical and physical observations in solar material that still need to be explained. However, astrophysical observations of young stellar objects and theoretical models can provide a consistent image of processes that have probably occurred during the formation of our solar system which help to align results of this study with presumed events.

Once, a protostar has formed after the collapse of a molecular cloud, when it has accreted most of the circumstellar cloud material, the accretion disk around the protostar evolves into a protoplanetary disk or *solar nebula*.

Temperatures in the solar nebula decrease and gas can condense into dust, ice and first refractory mineral aggregates (CAIs and AOAs, see section I.3). Due to the texture found in certain meteoritic components, flash heating events have to occur to rapidly produce a high density of melt droplets from dust grains and partly evaporate a significant amount of molten refractory dust clumps (McSween and Huss, 2010). The melt droplets crystallize into silicate-rich spherical *chondrules* during a very short cooling time of about several hours. Presumably, the process of melting and subsequent crystallisation takes place without losing significant amounts of volatile elements or showing isotopic mass fractionation associated with evaporation (Alexander et al., 2008). This implies that chondrules form in large swarms where

the solid-to-gas ratio is several orders of magnitude higher than in the solar nebula as a whole (Chambers, 2013). Chondrules are a dominant constituent of most chondrites (see section 3), albeit the process and conditions responsible for chondrule formation are still not understood to this date.

On a larger scale, evaporation of volatiles due to high temperature occurs at low distance to the sun, thus refractory solids are enriched in the inner area of the solar nebula. In comparison, outer areas of the solar nebula contain more condensed volatile elements and average gas pressure is lower than at smaller distance to the sun (Chambers, 2013). However, the enrichment of volatile elements in planets or meteorites in the outer solar system does not balance the depletion, thus it remains a volatile element depletion in the bulk solar system (Palme et al., 1988). The border that marks the transition from gaseous to frozen water along the temperature gradient from the center of the solar nebula to its outer rim, is called *snow line*. The radius of this snow line has possibly decreased over time due to a decrease in luminosity of the protosun, the gas mass accretion rate and evolution of icy dust particles due to grain growth and fragmentation (Piso et al., 2016). When the snow line reaches a distance of 5 AU or perhaps less, the large amount of condensed silicates and water ice collide and accrete to bigger chunks of solids. Due to turbulent motions within the solar nebula, water vapor is carried outwards and enriches the area beyond the snow line with ice (Stevenson and Lunine, 1988). Gas drag carries boulder-sized bodies inwards and may bring large amounts water-rich material into the planet-forming area which could affect the oxidation state of the nebular gas and modify the decline of water vapor inward the snow line (Lunine, 2006).

Turbulences also occur close to the star due to ionized gas that is coupled to the local magnetic field (Hawley et al., 1995). At an intermediate distance to the star, dust grains absorb charged particles, thus neutralize the magnetic field (Gammie, 1996; Matsumura and Pudritz, 2006). This reduces turbulences and provides an environment where disk material may accumulate (Chambers, 2013). If collisional accumulation is efficient and rapid, precursors of planets, so-called *planetesimals*, can grow from smaller particles (Supulver and Lin, 2000). They are no longer affected by turbulences but grow to planets due to runaway growth caused by their gravity.

Beside the formation of planets, the asteroid belt forms at a radius of 2-3 AU. In this area, it has been suggested that Jupiter's growing gravity causes turbulences too strong for planet formation to occur and may have removed about 99% of initial material in the belt (McSween and Huss, 2010). According to the Grand Tack hypothesis, the early inward and then outward migration

of Jupiter removed much mass from the asteroid belt which also explains the small size of Mars (Walsh et al., 2011). The asteroid belt is the main source of meteoritic material on Earth. Parent bodies of meteorites which have not undergone melting and differentiation, still contain - to a certain degree - primitive material left over from the early solar nebula. Undifferentiated and unequilibrated primitive meteorites (chondrites, see below) also contain *presolar grains*, material that survived as sub-µm-sized grains, coming from a stellar source older than our solar system.

At a later stage, when the sun ejects massive stellar winds during its evolution, most of the gas and small dust particles are blown outwards of the solar nebula, thus are removed from the system if not already fallen onto the star (Boss and Ciesla, 2013). In the timescale of several million years after the formation of the protostar, the lifetime of the surrounding disk ends (Calvet et al., 1999) to become a planetary system around the sun (Figure 1.3). There, the differentiated planets undergo several giant impacts like the putative Moon-forming event, which lead to the exchange of material with colliding objects or losing mantle material (thereby explaining the high density of Mercury) (Chambers, 2013).

3. CHONDRITES AND THEIR COMPONENTS

Chondrites are meteorites that originate from parent bodies that did not undergo differentiation since their formation in the early solar nebula. They represent the most primitive material in the solar system and are composed of different components (e.g. refractory inclusions, chondrules, matrix, and metal, cf. Figure 1.4, Hezel (2014)) formed at different times and each with its own previous history (Busso et al., 1999). Because the material of chondrites is well preserved and did not undergo differentiation, they often contain small grains from a source different from what was the origin of the solar nebula. These so-called *presolar grains* stand out from solar material with highly variable isotopic pattern that cannot be explained by processes within our solar system.

About 86 % of meteorites are chondrites and are organized in classes – carbonaceous (C), ordinary (O), and enstatite (E) chondrites – and chemical groups, using bulk chemical composition and petrological types considering aqueous alteration (type 1-2) or thermal metamorphism (type 3-6) (Table 1.1) (McSween and Huss, 2010).

Table 1.1. Chondrite classification adapted from McSween and Huss (2010) and Van Schmus and Wood (1967)

Carbonaceous chondrites (CC)	**Ordinary chondrites* (OC)**	**Enstatite chondrite** (EC)**	Rumuruti chondrites	Kakangari chondrite
CI (1)	H (3-6)	EH (3-6)	R (3-4)	K (3)
CM (1-2)	L (3-6)	EL (3; 5-6)		
CR (1-3)	LL (3-6)			
CB (3)				
CH (3)				
CV (3)				
CO (3)				
CK (3-6)				

*H: high Fe; L: low Fe; LL: low Fe, low metal

**EH: high Fe; EL: low Fe

Carbonaceous chondrite groups are not closely related and reflect different compositions, oxidation states and petrography. The second letter in their name is the first letter of the type

meteorite, representing the group, except H in CH stands for high Fe. CI chondrites show a relative element abundance similar to that of the solar photosphere, except for atmophile elements such as H, He, O, C, N and noble gases. In other primitive chondrites, the abundances of moderately volatile elements (elements with condensation temperatures in the range of 650 to 1350 K) are depleted relative to CI chondrites (Wasson and Kallemeyn, 1988). CI chondrites do not contain chondrules and are enriched in presolar grains. All other chondrites contain chondrules which can comprise up to 80 % of the total chondrite mass (Jones et al., 2000).

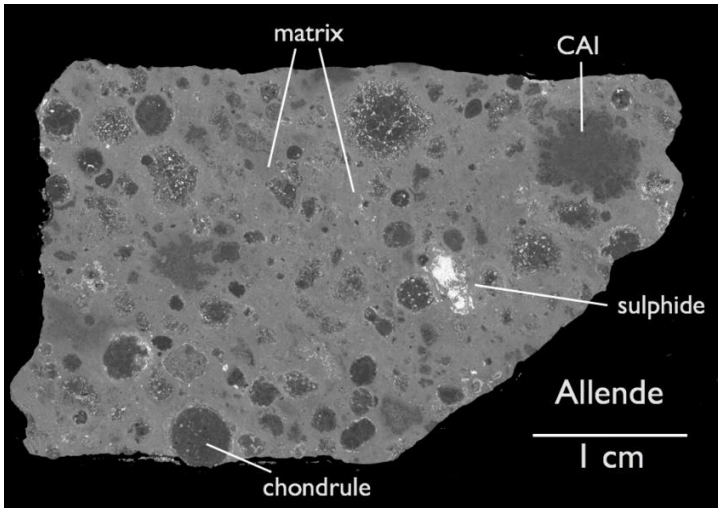

Figure 1.4. Back Scattered Electron (BSE) image of the CV chondrite Allende by Hezel (2014).

3.1. Chondrules

The origin and building processes of chondrules still lack a clear explanation and are major topics in cosmochemistry. Theoretical models suggest that, considering the composition and texture of chondrules, their precursor material, presumably dust, must have been partially or completely molten. Local high-temperature events, presumably caused by shock waves or flashes in the solar nebula, reached peak temperatures of about 1,700 to 2,100 K, following subsequently slow cooling at rates of 10–1,000 K/hr (Hewins et al., 1996; Alexander, 2001). The exact origin of heat sources remains unclear.

High-temperature processes such as evaporation of elements into vacuum produce isotope fractionation. Lighter isotopes of the evaporating species have higher thermal velocities and become depleted while heavy isotopes become enriched in the residual material (Lord Rayleigh, 1896). Despite volatile element depletion, only minor evidence of isotope fractionation was found in chondrules (Alexander et al., 2000). Zinc in chondrules even tends to be enriched in

light isotopes which is opposite of what would be expected from partial evaporation (Pringle et al., 2017).

A majority of chondrules is porphyritic, composed of olivine, pyroxene and glass. They are usually sized on a µm to millimeter scale with an average diameter of 500 µm (e.g. Friedrich et al., 2015) and can show igneous or dust rims and zonation (Hewins et al., 2005; Simon et al., 2018). The high abundance of chondrules in chondrites points to several episodes of chondrule formation events, that produced several generations of spherules (Cuzzi and Alexander, 2006). The size-range of chondrule subtypes within a chondrite is restricted and has been explained by size sorting processes within the solar nebula before the accretion of parent bodies (Simon et al., 2018).

3.2. Refractory Inclusions

CAIs (*Calcium-Aluminium-rich Inclusions*) are refractory components of chondrites and provide the oldest dated material formed in the solar nebula. They formed about 4567-4568 Ma ago, thus define an absolute age of the solar system (Amelin et al., 2010; Bouvier and Wadhwa, 2010). They are 1-2 million years older than chondrules and much less abundant. CAIs are almost entirely made of MgO, CaO, SiO_2, Al_2O_3 and a small amount of TiO_2 (Richter et al., 2011). Fine-grained minerals with irregular shapes in CAIs reflect what would condense from a cooling gas of solar composition and therefore, about one third of them are assumed to have directly condensed from the solar gas phase cooled to about 1300 K at a total pressure of 10^{-5} to 10^{-3} bar (Grossman, 1972; Ebel and Grossman, 2000; McSween and Huss, 2010). Another argument for condensation as a building process of CAIs is a highly fractionated REE pattern found in about 30 % of all CAIs (Palme and Boynton, 1993; Scott and Krot, 2013). Some CAIs show textures characteristic for melt crystallisation and are more coarse-grained and compact (McSween and Huss, 2010). There are also arguments supporting evaporation as formation process for CAIs, like the preservation of large isotopic anomalies in platy hibonite crystals found in CM chondrites, the lack of ^{26}Al, mass fractionation effects and smaller nuclear anomalies in inclusions with unknown nuclear effects (FUN). Hence CAIs were either formed by condensation from a gas of solar composition or by evaporation of chondritic material (Palme and Boynton, 1993; Scott and Krot, 2013).

The environment in which CAIs formed is assumed to be dominated by low oxygen fugacity, thus a very reducing atmosphere (Beckett et al., 1988). Mineralogy and isotope chemistry vary between chondrite groups, which could be explained by multiple CAI-forming events under

variable conditions and a separation of CAIs from the system after formation (Scott and Krot, 2013). CAIs can bear nucleosynthetic anomalies from incorporated presolar grains. The highest abundance (3 vol.% Hezel et al., 2008) of CAIs is found in CV chondrites.

3.3. Matrix

The matrix material of chondrites fills the gaps between chondrules, refractory inclusions and metal grains and consists of fine-grained disequilibrium assemblage of various minerals (amorphous phases, crystalline FeO-rich silicates, oxides, sulfides, phyllosilicates (Friend et al., 2018)) which are, according to the petrological type of the chondrite, more or less aqueously or thermally altered. With the degree of alteration varies the abundance of presolar grains in the matrix. Matrix material is richer in volatiles than other chondrite components (McSween and Huss, 2010) with an almost chondritic composition apart from a FeO abundance which is higher than in chondrules and can make up 5 to 50 vol.% of the bulk chondrite. Sizes of matrix minerals usually range from 50 to 100 nm and with up to 95 vol.%, CI chondrites show the highest amount of matrix material (Greshake et al., 2002; Scott and Krot, 2013).

3.4. Presolar grains

Presolar grains are found in primitive chondrites and are older than the solar system. Their isotopic signatures differ from every known solar system material. The large isotopic variations, which can span several orders of magnitude, cannot be explained by chemical or physical fractionation. Presolar grains are condensates from stellar outflows/ejecta and can be assigned to certain stellar sources/supernovae by their isotopic composition (e.g. Clayton and Nittler, 2004). When they were mixed into the solar nebula or molecular cloud, they survived all thermal processes and the accretion into solar material. Types of presolar grains that have been observed so far are nanodiamonds, silicon carbides, graphite, silicates, oxides, silicon nitrides, Ti, Fe, Zr, Mo carbides and metal grains. Their size varies from 0.1 µm to 200 nm. Highest abundance of a single grain type found in a chondrite is 1400 ppm for presolar nanodiamonds (e.g. Nguyen et al., 2007; Zinner, 2013).

4. SUMMARY AND OUTLOOK

The conditions under which our solar system formed provides the overlying theme for this thesis. **Chapter I** provides essential knowledge about the processes during star formation, the evolution of a star during its lifetime and different burning stages. The chapter then gives an overview about the formation of our solar system. Since we know that chondrites represent the most primitive material in the solar system, the isotopic composition of their different components is of great interest. They reflect the conditions, for example temperature, pressure or surrounding gas, under which they have formed during the evolution of the protosolar disk into the solar system we know today.

Key questions regarding the formation of solar material are, how evaporation and condensation affected volatile element stable isotopes in solar system materials and how the mass-dependent stable isotope pattern observed in chondritic samples were generated. One approach to find answers to these questions is, to implement experiments that reflect conditions under which the solar system may have formed or allow for a better general understanding of mass-dependent stable isotope fractionation. **Chapter II** presents the study of samples gained from two evaporation and condensation experiments in which silicate material doped with 15 volatile elements was placed in a crucible on the bottom of a furnace tube. Experiment 1 was implemented in CO-CO_2 and experiment 2 in air. Because of the feasibility of advanced high precision isotope measurements and the availability of a quick and effective separation method, Cd was chosen for representing volatile element stable isotopes. Stable Cd isotopes of the melt residues and condensates were analyzed to better understand how evaporation and condensation affect the distribution of stable isotopes in the material and if or to which extent evaporation and condensation cause isotope fractionation under different atmospheres. Results show a different behavior of Cd isotopes in experiment 1 compared to experiment 2. Cadmium evaporates much faster from the melt, without showing significant isotope fractionation in experiment 1 (CO-CO_2) while in experiment 2 (air), Cd clearly shows isotope fractionation. The suppressed isotope fractionation in experiment 1 is best explained by evaporative loss via a saturated boundary layer on top of the melt surface, where back reaction of evaporated material with the melt occurs. The evaporated material condensed onto condensation plates placed on the furnace walls of which leachates were taken. Samples showed Cd isotope fractionation from “light” at the bottom to “heavy” at the top of the plates. The light isotopes

condensed preferentially as expected from their higher collision frequency. In air, the fractionation factor suggests purely kinetic condensation whereas in CO-CO_2, some back reactions seem likely.

Assuming that the solar system underwent high temperature processes like evaporation and recondensation, it arises the question, how nucleosynthetic isotope anomalies found in chondritic material, which cannot be explained e.g. via isotope fractionation or radioactive decay, were implemented and preserved during accretion of parent bodies. For a long time, the study of nucleosynthetic Fe isotope anomalies in solar material faced the problem of insufficient measurement precision. Today, an improved precision for the mass spectrometric analysis of Fe isotopes provides better resolution and can potentially reveal isotope anomalies that were not detectable before. In **Chapter III**, iron isotope analyses of chondrite leachates, residues and bulk rock samples are presented. Sequential leaching of various chondrites in acid with increasing strength was implemented to separate chondrite components of different acid resistivities from each other, thus gain a better resolution of possible isotope anomalies that would not be detectable on the bulk rock scale. Results do not show nucleosynthetic Fe isotope anomalies in bulk chondrite samples, leachates or residues in contrast to other Fe-peak elements like Cr and Ti which show various nucleosynthetic anomalies on the bulk rock scale as well as on the planetary scale. Two different theories to explain the homogeneity of iron isotopes in the solar system are evaluated. *Theory I* refers to a secondary redistribution of refractory carrier phases of Fe-peak elements such as Cr and Ti, while Fe bearing, less refractory carrier phases evaporated during high-temperature events during the formation of the solar system. This would enable Fe to remain homogeneously distributed throughout the solar system while other Fe-peak element isotopes show a dichotomy on the planetary scale due to grain-size or density sorting via turbulences, particle velocity and aerodynamic effects. *Theory II* refers to injection and heterogeneous distribution of anomalous material into an initially homogeneous molecular cloud or protosolar disk. The external source would be rich in anomalous Fe-peak elements but would have lost Fe during processes outside the solar system or would carry Fe in thermally unstable phases, that would be evaporated and homogeneously distributed in the protosolar disk as a gas phase.

Newly gained insights into mass-dependent isotope fractionation processes and the distribution of nucleosynthetic isotope anomalies in chondrites, as provided by this thesis, contribute to the steadily refining cosmochemical picture of our solar system. The constant growth of isotope data and their precision, thanks to the advances made in mass spectrometry over the past decades, leads to a better understanding but also gives rise to new questions in cosmochemistry.

To pursue what has been achieved in this thesis, further evaporation and condensation experiments using refined parameters as well as analyses of element separates from existing samples should be conducted to draw an exhaustive picture of isotope distribution in the experimental samples.

Having revealed the lack of nucleosynthetic Fe isotope anomalies in leachates and residues of various chondrites, a sequel of high precision Fe isotope analyses of further chondritic components would target the question if Fe isotopes are indeed homogeneously distributed throughout the solar system, as today's knowledge lets assume, and would help to understand in more detail how Fe isotope homogeneity was achieved.

II. Cadmium stable isotope fractionation during evaporation and condensation at atmospheric pressure

1. INTRODUCTION

The study of volatile element stable isotope fractionation associated with evaporation and condensation allows to evaluate the importance of these processes in terrestrial and extraterrestrial environments (e.g. Richter et al., 2007; Richter et al., 2009). Interpretation of such data requires a thorough understanding of isotope fractionation effects related to condensation and evaporation. Much of the theory underlying stable isotope fractionation during evaporation and condensation is well understood (e.g. Davis and Richter, 2013); see section 3) and observations on natural samples and experimental investigations have added a lot to this understanding. However, stable isotope fractionation during evaporation into an ambient atmosphere and diffusion through such an atmosphere is not well studied and disagreement exists in the literature about stable isotope fractionation related condensation (see section 3).

Here, Cd stable isotope fractionation related to the evaporation and diffusion through an ambient gas (air and CO-CO_2), and to the condensation along a temperature gradient is evaluated at atmospheric pressure using a novel experimental setup. Investigation of such volatile element stable isotope effects at atmospheric or high pressure may be relevant for studies of environmental pollution (e.g. Cloquet et al., 2006), terrestrial volcanism (e.g. Toutain et al., 2008; Baker et al., 2009; Zambardi et al., 2009) and impacts and tektite formation (Wombacher et al., 2003; Herzog et al., 2008; Moynier et al., 2009; Moynier et al., 2010) and in cosmochemistry, if higher ambient gas pressures are to be expected, e.g. inside parent bodies (cf. Wombacher et al., 2008), for the nature of the vapor disk from which the Moon may have formed (e.g. Canup et al., 2015; Wang and Jacobsen, 2016) and perhaps during chondrule formation (e.g. Galy et al., 2000).

2. EXPERIMENTAL SETUP AND METHODS

2.1. Evaporation and recondensation experiments

The experimental setup is based on the mechanically assisted equilibration (MAE) technique (Dingwell et al., 1994), modified by the addition of two Al_2O_3 condensation plates into the furnace tube (Ertel-Ingrisch and Dingwell, 2010a; Ertel-Ingrisch and Dingwell, 2010b). Experiment 1 is implemented using a CO-CO_2 mixture yielding a logfO_2 = -11.3 (IW-0.5) and experiment 2 is implemented in air with logfO_2 = -0.7 (IW+10.1), both under atmospheric pressure. During experiment 1, the CO-CO_2 gas flow rate in the furnace is set to 200 cm^3/min, while the air flow rate in experiment 2 is not actively controlled and results from the stack effect with small openings at the top and bottom of the furnace. The melt temperature corresponds to about 1580 K in both experiments. The starting material consists of 60 g of prefused glass chips from a haplo-basaltic melt composition corresponding to the 1-bar Anorthite-Diopside eutectic, which had been doped to about 3000 µg/g with 15 volatile elements (Rb, Cu, Li, Na, Ti, Cr, Mn, Cs, Cd, Tl, Sb, Zn (missing in experiment 2), K, Ga, Co, In, and Sn) plus Ti and Cr. The Cd contents of the very first sample in experiment 1 and 2 were 1680 and 3050 µg/g, respectively. Therefore, some Cd in experiment 1 was either lost already during prefusion or, more likely, during the heating phase of experiment 1 before the first sample was taken about 6 minutes after the run temperature was attained. This would result in an underestimation of the initial Cd content and an 0.28 ‰ higher $^{114}Cd/^{110}Cd$ ratio in the first sample of experiment 1 than in the first sample of experiment 2, which suggests that a small isotope fractionation effect may have been associated with this early loss. A Cd loss of 82 % recorded in the evaporation residues is evaluated in section 3. Continuous vigorous stirring with an Ir spindle maintains the homogeneity of the melts in the crucible and minimizes diffusive elemental and isotopic zonation and, hence, diffusion-limited or diffusion-related isotope fractionation. Implementation of the time series sampling involves interrupting the stirring and extracting a melt droplet with the use of an Al_2O_3 rod which is then quenched in water.

Cadmium and other volatile element vapors recondense onto two Al_2O_3 plates placed within T gradient above the crucible from ~1580 K near the melt surface to 570 K on top of the furnace tube.

2.2. Sample preparation

From each quenched glass sample, aliquots of 3 – 56 mg were ground using mortar and pestle and dissolved by tabletop digestion using HNO_3-HF followed by repeated treatment with concentrated HNO_3 and 6 M HCl. Major elements and volatile trace elements were determined on aliquots of the sample solutions. The majority of the sample solution was subjected to Cd separation via column chromatography using MP1 anion exchanger and Eichrom TRU resin and a pre-filter for clean-up using procedures similar to those of Maréchal et al. (1999) and Wombacher et al. (2003) (Table A.1).

The elemental distribution on the condensation plates was determined using an XRF scanner (section 2.3.). Condensate samples for Cd isotope analyses were obtained by leaching the plate surfaces with either 2.8 M HNO_3 or 2.5 M HCl using a pipette to apply and remove an acid droplet for several tens of seconds. Some acid droplets spread out such that the corresponding locality of the condensate sample is not precisely constrained and the removal with the pipette is not 100% efficient. Sampling has been carried out about every 10 mm along the plates. Separation of Cd from these leachates was done by column chromatography as described above.

2.3. Elemental and isotope analyses

For melt residue samples, Cd abundances were analyzed along with major elements and volatile trace elements using a Thermo ElementXR sector-field ICP-MS equipped with dual inlet spray chamber (Thermo SIS) at the University of Bonn, Germany. For external calibration of element concentrations, five element standard solutions containing all volatile trace elements of interest with concentrations of 0, 0.2, 2, 20 and 200 µg/ml each were measured. Sample Mg was used for internal normalization. To quantify the Cd depletion *f*, sample Cd/Mg was normalized to the first sample of each experiment (Table 2.1).

In order to examine the volatile element distribution at the top 10 cm (experiment 1) or 20 cm (experiment 2) of the condensation plates, the plate surface was scanned by an energy dispersive XRF scanner (Cox Analytical Systems ITRAX) at the Universität zu Köln. The instrument was equipped with a Mo x-ray tube operated at an acceleration voltage of 30 kV and 30 mA. Measurements were implemented with an 8 mm X-ray beam and a resolution of 500 µm. Matrix correction was performed via software.

Cadmium separated from melt residue samples (Table 2.1) and condensates (Table 2.2) was analyzed for isotope compositions using a Thermo Scientific Neptune multi-collector ICP-MS in low resolution, an APEX sample introduction system and the following cup configuration: L4 (^{107}Ag), L3 (^{108}Cd+^{108}Pd); L2 (^{109}Ag), L1 (^{110}Cd+^{110}Pd); C (^{111}Cd), H1 (^{112}Cd+^{112}Sn), H2 (^{114}Cd+^{114}Sn), H3 (^{117}Sn), H4 (^{118}Sn), with 10^{11} Ω resistors in the amplifier feedback loop, except for H3 and H4 with 10^{12} Ω resistors. Standard bracketing with an in-house JMC Cd standard was combined with the use of ^{109}Ag/^{107}Ag for mass bias drift correction using the exponential law. To this end, the same Ag solution was added to all sample and standard solutions (Wombacher et al., 2003; Abouchami et al., 2013). Results are corrected for minor Sn interferences and reported as $\Delta^{114}Cd/^{110}Cd = 1000*((^{114}Cd/^{110}Cd)_{sample}/(^{114}Cd/^{110}Cd)_{1st\ sample} -1)$, where $^{114}Cd/^{110}Cd_{1st\ sample}$ refers to the first sample taken from the melt residue in each experiment, respectively. The repeatability (2 s.d.) for $\Delta^{114}Cd/^{110}Cd$ (in ‰) was ±0.03 for a 100 ppb NIST SRM 3108 Cd standard solution that was measured as a sample (n=4), ±0.04 for sample 1-0 (Table 2.1). All other melt residue samples given in Table 2.1 were measured twice. The maximum difference between two replicates was 0.05 for $\Delta^{114}Cd/^{110}Cd$ and the average is given in Table 2.1. Some condensate samples were analyzed in two different measurement sessions (Table 2.2), with a maximum difference of 0.13 for $\Delta^{114}Cd/^{110}Cd$.

Table 2.1. Melt residue samples.

Sample	**t (h)**	**depletion *f***	**$\Delta^{114/110}$Cd**
$CO\text{-}CO_2$ (experiment 1)			
1-0	0.1	1.00	0.00
1-5	0.92	0.95	-0.15
1-9	2.32	0.38	0.07
1-10	2.53	0.31	-0.13
1-12	3.5	0.14	0.18
air (experiment 2)			
2-0	0.08	1.00	0.00
2-7	2	0.98	0.01
2-11	4	0.92	0.08
2-15	6	0.95	0.06
2-18	9	0.91	0.13
2-21	12	0.80	0.35
2-22	24	0.62	0.90
2-24	48	0.54	0.88
2-26	72	0.37	1.53
2-27	79	0.26	2.04

$\Delta^{114/110}$Cd normalized to first sample 1-0 or 2-0, respectively.

Table 2.2. Leachates from condensation plates.

Sample	**dms (mm)**	**$\Delta^{114}Cd/^{110}Cd$**
$CO\text{-}CO_2$ (experiment 1)		
1	303	-0.20
1 replicate		-0.12
2	295	-0.40
2 replicate		-0.43
3	287	-0.15
3 replicate		-0.20
4	279	-0.79
4 replicate		-0.72
5	268	-1.03
5 replicate		-1.14
6	260	-1.87
6 replicate		-1.74
7	255	-2.91
8	245	-1.68
9	236	-1.04
10	225	-0.72
air (experiment 2)		
1	301	3.67
2	294	4.52
3	289	3.66
4	275	4.58
5	237	-1.22
6	234	-0.23
7	230	-1.05
8	224	-2.61
9	224	-1.73
10	222	-2.04
11	217	-1.60

dms: distance from melt surface.

Replicate analyses from a second session.

3. THEORY

Mass-dependent equilibrium and kinetic isotope fractionation occurs in chemical and physical processes (e.g. Humayun and Cassen, 2000; Eiler et al., 2014). Equilibrium isotope partitioning becomes negligible at high temperature, whereas kinetic isotope effects during evaporation/condensation processes and diffusion through ambient gases are commonly assumed to be temperature independent. However, a subtle increase of isotope fractionation with temperature has been observed in a high-temperature Mg evaporation experiment (Richter et al., 2007).

The relationships describing isotope fractionation according to the kinetic theory of gases should apply for unidirectional kinetic evaporation and condensation without back reaction (Knudsen, 1911; Langmuir, 1913; Hirth and Pound, 1960; Eiler et al., 2014). Masses *m* in the following treatment could also refer to isotopically substituted molecules (isotopologues). However, this is neglected in the following as Cd forms a monatomic vapor upon reduction according to CdO(s) = Cd(g) + 0.5 O_2(g) (Glemser and Stöcker, 1963; Behrens and Mason, 1981). In Eq. 1, α_{kin} refers to the kinetic fractionation factor between vapor and condensed phase for isotopes denoted with subscript 1 and 2 (by convention m_1 is the mass of the lighter isotope; the denominator in isotope ratios reported) and γ refers to sticking (condensation or evaporation) coefficients:

$$\alpha_{kin} = \frac{\gamma_2}{\gamma_1}\sqrt{\frac{m_1}{m_2}} \quad (1)$$

If the ratio of evaporation or condensation coefficients γ_1/γ_2 equals 1, α_{kin} becomes $\sqrt{m_1/m_2}$ which is often adopted. According to Richter (2004), only a fraction of gaseous atoms or molecules that impinge on the surface may actually condense (stick), but sticking coefficients for two isotopes of the same element are usually assumed to be the same (Richter, 2004) for condensation. In contrast and to account for the observation from evaporation experiments that α_{kin} is usually closer to one than $\sqrt{m_1/m_2}$, γ_2/γ_1 is typically slightly larger than one for

evaporation (cf. Richter et al., 2011), which may result from different bond vibration frequencies in the melt (Simon and Young, 2007).

The above square root of mass dependence for α_{kin} results from the equipartitioning of kinetic energy, where isotopes or isotopologues of lighter mass assume higher velocities on average, such that $\alpha_{kin} = v_2/v_1$, (e.g. Humayun and Cassen, 2000). Likewise, kinetic isotope fractionation during diffusion through an ambient gas results from the differential velocities of isotopes (or isotopologues). Provided that the interaction with ambient gas molecules occurs only trough instantaneous, uncorrelated binary collisions, reduced masses

$$\mu_i = \frac{m_i * M}{(m_i + M)} \quad (2)$$

apply, where m_i refers to the mass of the trace gas isotope or isotopologue and M to the average mass of the ambient atmospheric gases. A fractionation factor equal to the inverse square root of the reduced masses μ is then expected:

$$\alpha_{diff} = \sqrt{\frac{\mu_1}{\mu_{2,}}} \quad (3)$$

(e.g. Mook, 2000; Richter et al., 2011; Eiler et al., 2014). The results from our evaporation/condensation experiment under atmospheric pressure will be compared with predictions for α_{diff} (Eq. 3; Figure 2.1) as it describes the isotope fractionation associated with evaporation at 1 bar (Richter et al., 2011), i.e. the diffusive transport of Cd vapor away from the melt surface through the ambient gas, as well as the higher collision frequency of the faster light isotopes with the condensation plates. Figure 2.1 shows calculated values for α_{diff} for isotope ratios of different elements and for different average masses of ambient gases. The figure shows that comparatively larger isotope fractionation is expected for light trace gas elements with large relative isotopic mass differences and for heavy ambient gases. This is important in cosmochemistry as it shows that comparatively small isotope effects are expected for condensation from and evaporation into an H_2 dominated solar-like gas, if the gas pressure is sufficiently high.

At least during evaporation, real fractionation factors are commonly closer to 1 than the theoretical kinetic fractionation factors $\alpha_{kin} = (m_1/m_2)^{0.5}$ and $\alpha_{diff} = (\mu_1/\mu_2)^{0.5}$ (e.g. Richter et al., 2007). To account for this observation, the exponent 0.5 in Eq. 1 and 3 can be replaced by β which is then typically < 0.5 (e.g. Richter et al., 2009).

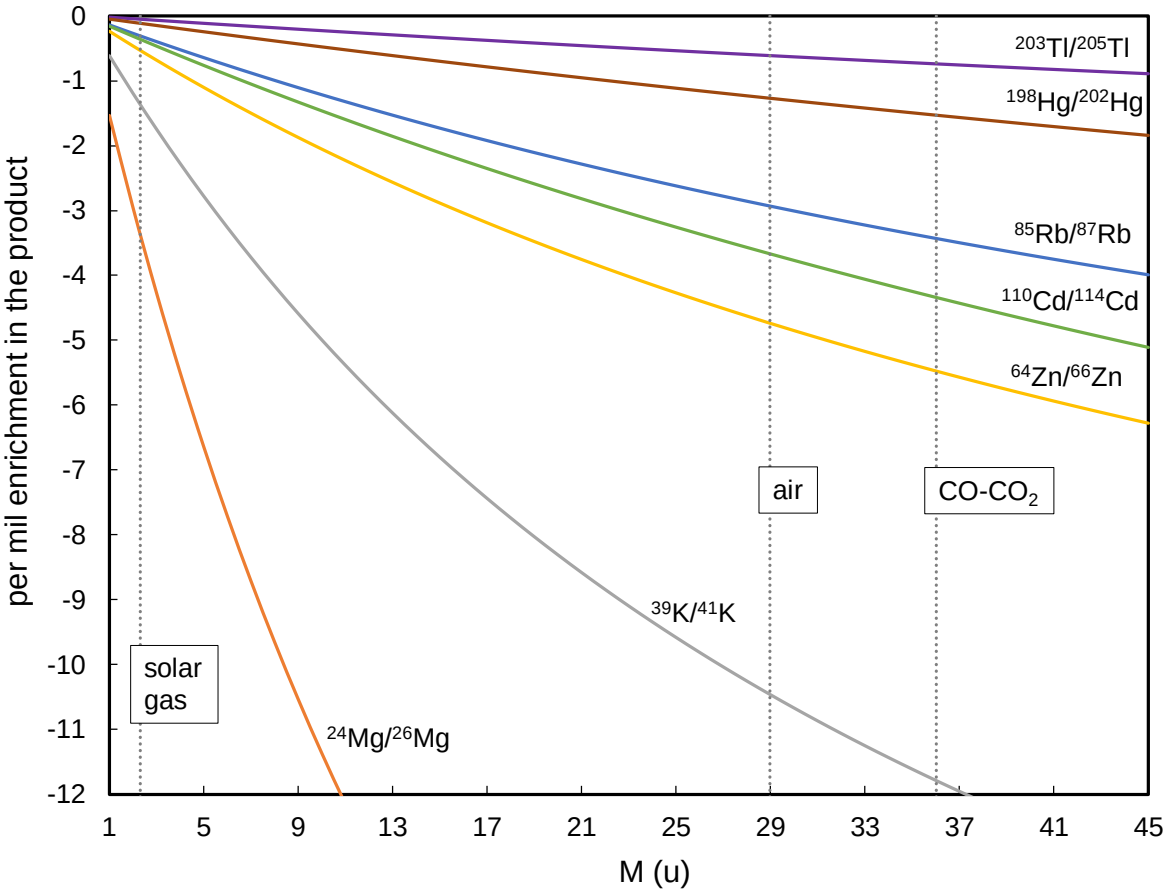

Figure 2.1. Dependence of the fractionation factor α_{diff} (Eq. 3) for the diffusion trough ambient gases on the masses of the trace gas isotopes m_i (lines for different isotope ratios) and mass M for the ambient gas. The average masses for a solar gas (M = 2.31 u; with molar fractions of 0.85 for H_2 and 0.15 for He), air (M = 28.97 u) and the CO-CO_2 mixture used in the experiment (M = 36.01 u) are indicated as stippled vertical lines. The effect of somewhat different collisional cross sections of the gas species in the mixtures has been ignored. Comparatively larger isotope fractionation is expected for light trace gases (large relative mass differences) and heavy ambient gases (M). Thus, the smallest isotope effects may be expected in H_2 dominated solar gas if the gas pressure is sufficiently high.

Evaporation and condensation are not necessarily unidirectional. In the extreme case where evaporation and condensation fluxes are equal, the equilibrium fractionation factor α_{eq} applies but is expected to be very close to 1 at high temperatures. Such a situation occurs in closed systems where the vapor has time to interact with the condensed phase, for example if most of

the vapor is released from bubbles (Wombacher et al., 2004) during boiling. Furthermore, partial back reaction (recondensation) during evaporation may result from corrugated surfaces of the condensed phase (Dauphas and Rouxel, 2006) and from collisions with gas particles overlying the evaporating condensed phase as in the current experiment.

Whether net evaporation or condensation occurs depends on the ratio of the partial pressure for species *i* in the vicinity of the condensed phase P_i to the saturation vapor pressure P_i^{sat}. In the case of free evaporation (vacuum), $P_i/P_i^{sat} \ll 1$ results in a unidirectional evaporation flux without significant recondensation. On the contrary, $P_i/P_i^{sat} \gg 1$ results in net condensation without evaporation. The system is at equilibrium with equal evaporation and condensation fluxes (with $\alpha_{eq} = \alpha_{cond}/\alpha_{evap}$) if $P_i/P_i^{sat} = 1$.

If the following assumptions are met, we can calculate the ratio of the net flux J_{net} to the forward flux J_f from measured effective α values (α_{eff}): 1) the ratio of sticking coefficients $\gamma_2/\gamma_1 = 1$, 2) the effective isotope fractionation factor α_{eff} is closer to one only because of partial back reaction, 3) that the theoretical kinetic isotope fractionation factor α_{theory} can be calculated using Eq. 1 or 3 and 4) that α_{eq} is known (here we expect $\alpha_{eq} = 1$ at high T):

$$\frac{J_{net}}{J_f} = 1 - \left(\frac{\alpha_{theory}}{\alpha_{eff}} - 1\right) \Big/ \left(\frac{\alpha_{theory}}{\alpha_{eq}} - 1\right) \quad (4)$$

For evaporation, P_i/P_i^{sat} can be calculated by

$$\frac{P_i}{P_i^{sat}} = 1 - \frac{J_{net}}{J_{evap}} \quad (5)$$

(Richter et al., 2002) and for condensation the equivalent expression is

$$\frac{P_i}{P_i^{sat}} = 1 \Big/ \left(1 - \frac{J_{net}}{J_{cond}}\right) \quad (6)$$

where J_{evap} and J_{cond} are the forward (total) evaporation and condensation fluxes, respectively.

Kinetic condensation requires that the ambient vapor is highly supersaturated in the element of interest (Davis and Richter, 2013), which may happen in case of condensation onto a cooler substrate (Esat and Taylor, 1999) or from a rapidly cooling vapor phase (Kehm et al., 2003; Richter, 2004). Since the lighter isotopes (or isotopologues) travel faster on average, the higher collision frequency of the lighter species leads to the enrichment of the lighter isotopes in the condensates. In the experience of the authors, the idea that kinetic condensation enriches the condensate in the light isotopes is often met with skepticism, which probably results from the well-known heavy O and H isotope enrichment in the condensate during atmospheric water condensation under equilibrium conditions at low temperatures. Furthermore, the importance of light isotope enrichment by partial kinetic condensation has been questioned, mainly for two reasons (Moynier et al., 2006; Kato and Moynier, 2017): First, there is no clear experimental evidence for light isotope enrichment upon partial kinetic condensation and second, it was postulated that light isotopes would stick less efficiently due to their shorter residence time on solid surfaces (Moynier et al., 2006), which would result from the lower bond energy between light isotopes and surface compared to heavier isotopes. Furthermore, the higher vibrational frequency of light isotopes would promote more attempts to escape from the surface. However, as for equilibrium isotope partitioning, the energy difference upon isotopic substitution and the difference between vibrational energy levels assumes very small values at high temperatures, hence the above arguments for lower residence times of lighter isotopes are of minor importance for condensation at high temperatures which applies for most metal isotope systems. Exceptional low-temperature metal condensation may occur for Hg and perhaps, under high vacuum conditions, also for highly volatile elements like Cd. If high degrees of undercooling and supersaturation make kinetic condensation unidirectional, light isotope enrichment in the condensate similar to α_{kin} (Eq.1) or α_{diff} (Eq. 3) is to be expected.

While kinetic evaporation experiments resulted in vapor phases enriched in the light isotopes and the evaporation residues enriched in the heavy isotopes (e.g. Esat et al., 1986; Molini-Vlesko et al., 1986; Davis et al., 1990; Wombacher et al., 2004), Moynier et al. (2006) and Kato and Moynier (2017) pointed out, that no previous condensation experiments clearly supports light isotope enrichment in the condensate relative to the vapor phase. Experiments for metal stable isotope fractionation during condensation were performed by Esat (1988) and Uyeda et al. (1991). Esat (1988) analyzed Mg isotopes from condensates after distillation of pyroxene crystals in vacuum at about 2150°C. They observed light isotope enrichment in the condensate. However, these results are ambiguous as they may also reflect light isotope enrichment of the vapor due to kinetic isotope fractionation during evaporation (Richter, 2004). The results of

another condensation experiments by Uyeda et al. (1991) are not in agreement with kinetic theory. In their experiments, silicate gas from the evaporation of forsterite condensed onto a cold finger with a temperature gradient (decreasing temperature with distance from vapor source). Condensates along the cold finger were analyzed and showed heavy Mg isotope enrichments in the first condensates at the highest temperature, while kinetic theory predicts the enrichment of light Mg isotopes in the first condensates. Richter (2004) states that the results from Uyeda et al. (1991) cannot be explained by the standard representation of condensation (as outlined above).

4. RESULTS

4.1. Cadmium loss and isotope fractionation in silicate melt residues

For experiment 1 (CO-CO_2) and experiment 2 (air), Figure 2.2 gives the depletion of Cd in the melt as the Cd fraction *f* remaining in the residue vs. time. Initially, the Cd loss under reduced conditions is about 19 times faster (7.6 vs. 0.41 µmol Cd min^{-1}) mainly because the lower oxygen fugacity shifts the equilibrium to the right-hand side of the equation $CdO(s) \leftrightarrow Cd(g) + 0.5\ O_2(g)$.

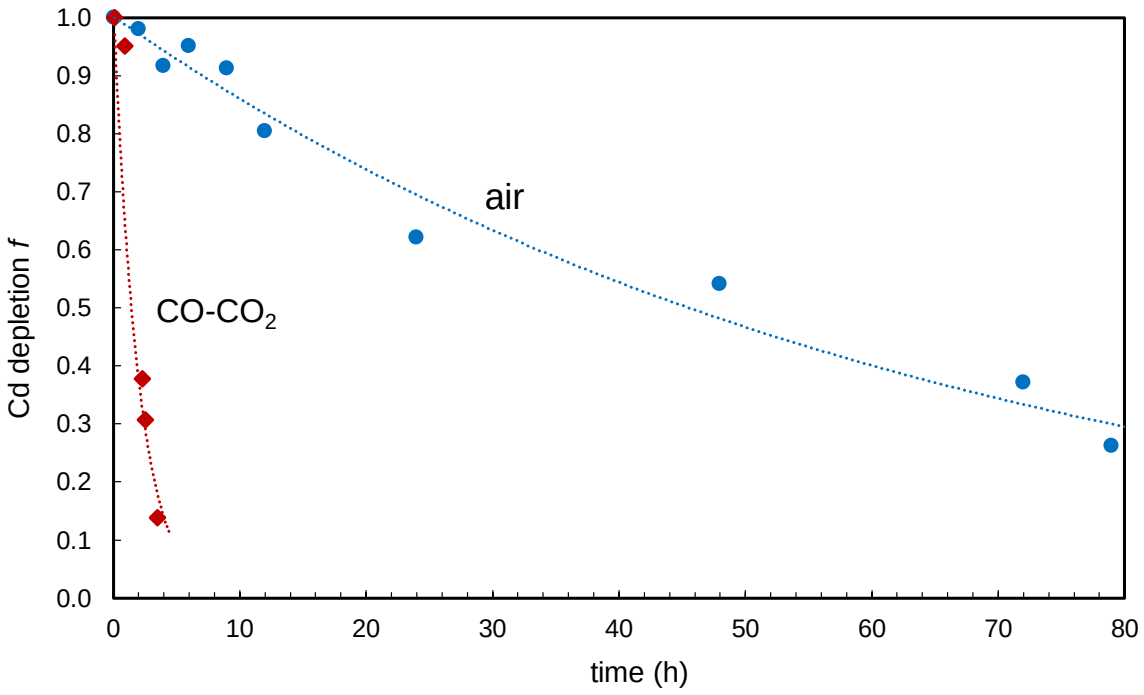

Figure 2.2. Cadmium depletion in the melt given as the fraction remaining in the residue *f* vs. time for experiments 1 (CO-CO_2) and experiment 2 (air).

For open system evaporation, assuming that homogeneity of the residue is maintained by stirring of the melt, and for condensation from a given volume of gas, the isotopic composition of the residue (or residual gas) is expected to follow a Rayleigh fractionation trend described by

$$\left(\frac{N_1}{N_2}\right)_{residue} = \left(\frac{N_1}{N_2}\right)_{initial} f^{(\alpha-1)} \qquad (7)$$

where *f* is the fraction of the element remaining in the residue (or residual gas) and N_1/N_2 is the isotope ratio under consideration. The observed pattern for Cd isotope fractionation in the residual melt during evaporation into air indeed follows a Rayleigh fractionation curve (Figure 2.3), while no resolvable isotope fractionation is observed for evaporation into the CO-CO_2 mixture.

The fractionation factors α_{eff} given in Figure 2.3 and Table 2.3 were calculated as the slope 1000*(α-1) derived from the linear regression of $1000*\ln((^{114}Cd/^{110}Cd)_{residue}/(^{114}Cd/^{110}Cd)_{starting\ material})$ versus ln(*f*) at the 95% confidence level (Eq. 7; cf. Richter et al., 2011). Evaporation into air (experiment 2) resulted in $1000*(1-\alpha_{air}) = -1.54 \pm 0.08$ ($\alpha_{air} = 0.99846\pm8$), while evaporation into CO-CO_2 gave $1000*(1-\alpha_{CO\text{-}CO2}) = -0.04 \pm 0.14$ ($\alpha_{CO\text{-}CO2} = 0.99996\pm14$) (Figure 2.3).

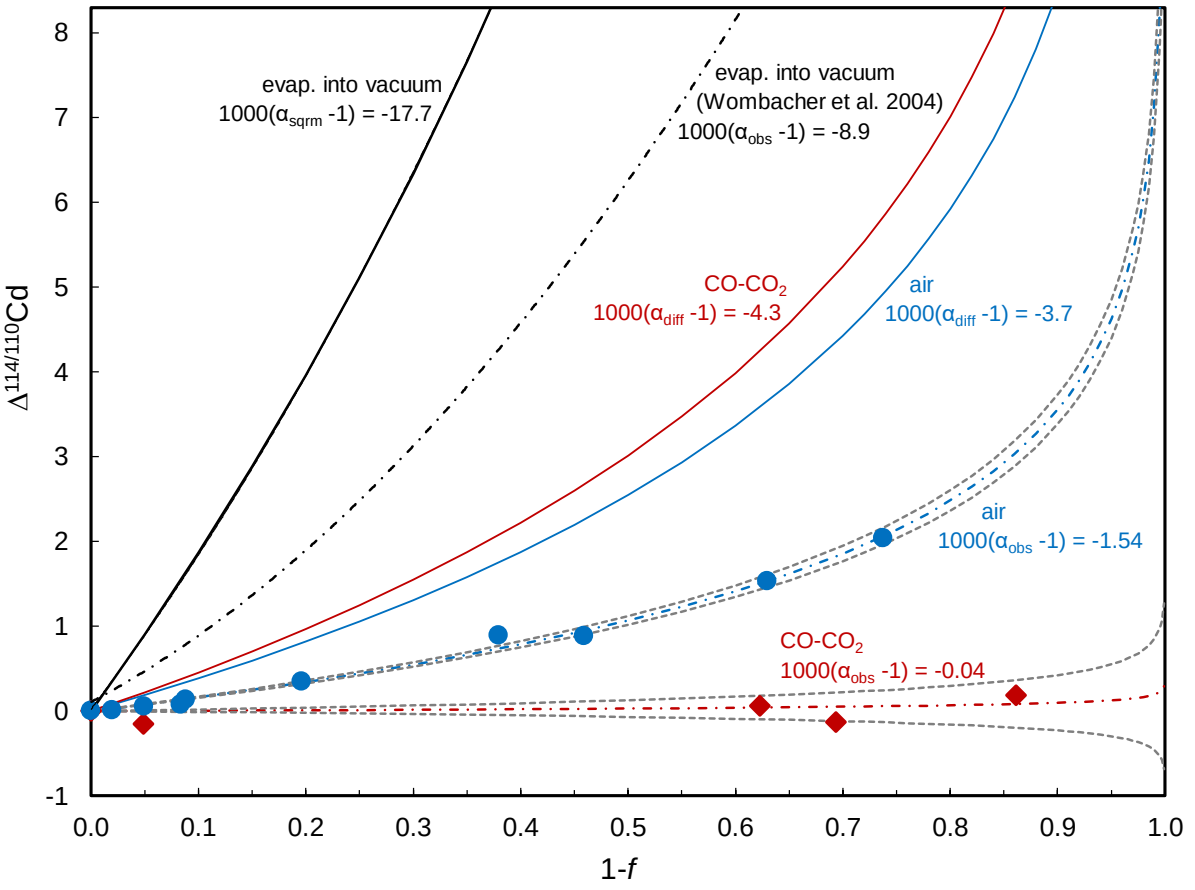

Figure 2.3. Rayleigh fractionation due to evaporation, where f is the mass fraction of Cd left in residues. Red dashed curve fitted to red diamonds for experiment 1 (CO-CO_2). Blue dashed curve fitted to blue circles for experiment 2 (air). For comparison, solid red and blue curves are given for isotope fractionation due to diffusive transport away from the melt trough CO-CO_2 and air, respectively (Eq. 3); the black solid curve is for evaporation into vacuum as calculated using α according to Eq. 1 with $\gamma_1/\gamma_2 = 1$ and the stippled black curve refers to the Cd isotope fractionation observed for evaporation into vacuum (Wombacher et al., 2004).

The observed isotope fractionation during evaporation into both atmospheres is much less than predicted by $\alpha_{diff} = (\mu_1/\mu_2)^{0.5}$, which yields $\alpha = 0.9963$ ($1000*(1-\alpha) = -3.7$) or 0.9957 ($1000*(1-\alpha) = -4.3$) for air and CO-CO_2, respectively. The corresponding $ß_{eff}$-values (Table 2.3) are 0.21 in air and ß near zero for CO-CO_2.

Table 2.3. Measured and calculated parameter for evaporation and condensation of Cd in air and CO-CO_2

Process	α_{diff}	α_{eq}	α_{eff}	$1000*(\alpha-1)$	β_{eff}	$P_i/P_{i,sat}$	$J_{net}/J_{eva(cond)}$
evap. CO-CO_2	0.99566	1.00000	0.99996±14	-0.04±0.14	0.00	0.99	0.01
evap. air	0.99633	1.00000	0.99846±8	-1.54±0.08	0.21	0.58	0.42
cond. CO-CO_2	0.99566	1.00000	0.99750	-2.50	0.29	2.35	0.57
cond. air	0.99633	1.00000	0.99633	-3.67	0.50	n.d.	1.00

n.d.: not defined for $J_{net}/J_{cond} = 1$ (moves towards infinity if condensation becomes unidirectional)

$\beta_{eff} = Ln(\alpha_{eff})/Ln(\mu_2/\mu_1)$

4.2. Condensation plates and Rayleigh condensation model

Most of the Cd vapor recondensed inside the furnace tube where two Al_2O_3 plates were inserted (Figure 2.4). In air, Cd condensation occurred sharply at about 1000 K, except for a first minor peak at about 1100 K. This observation agrees reasonably well with the Cd boiling point of 1040 K under standard conditions. In the reduced CO-CO_2 atmosphere, Cd recondensation set in at a lower temperature at around 760 K, consistent with a lower boiling point at reduced conditions.

Relative to the starting material, the Cd isotope compositions of leachates from the condensation plates generally display the most negative values in the lowermost condensates at the highest temperature and a trend from negative (light) to positive (heavy) Cd isotope compositions with increasing distance from the melt surface and decreasing temperature. In CO-CO_2, the results for the three samples at the highest temperature also reveal light isotope compositions, but with an initial trend towards lighter isotope compositions towards the top. These three data are from an area where little Cd condensed, and the Cd isotope composition may therefore be affected by contamination. In any case, these three samples represent only a minuscule fraction of the condensed Cd and are therefore considered insignificant in the gross picture.

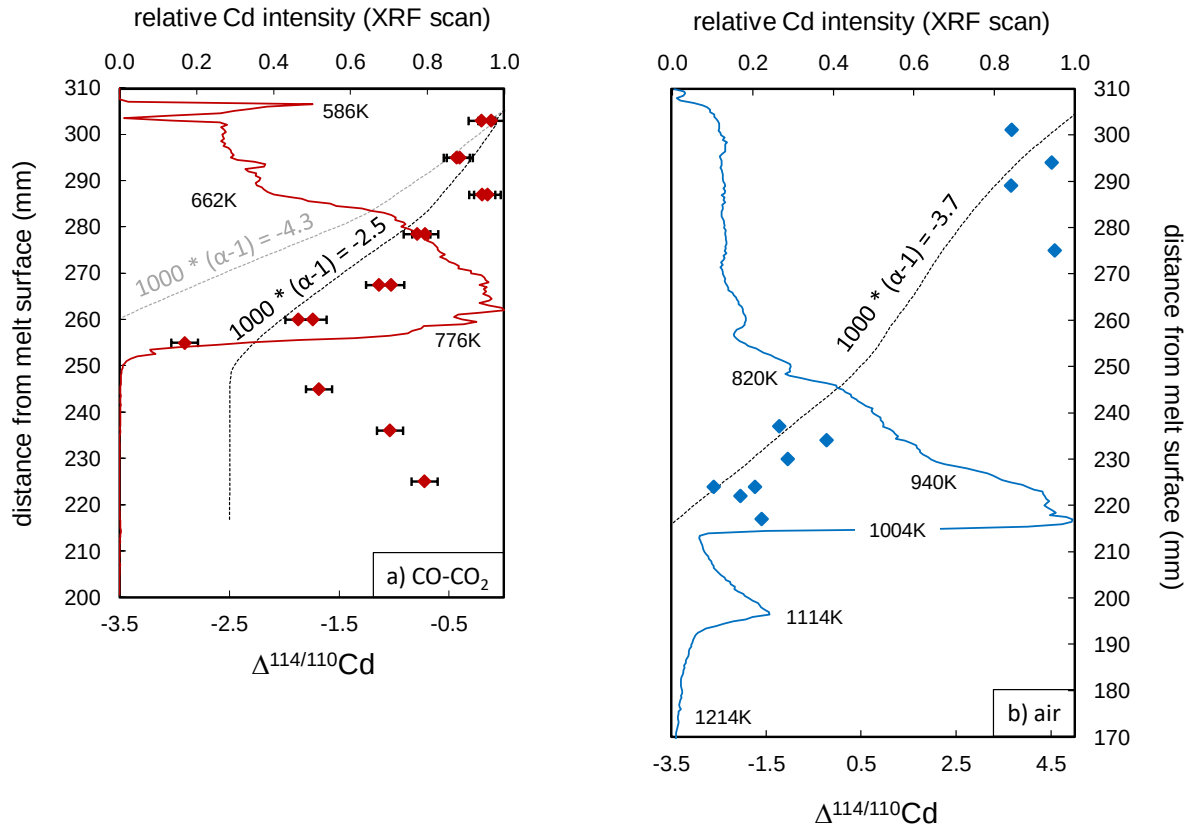

Figure 2.4. Cadmium distribution and Cd isotope compositions on condensation plates: (a) Condensation plate from experiment 1 (CO-CO_2); (b) Condensation plate from experiment 2 (air). Solid lines: Cd distribution determined by XRF scan. As the XRF scans provide only relative Cd abundances, the highest Cd signal was arbitrarily set to one. Diamonds: $\Delta^{114/110}$Cd ratio from acid leachates from the condensation plates. Modeled Rayleigh curves based on XRF data and assuming 36 % vapor loss (black dashed lines in a) and 8 % vapor loss (black dashed line in b). Furnace temperatures were measured during test runs using a type B thermocouple.

Knowledge of the Cd distribution along the condensation profiles allowed us to calculate the Cd fraction *f* remaining in the vapor phase at a given distance from the melt surface and hence to calculate Rayleigh condensation curves using Eq. 7. To this end, we assumed that the integrated bulk Cd vapor released from the melt represents the unfractionated Cd isotope composition of the starting material. This is justified as all Cd was volatilized at the end of both experiments after 72 and 336 hours, respectively (experiments 1 and 2; cf. Figure 2.2). Also, it should be noted that no resolvable stable isotope fractionation was recorded for 82 % of Cd loss into CO-CO_2 (Figure 2.3). Therefore, the stable isotope fractionation along the condensation plate in this experiment can only record the isotope effects of condensation. Our Rayleigh model also requires that the condensation profile and Cd isotope fractionation factor did not change significantly during the experimental runs. Furthermore, the Rayleigh trends in Figure 2.4 were fitted to the data, such that only 64 % of the total Cd condensed inside the

furnace tube during experiment 1 (CO-CO_2) and 92 % during experiment 2 (air) suggesting that about 36 % (8 % in air) of heavy isotope enriched Cd vapor escaped the furnace tube. This is roughly in line with the observation that the total number of XRF counts was about 30 % higher in experiment 2 and suggests that no large Cd fraction alloyed into the Pt beaker during the reduced experiment.

When applying the theoretical fractionation factors α_{diff} (Eq. 3) for diffusion in air and CO-CO_2 respectively, for air, the Rayleigh curve fitted the data reasonably well (Figure 2.4b). In CO-CO_2, a fractionation factor of 0.9956 fitted better than the theoretical value of 0.9975. Therefore, both curves are given in Figure 2.4a. Compared to what is expected for diffusion through these atmospheres, the exponent ß was estimated to be about 0.5 (air) and ~0.29 (CO-CO_2) (Table 2.3).

5. DISCUSSION

5.1. Isotope fractionation during evaporation

The description of the Cd isotope fractionation during evaporation in this study builds on the model of Craig and Gordon (1965) for the O and H stable isotope fractionation during the evaporation of water into the atmosphere. In their model, evaporation proceeds via a water-saturated and isotopically equilibrated viscous boundary layer at the interface between a liquid water body and the atmosphere. Transport of water from this saturated layer into the overlying undersaturated atmosphere then proceeds via molecular diffusion associated with additional kinetic isotope fractionation.

The fact that no measurable Cd isotope fractionation is observed during the evaporation into CO-CO_2 (β_{eff} = 0.00; see Table 2.3 for definition) is best explained by evaporative loss via a saturated boundary layer with α_{eq} being effectively equal to 1 due to the high temperature of the experiment. If an effective diffusive sublayer would have developed on top of the equilibrated viscous boundary layer, the melt composition would be expected to shift to higher $\Delta^{114/110}$Cd isotope values with depletion. This was not observed in the experiments. Therefore, advective transport assumingly dominates the removal of Cd away from the melt surface. This advective transport may be aided by the turbulences induced by the gas stream passing the crucible from below and the absence of large Cd concentration gradients on top of the saturated boundary layer.

In contrast to evaporation into CO-CO_2, evaporation into air displays appreciable Cd stable isotope fractionation with β_{eff} = 0.21. Because the gas flow rate was uncontrolled in experiment 2 (air), the stable isotope fractionation could be due to a different transport regime in air, where diffusion above a saturated boundary layer could be significant. However, Ga showed significant stable isotope fractionation with β_{eff} = 0.14 with a lower evaporation rate than Cd (Figure A.1, Figure A.2 et seq. for details) in experiment 1 (CO-CO_2), where no measurable Cd isotope fractionation occurred. This suggests that the occurrence of stable isotope fractionation is not controlled by the gas flow rate alone. More likely, the transport away from the melt is advective in both experiments and measurable Cd stable isotope fractionation in experiment 2 (air) and Ga in experiment 1 (CO-CO_2) reflects the absence of an equilibrated boundary layer on top of the melt. In other words, the rate-limiting step for the fast

Cd loss into CO-CO_2 mixture is the advective transport away from the equilibrated boundary layer, while the much lower Cd evaporation rate in to air is limited by the reduction step which was too slow to develop an equilibrated boundary layer with negligible high-temperature equilibrium Cd isotope fractionation.

Given the reasonable assumptions made in the theory section, for evaporation into CO-CO_2 mixture with a saturated boundary layer above the melt surface, the calculated net evaporation flux is very small compared to the total evaporation flux (J_{net}/J_{eva} = 0.01) due to abundant recondensation and $P_{Cd}/P_{Cd,sat}$ is close to 1. (Table 2.3). In contrast, no equilibrated boundary layer developed during evaporation into air for which we calculated J_{net}/J_{eva} ~0.4 and $P_{Cd}/P_{Cd,sat}$ ~0.6, which still indicates substantial back reaction.

5.2. Cadmium isotope fractionation due to diffusion and condensation

Along its path up the tube furnace, the gas passes the condensation plates (for experiment 1 at a velocity of about 15 cm min^{-1}) whereby the gas molecules constantly thermalize by collisions with the furnace tube, condensation plates, the spindle and themselves. Cadmium condensation commences once the condensation plate surface temperature is low enough for impinging Cd atoms to stick. In air, this occurs at about 1040 K, the Cd boiling point at standard conditions. Due to their higher average velocity and hence collision frequency, the lighter Cd isotopes are slightly preferred during condensation. As the Cd vapor moves upwards, it becomes increasingly heavy as it preferentially loses light Cd isotopes to the condensation plates (as modeled by the Rayleigh curves in Figure 2.4).

The observation that β_{eff} equals ~0.5 (Table 2.3) suggest that condensation in air was purely kinetic, i.e. unidirectional and with sticking coefficients $\gamma = 1$, while some back reaction seems likely for condensation in CO-CO_2 (Table 2.3). However, given the current data, it is difficult to judge how well the leachates represent the true Cd isotope composition and location of Cd on the condensation plates and observations such as the Cd abundance peak at about 1100 K for condensation of Cd in air are not understood. Therefore, the exact values given in in Table 2.3 for condensation should be viewed with caution. However, the isotope fractionation along the condensation plates can be unambiguously tied to condensation whereby light isotopes condense preferentially as expected from their higher collision frequency predicted by kinetic theory.

6. CONCLUSION

The mechanically assisted equilibration technique (Dingwell et al., 1994; Ertel-Ingrisch and Dingwell, 2010a; Ertel-Ingrisch and Dingwell, 2010b) has proven suitable for the experimental study of Cd isotope fractionation related to evaporation and condensation at atmospheric pressure.

Presented results from combined Cd evaporation and condensation experiments at 1 bar are in agreement with kinetic theory, which suggests that isotope fractionation due to diffusion through an ambient atmosphere can be described by a fractionation factor $\alpha = (\mu_2/\mu_1)^{0.5}$ (see theory in section 3) and that light isotopes become enriched in partial condensates.

While the condensation experiment was conducted at atmospheric pressure where the fractionation factors need to be calculated from reduced masses, kinetic condensation in vacuum should be characterized by larger isotope fractionations, provided that back reaction is limited. Isotopically zoned metal grains in CH and CB chondrites may be the best natural examples for kinetic condensation (Alexander and Hewins, 2004; Zipfel and Weyer, 2007; Richter et al., 2014; Weyrauch et al., 2017). Partial kinetic condensation may also explain the light Sn and Zn isotope enrichment with increasing volatile element depletion in carbonaceous chondrites (Bourdon et al., 2017) and the related light volatile element isotope enrichments observed in chondrules and CAIs (Luck et al., 2005; Wombacher et al., 2008; Pringle et al., 2017; Kato and Moynier, 2017)

It has been argued that volatile loss in the early solar system cannot be due to partial evaporation of volatile elements, as partial evaporation would always be accompanied by stable isotope fractionation (Humayun and Clayton, 1995). Results from melt residue sample analyses give experimental evidence that evaporation can proceed without resolvable isotope fractionation at least under very special circumstances, characterized by high temperatures (1580 K), an equilibrated boundary layer at the interface between the condensed and the gas phase combined with advective transport of equilibrated vapor away from the melt. Volatile element loss from a melt into an ambient atmosphere is generally expected to be characterized by smaller isotope fractionation than free volatile loss from atmosphere absent bodies such as the Moon or achondrite parent bodies. This is because fractionation factors for evaporation into an

atmosphere of sufficient pressure need to be calculated using reduced masses (Richter et al., 2011; Figure 2.1) and because of increased back reaction due to the overlying gas pressure.

III. Homogeneous iron isotope composition of chondrites and Earth

1. INTRODUCTION

1.1. The formation of the elements and isotopes

The chemical elements formed – and still form – in various environments. Hydrogen, He and traces of Li formed shortly after the big bang. Elements with a mass up to Fe, are mainly formed by nuclear fusion inside stars and during supernova explosions. Elements heavier than iron are mainly formed by neutron (n-) capture. The occurrence of nuclear fusion for masses up to iron and n-capture as the main process for the formation of heavier elements is best illustrated in the plot of binding energy vs. atomic mass (Figure 3.1, Hezel (2019)): ^{56}Fe and other nuclides of similar mass have the highest binding energies per nucleon. The binding energy is equivalent to the mass defect, according to Einstein's equation $E = mc^2$, and is highest for ^{56}Fe. Energy is released when tightly bond nuclides form via fusion on the expense of lower mass nuclides. While most fusion reactions up to about ^{56}Fe are endothermic, the fusion of nuclides heavier than Fe would consume energy.

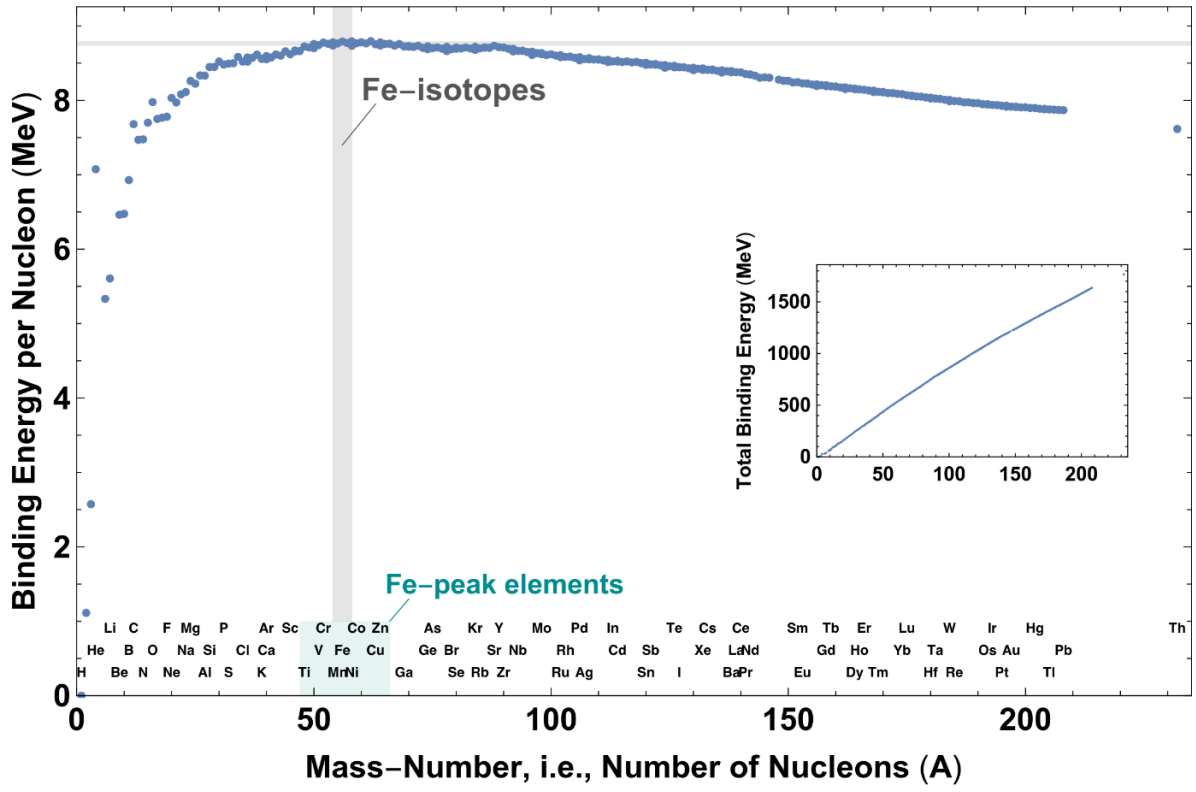

Figure 3.1. Binding energy (mass defect) per nucleon vs. atomic mass by Hezel (2019).

In Figure 3.2 (Heger et al., 2013), iron shows a peak in the abundances of isotopes present in the solar system. The neighboring elements of Fe – Cr, Mn, Co, Ni and Ti – together with Fe are often referred to as *Fe-peak elements*.

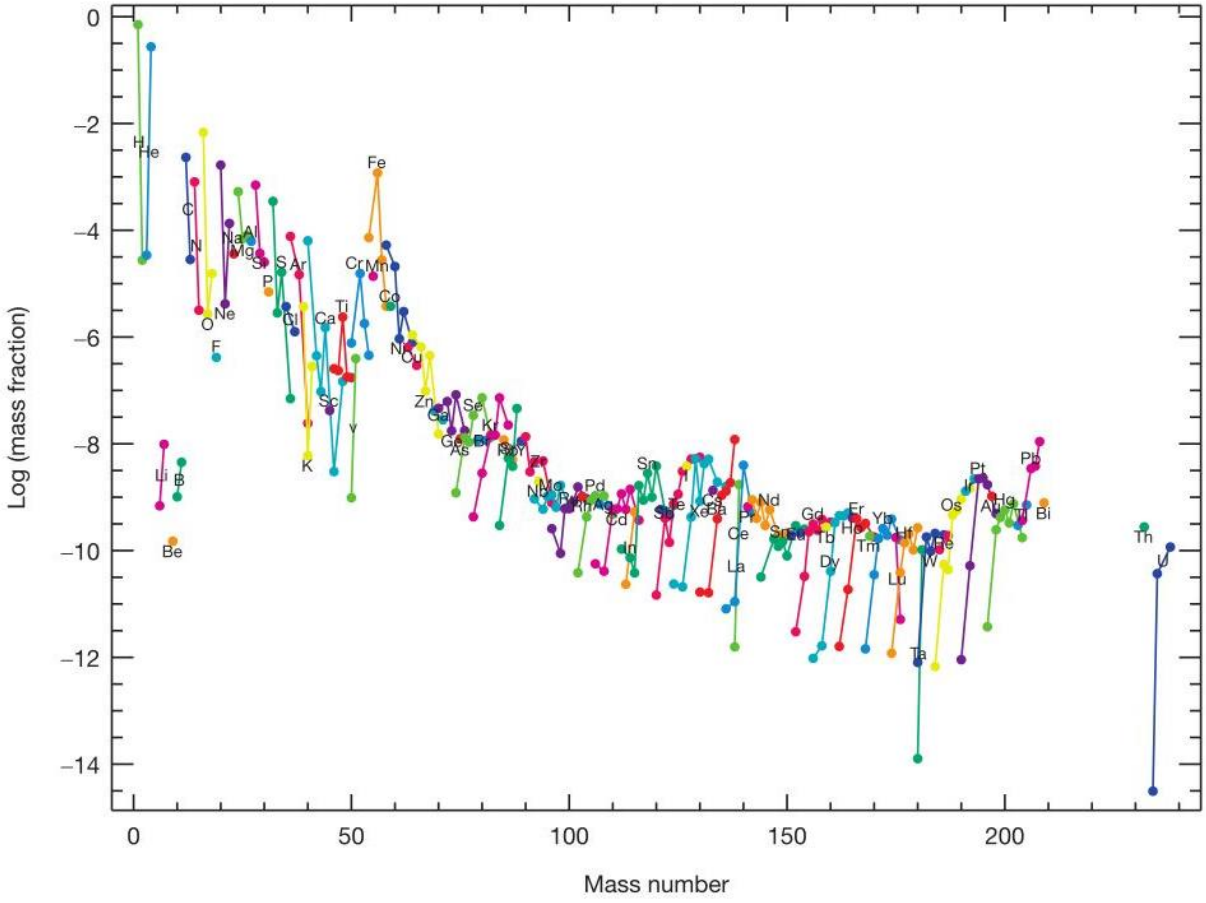

Figure 3.2. Isotope abundances present in the solar system matter by Heger et al., (2013), showing the "Fe-peak".

The relative isotope abundance of each element depends on their nuclear properties and their formation environment. The four stable isotopes of Fe (^{54}Fe, ^{56}Fe, ^{57}Fe, ^{58}Fe), for example, have different relative abundances if formed in e.g., a core-collapse supernova, compared to when these formed in a thermonuclear supernova. To understand the heritage of the nucleosynthetic anomalies of Fe-peak elements in meteorites, the origin of the relative nuclide abundances as produced in the various nuclide formation environments must be evaluated. The following sections summarize the current state of knowledge about the most important nucleosynthetic formation environments – type II and type Ia supernovae, as well as AGB stars –, and the relative isotope abundances produced in these.

1.1.1. Nucleosynthesis in massive stars and core-collapse supernova (Type II supernova)

Massive stars are defined as being >10 times heavier than the sun ($M_\odot$ = 1.989 × 10^{30} kg). A star is in hydrostatic equilibrium when its gravitational compression balances the radiation pressure exerted by the thermal energy from the fusion reactions in its core. Whenever the fusion regime changes the radiation pressure, the star moves towards hydrostatic equilibrium, i.e. expands or contracts. Once, the energy from the fusion reactions is largely exhausted in the Fe-rich core and core size reaches the Chandrasekhar limit of 1.4 solar masses, gravitational collapse of the core produces a supernova.

Massive stars evolve through a series of initial fusion stages from H-, He-, C- and Ne-burning, thereby producing successively heavier elements. Titanium and Cr production follows thereafter during O-burning, which ignites at about 2 billion K. The most abundant Ti nuclides produced at this stage are ^{46}Ti and ^{47}Ti. After most O is consumed by nuclear fusion, the local abundances of ^{46}Ti and ^{47}Ti are by factors of 1000 and 100, respectively, higher relative to the concentration at the beginning of O-burning (Clayton, 2003). The final burning stage, Si-burning, ignites at about 3 billion K, where ^{46}Ti is quickly consumed and hence does not contribute to the ISM, while ^{47}Ti survives Si-burning. Abundant ^{56}Ni with a short half-life of only 6.075 d is produced, which decays to ^{56}Co (half-life of 77.31 d) and finally to the stable nuclide ^{56}Fe. The main product of Si-burning is thus ^{56}Fe, the nuclide with the highest binding energy per nucleon. Nuclei of ^{54}Fe are produced with a 6.3% higher $^{54/56}$Fe ratio than solar.

Silicon-burning is not simply characterized by fusion reactions whereby increasingly heavy nuclides are produced as in previous burning stages. The high temperatures during Si-burning partially photodisintegrate nuclides from previous fusion reactions, in particular the most abundant nuclide ^{28}Si. At the same time, freed α-, p- and n-particles result in fast capture reactions, which drives the system towards nuclear statistical equilibrium (NSE) between photodisintegration and nuclide production. Only small amounts of the Fe-peak element nuclei photodisintegrate, because of their high binding energy, as displayed in Figure 3.1. Thus, the relative Fe-peak element abundances increase (Lugaro, 2005).

Helium- or C-burning produced nuclei with a neutron to proton overabundance, mainly ^{22}Ne with 10 protons and 12 neutrons. The reaction ^{22}Ne(α,n)^{25}Mg where ^{22}Ne captures an α-particle and emits a n-particle, to form ^{25}Mg, provides free neutrons (Pignatari et al., 2010). In this case, the synthesis of ^{60,61,62}Ni, ^{50}Ti and ^{54}Cr and many heavy nuclides occurs via slow neutron capture (s-process). Further, during Si-burning, ^{54}Fe and ^{56}Fe can then be directly produced via

neutron capture and the synthesized Fe-peak element isotope composition shifts towards neutron-rich nuclei (Lugaro, 2005).

After the material in the core was largely converted to Ni and Fe, insufficient radiation energy is generated to counteract the gravitational core contraction. The core is destabilized and starts to collapse until its density increases close to nuclear densities. Iron and Ni isotopes disintegrate into neutrons and previously synthesized abundances are no longer present. The infalling matter then bounces back from this high-density core, setting off a shock wave that travels outward through all the layers in the star (Thielemann, 1984). This shock wave produces an extremely hot environment (6-10 billion K) in which nuclei are disintegrated into neutrons and α-particles. Nuclear fusion is again ignited in the ejected layers of the supernova and large amounts of ^{56}Ni, as well as substantial portions of ^{57}Ni and ^{58}Ni are produced via explosive Si-burning. This Si-burning also produces ^{46}Ti, from which ^{47}Ti can form via n-capture. Nuclei of ^{48}Ti and ^{49}Ti are products of radioactive Cr decay. The decay of ^{52}Fe and ^{53}Fe produce ^{52}Cr and ^{53}Cr close to the core, whereas ^{50}Cr is produced further away from the core. The isotopes ^{60,61,62}Ni are produced from radioactive Cu and Zn, and also during explosive Si-burning (Clayton, 2003). Although the s-process produces a large range of Fe-group element nuclei, the relative abundances are highly different. Abundant isotopes are ^{54}Fe and ^{56}Fe. The outside layers of the supernova and its nuclei are ejected into the interstellar medium (ISM), e.g., a supernova of a star with ~25 $M_\odot$ ejects a net quantity of about 10^{29} kg ^{56}Ni which decays via ^{56}Co to ^{56}Fe. Fe-peak elements synthesized close to the core are not ejected but fall back to the core.

The outer layers cool during expansion while α-particle capture as well as photodisintegration approximates NSE or quasi-equilibrium in the system. After further cooling of the expanding supernova layers, the temperature drops to a level where the system moves away from quasi-equilibrium and nuclear reaction rates decrease. Charged particles ‘freeze out’, but the temperature is still sufficiently high for α-particle capture, creating α-rich isotopes, such as the radioactive ^{44}Ti (Lugaro, 2005). The production of ^{54}Fe drops and the ratio of $^{54/56}$Fe falls below the solar ratio, compensating the higher ratio of $^{54/56}$Fe, produced during NSE. At this stage, ^{61}Ni and ^{62}Ni are produced slightly more effectively than during Si-burning (Clayton, 2003).

1.1.2. Nucleosynthesis in binary systems with white dwarfs (Type Ia supernova)

Type Ia supernova explosions produce Fe-peak elements more efficiently than type II supernovae but are much less abundant than the latter (Clayton, 2003). As described by e.g. Iwamoto et al. (1999) and Lugaro (2005), a binary system as precursor of type Ia supernovae consists of two stars that are locked in a close orbit for their entire stellar evolution. The star with greater mass (but <~10 $M_\odot$) develops into a white dwarf at the end its life cycle and successively accretes matter from the companion star, that has evolved into a red giant. If the white dwarf has accreted substantial amounts of H and He from his companion star, H- and subsequent He-burning ignites in its outer shell. In its final stage, the core of the white dwarf typically contains mainly C and O. Further accretion increases its mass until the Chandrasekhar-limit of 1.4 $M_\odot$ is approached. Upon further contraction, explosive C-burning ignites. In the final stage, an explosive wave disrupts the star into a thermonuclear type Ia supernova, without leaving behind a remnant. In the expanding layers, nuclear reactions ignite and the system changes into thermonuclear equilibrium, in which primarily ^{54}Fe, ^{56}Fe, ^{57}Fe and ^{60}Ni are produced. A large abundance of ^{56}Fe is directly created via n-capture (Nomoto et al., 1997). The amount and relative abundance of produced Fe isotopes depends on the initial mass, rotation, speed and composition of the white dwarf, as well as the mass accretion rate and species of accreted matter (Nomoto et al., 1997). Additional nuclides that are produced in significant amounts are ^{46,48,49}Ti and ^{53}Cr. Abundant production of the neutron-rich nuclides ^{54}Cr, ^{50}Ti and ^{60,61,62,64}Ni via s-process occurs only in white dwarfs with a mass close to 1.4 $M_\odot$, when a high-neutron flux is produced (Woosley, 1997; Clayton, 2003; Lugaro, 2005).

1.1.3. Nucleosynthesis in AGB stars

Asymptotic giant branch (AGB) stars have masses between 0.6 and 10 $M_\odot$. A star of this mass enters the AGB phase after all He in its core was fused to C and O. The core of an AGB star is tiny compared to its surrounding envelopes. Close to the core, a He-burning shell is surrounded by an H-burning shell, which is then surrounded by an enormous H-rich envelope (Lattanzio, 2002). The growing thickness of the layers causes compression and consequently a rise of temperature and density. It follows a thermal runaway reaction (*thermal puls*e) that releases energy as in the shell. Convective energy transport (*convective pulse*) induces the mixing of the surrounding envelopes and the transport of the products of H- and He-burning to the surface (Zhang et al., 1998; Lattanzio, 2002; Lugaro, 2005). This material transport is called *dredge-up*.

During each dredge-up, the shell expands, cools and for a while, all fusion processes come to a halt. Temperature and neutron density increase with every dredge-up (Lugaro, 2005). After only a few hundred years the thermal pulse loses its energy, and a new cycle of H- and He-burning with subsequent dredge-up starts.

Neutrons in AGB stars are mainly produced in the He-shell via the reaction $^{13}C(\alpha,n)^{16}O$ and at higher temperatures at the bottom of the shell via the reaction $^{22}Ne(\alpha,n)^{25}Mg$. Thereby, so-called ^{13}C pockets form, in which slow neutron capture nucleosynthesis (s-process) proceeds (Lattanzio, 2002; Lattanzio and Lugaro, 2005; Straniero et al., 2006; Pagel, 2008). Neutron-rich nuclides are produced in these pockets, mainly ^{50}Ti, ^{54}Cr, ^{58}Fe, and ^{64}Ni, and, to a smaller extent, ^{49}Ti, ^{46}Ti, ^{53}Cr, ^{57}Fe and ^{61}Ni (Wasserburg et al., 2015).

The mass of the AGB core increases with every dredge-up (Zhang et al., 1998). As described by Lugaro (2005), the circumstellar envelopes that surround the AGB star are blown away by strong stellar winds with every dredge-up/thermal pulse, whereby the mass of the convective envelope continually decreases while the ejected matter enriches the ISM in fusion and s-process products. In consideration of the mass balance of the solar system, it is believed that AGB stars are the main production site of s-process nuclei contributing to the ISM (Birck, 2004).

1.2. Nucleosynthetic anomalies of Fe-peak element isotopes in solar system materials

The newly synthesized elements feed the interstellar medium (ISM) via stellar explosions, ejected stellar envelopes and stellar winds. With time, evaporation and recondensation processes triggered by the galactic background radiation produce a chemically and isotopically largely homogeneous ISM (Hoppe et al., 2017). Our solar system formed 4.56 Ga ago when a molecular cloud separated from the local ISM, collapsed under its own gravity whereby the rotational speed increased, and a protoplanetary disk formed around the sun. Our solar system inherited its isotope composition from the local ISM. Figure 3.3 displays the Fe isotope compositions of meteoritic and terrestrial materials (Zhu et al., 2001). All samples plot onto a single mass-dependent fractionation line, thereby displaying the homogeneity of iron isotopes in the solar system at the planetary body and meteorite sample scale. In contrast, Figure 3.4 (Zinner, 2013) displays Si isotope compositions of individual, tiny SiC grains found in the matrix of undifferentiated meteorites. The different grain denotations, i.e. *mainstream*, *A-B*, *X*,

Y, *Z* and *nova grains* refers to their different Si (or C, N or inferred $^{26}Al/^{27}Al$) isotope ratios (Zinner, 2013). The slope defined by mainstream grains is >1 and does not conform to a mass-dependent fractionation which would plot with a slope of ~0.5. Also, the extent of Si isotope ratio variations (e.g. Z grains) cannot be explained by mass-dependent fractionation processes.

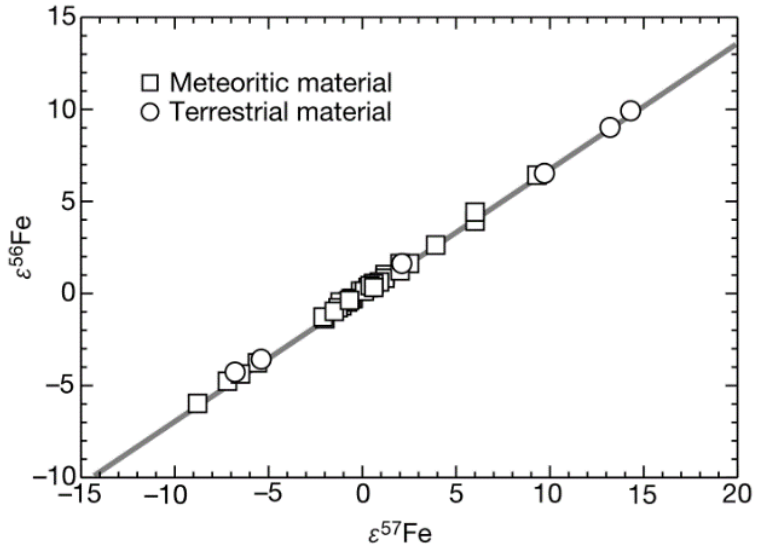

Figure 3.3. Iron three-isotope plot by Zhu et al. (2001) showing mass-dependent Fe isotope variation only.

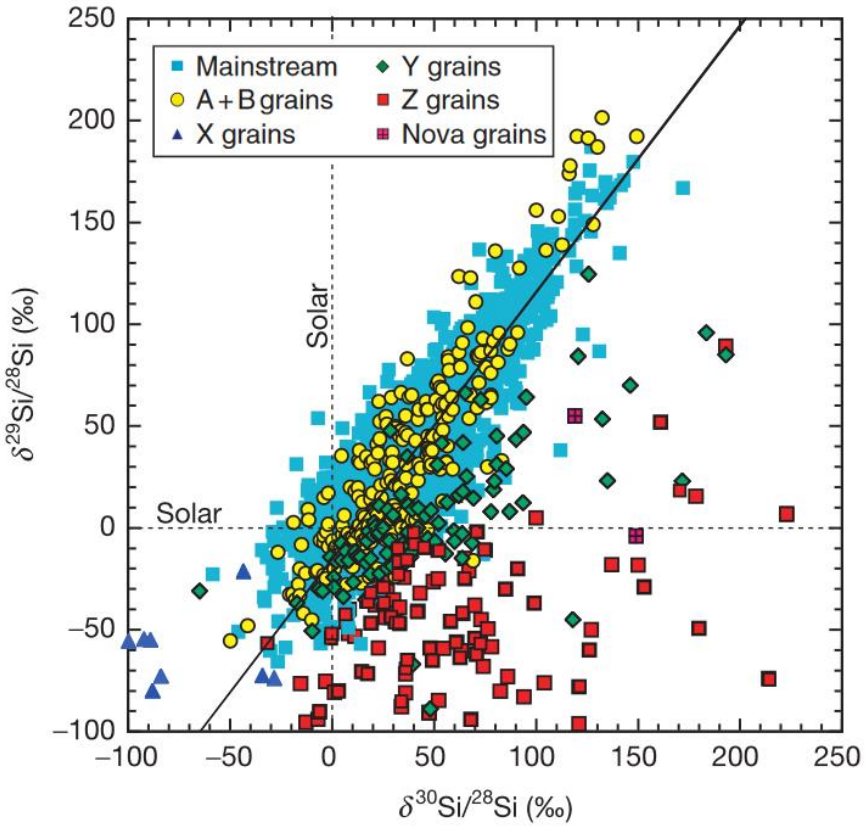

Figure 3.4. Silicon three-isotope plot by Zinner (2013) displaying huge variations due to the stellar provenance of the grains.

Therefore, the Si isotope abundances cannot be explained by mass-dependent isotope fractionation and also not by daughter excesses from prolonged radioactive decay (Lugaro, 2005). Obviously, the SiC grains escaped isotope homogenization in the ISM. Hence, these are most likely original stardust grains, i.e. grains that inherit the distinct isotope compositions from different sites of nucleosynthesis that survived the formation of the solar system in primitive chondritic meteorites and some interplanetary dust particles (IDPs). They are therefore called *presolar grains*. Their isotope inventory represents their stellar nucleosynthetic formation environment. If sufficiently abundant, the anomalous isotope composition of presolar grains relative to solar may contribute significantly to the bulk isotope composition of a meteorite or meteorite component. If different solar system materials or components therein display isotope compositions due to variable nucleosynthetic contributions, these isotope anomalies are referred to as *nucleosynthetic* anomalies. For simplicity, nucleosynthetic isotope anomalies are expressed relative to terrestrial isotope compositions. If presolar phases carry isotope anomalies, these are called *carrier* phases. A sample with a resolvable nucleosynthetic Fe isotope anomaly would plot off the mass-dependent fractionation line in Figure 3.3.

If nucleosynthetic anomalies are too small to be resolvable on bulk rock scale, one method to reveal the presence of isotope anomalies within components of the sample, is the analysis of single chondrite components, mechanically separated from the bulk sample. Another method is to sequentially leach the bulk chondrite sample in acids of increasing strength to separate the chondrite components of different acid resistivities from each other and analyze the various leachates and residues for nucleosynthetic isotope anomalies.

In order to summarize the current knowledge, the following sections review the occurrence of nucleosynthetic anomalies in four Fe-peak elements Fe, Ti, Cr and Ni in refractory inclusions, bulk meteorites, and sequential leachates of whole rock meteorite samples and, for Fe only, in presolar grains. In refractory inclusions, Fe, Ni and Cr, in contrast to Ti, are of very low abundance and may be introduced in part by secondary processes such as alteration of from matrix contamination.

Isotope ratios of numerous studies are shown in either δ-, ε- or μ-notation using the following or very similar equations:

$$\delta^{x/y}E = \left[\left(\frac{^{x/y}E_{sample}}{^{x/y}E_{standard}}\right) - 1\right] * 1000 \qquad (1)$$

$$\varepsilon^{x/y}E = \left[\left(\frac{^{x/y}E_{sample}}{^{x/y}E_{standard}}\right) - 1\right] * 10\,000 \quad (2)$$

$$\mu^{x/y}E = \left[\left(\frac{^{x/y}E_{sample}}{^{x/y}E_{standard}}\right) - 1\right] * 1\,000\,000 \quad (3)$$

Equations 1 to 3 can be applied to data with or without mass fractionation correction by internal normalization. Internal normalization removes the effects natural mass-dependent stable isotope fractionation, such that all data in Figure 3.4 would plot near the origin. To unambiguously identify data that has been internally normalized and to display the ratio used for internal normalization, we use the following notation: $\varepsilon^{56/54}Fe_{(57/54)}$ (here, $^{56/54}Fe$ was internal normalized using $^{57/54}Fe$).

1.2.1. Iron isotopes

Bulk chondrites: Iron isotope measurements of bulk chondrites were implemented for Allende (CV3) (Voelkening and Papanastassiou, 1989; Zhu et al., 2001; Dauphas et al., 2004; Hezel et al., 2010), Murchison (CM2) (Voelkening and Papanastassiou, 1989; Zhu et al., 2001), Orgueil (CI1) (Zhu et al., 2001; Dauphas et al., 2004; Hezel et al., 2010; Wang et al., 2013), Grosnaja (CV3), Mokoia (CV3) (Hezel et al., 2010), Alais (CI1), Ivuna (CI1), LEW 85320 (H5), GRO 95540 (L5), DOM 03194 (LL5) (Wang et al., 2013), Chandakapur (L5) and Indarch (EH4) (Zhu et al., 2001). Results of Hezel et al. (2010) and Wang et al. (2013) are reported as $\delta^{56/54}Fe$ and $\delta^{57/54}Fe$, while in the early work of Zhu et al. (2001) reported $\varepsilon^{57/54}Fe$ and $\varepsilon^{58/54}Fe$, all relative to the IRMM-014 standard. All bulk chondrite data of the above studies plot within error on mass-dependent fractionation lines and therefore show no nucleosynthetic isotope anomalies. Voelkening and Papanastassiou (1989) reported bulk carbonaceous chondrite Fe isotopes as $\varepsilon^{57/56}Fe_{(54/56)}$ and $\varepsilon^{58/56}Fe_{(54/56)}$, i.e. internally corrected with $^{54/56}Fe$. Results agreed within error with terrestrial values and they concluded that there are no Fe isotope anomalies in bulk chondrites. Dauphas et al. (2004) reported bulk carbonaceous chondrite Fe isotopes as $\varepsilon^{56/54}Fe_{(57/54)}$ and $\varepsilon^{58/54}Fe_{(57/54)}$, and again observed no Fe anomalies in their samples.

Sequential leachates: Leaching experiments using Semarkona (LL3), Orgueil (CI) and Murchison (CM2) were implemented by Wang et al. (2011) to search for iron isotope anomalies. They used acetic acid, HNO_3 and HCl at different temperatures, HCl-HF and additionally HNO_3-HF acid mixtures for successive leaching steps. Within an analytical

precision (2 s.e.) of 0.3 for $\varepsilon^{56/54}Fe_{(57/54)}$ and 1.5 for $\varepsilon^{58/54}Fe_{(57/54)}$ and no isotopic anomalies were resolved. They also applied a normalization scheme to $^{56/54}Fe$ and again yielded terrestrial Fe isotope compositions for all samples.

Refractory inclusions: Iron isotope analyses of calcium-aluminium-rich inclusions with fractionation and unknown nuclear effects (FUN CAIs) from the Allende CV3 chondrite by Voelkening and Papanastassiou (1989) revealed an enrichment of neutron-rich Fe isotopes. One sample revealed positive $\varepsilon^{58/56}Fe_{(54/56)}$ of up to ~300, while the other two FUN inclusions displayed an enrichment of ~30 to ~40. Measurements of four non-FUN inclusions showed $\varepsilon^{57/56}Fe_{(54/56)}$ and $\varepsilon^{58/56}Fe_{(54/56)}$ similar to terrestrial values with a slight tendency towards negative values. One exception was sample EGG-2 with $\varepsilon^{58/56}Fe_{(54/56)}$ of 27±11. Kööp et al. (2016) analyzed hibonite sample CAI 2-5-1, classified as FUN, and did not detect Fe isotope anomalies. Shollenberger et al. (2016) analyzed CAIs from Allende and other CV3 chondrites, CAIs from CK chondrites and magnetic mineral separates of Allende non-FUN CAI sample EGG-2. They reported large anomalies of $\varepsilon^{57/54}Fe_{(546/54)}$ and $\varepsilon^{58/54}Fe_{(56/54)}$ in magnetic separates of EGG-2 in opposite direction than the results of Voelkening and Papanastassiou (1989). Later, the same group (Shollenberger et al., 2017) reported their results as $\varepsilon^{56/54}Fe_{(57/54)}$ and $\varepsilon^{58/54}Fe_{(57/54)}$ and again could not confirm the $^{58/54}Fe$ anomalies, found by Voelkening and Papanastassiou (1989). Results for the magnetic separates displayed $\varepsilon^{56/54}Fe_{(57/54)}$ of varying excess of up to about 2 (Shollenberger et al., 2017).

Presolar grains: Investigations of Fe isotope anomalies in presolar grains commonly do not apply internal normalization as the measurement uncertainties but also the variations in these grains are rather large and mass-dependent effects can be neglected. Hoppe et al. (2000) analyzed eight Murchison X grains, a grain type that presumably originated in type II SN and found $\delta^{54/56}Fe$ values that do not significantly differ from zero. Tripa et al. (2002) analyzed 13 Murchison Mainstream (MS) grains that most likely condensed form low-mass C-rich AGB stars. Hoppe and Ott (1997) reported $\delta^{54/56}Fe$ ranging approximately from -170 to -50, $\delta^{57/56}Fe$ ranging approximately from -125 to +60 and $\delta^{58/56}Fe$ ranging approximately from about -300 to +400, with one sample with about +800. Marhas et al. (2008) analyzed 37 X grains and 53 SiC grains of various other classification from Murchison. They observed large $\delta^{57/56}Fe$ excesses up to +1000 in most X grains and normal $\delta^{54/56}Fe$ in almost all analyzed grains relative to the solar value. A few X grains showed a $\delta^{57/56}Fe$ deficit up to -436±23 and one Y grain, as well as one Z grain, both grain types presumed to have originated in AGB stars (Hoppe and Ott, 1997; Amari et al., 2001; Zinner et al., 2007), showed excess in $\delta^{54/56}Fe$ of +403±68 and

+288±57, respectively, with normal $\delta^{57/56}$Fe. Out of 25 SiC grains of Murchison (CM) analyzed by Kodolányi et al. (2018) only 2 showed deficits in $\delta^{54/56}$Fe of up to -29 and deficits in $\delta^{57/56}$Fe of up to -51. The highest value of $\delta^{54/56}$Fe in SiC grains of Murchison found by Trappitsch et al. (2018) is 467±96 but most grains revealed a value closer to the solar system.

Excess in $\delta^{54/56}$Fe was found by Mostefaoui and Hoppe (2004) in one pyroxene and one spinel grain from the ungrouped carbonaceous chondrite Acfer 094 with 116±44 and 63±36, respectively. One Fe-rich oxide grain from Acfer 094 analyzed by Floss et al. (2008) showed deficits in $\delta^{54/56}$Fe as well as in $\delta^{57/56}$Fe. Vollmer and Hoppe (2010) analyzed 13 silicate grains from Acfer 094 and detected one grain with positive and one grain with negative $\delta^{54/56}$Fe, +128±22 and -140±52, respectively, relative to solar ratios. From five silicate grains analyzed by Nguyen and Messenger (2014) one grain showed a $\delta^{57/56}$Fe deficit of -135±73 and one grain a small $\delta^{54/56}$Fe deficit of -37±19. Ong and Floss (2015) analyzed 21 silicate and oxide grains from Acfer 094 and reported negative $\delta^{57/56}$Fe in five grains, ranging from about -200 to -85. One grain revealed a positive $\delta^{57/56}$Fe value of ~100. The grain with the largest $\delta^{57/56}$Fe deficit also shows negative $\delta^{54/56}$Fe of about -100. In summary, single grains from chondrites occasionally display clear isotope anomalies. However, these anomalies are not revealed in the bulk samples or leachates and residues, either because their contribution to the bulk Fe reservoir is too little and hence, irrelevant and likely also because the anomalies of single grains cancel out to some extent.

1.2.2. Titanium isotopes

Bulk chondrites: Niederer et al. (1981) were the first to search for isotope anomalies in bulk samples of Allende (CV3). Their results of -0.7±1.6 for $\varepsilon^{47/48}\text{Ti}_{(46/48)}$, 1.6±1.1 for $\varepsilon^{49/48}\text{Ti}_{(46/48)}$ and 1.4±1.3 for $\varepsilon^{50/48}\text{Ti}_{(46/48)}$ display no evidence for nucleosynthetic Ti isotope anomalies. Niederer et al. (1985) then studied also various other chondrites and only found excess $\varepsilon^{50/48}\text{Ti}_{(46/48)}$ of 15±2.6 in Leoville (CV3), 4.7±0.9 in Murchison (CM) and 5.1±1.3 in Adelaide (CM2). More than 20 years later, and with significantly improved analytical precision, Leya et al. (2008) measured positive $\varepsilon^{50/47}\text{Ti}_{(49/47)}$ between 2.5 and 4.3 for Allende. They also resolved a slight elevation in $\varepsilon^{46/47}\text{Ti}_{(49/47)}$ in Orgueil (CI1) and Renazzo (CR2) with values up to 3.4. Further, they did not find nucleosynthetic Ti isotope anomalies in ordinary chondrite Forest Vale (H4). Trinquier et al. (2009) reported variable excesses in $\varepsilon^{46/47}\text{Ti}_{(49/47)}$ and $\varepsilon^{50/47}\text{Ti}_{(49/47)}$ of various bulk carbonaceous chondrites and uniform deficits in ordinary chondrites, relative to

the Earth. Their results are shown in Figure 3.5 since their paper does not report tabulated values. High-precision measurements by Zhang et al. (2011) of Allende (CV3) showed slightly elevated $\varepsilon^{46/47}Ti_{(49/47)}$ of up to 0.68±0.11 and larger excesses in $\varepsilon^{50/47}Ti_{(49/47)}$ of up to 3.68±0.25, $\varepsilon^{48/47}Ti_{(49/47)}$ appeared normal. The same isotope pattern were found for Murchison (CM2) with $\varepsilon^{46/47}Ti_{(49/47)}$ of 0.47±0.15, $\varepsilon^{50/47}Ti_{(49/47)}$ of 2.83±0.19 and normal $\varepsilon^{48/47}Ti_{(49/47)}$. Ordinary chondrite St. Severin (LL6) showed, beside normal $\varepsilon^{46/47}Ti_{(49/47)}$ and $\varepsilon^{48/47}Ti_{(49/47)}$, a slightly negative $\varepsilon^{50/47}Ti_{(49/47)}$ of up to -0.79±0.34. They normalized their results to $^{46/48}Ti$ as well, which revealed a slightly negative $\varepsilon^{47/48}Ti_{(46/48)}$ of up to -0.35±0.06, an elevation in $\varepsilon^{49/48}Ti_{(46/48)}$ of up to 0.48±0.14 and $\varepsilon^{50/48}Ti_{(46/48)}$ of up to 4.53±0.38 for Allende and Murchison. St. Severin did not show any nucleosynthetic anomalies but a slightly negative $\varepsilon^{50/48}Ti_{(46/48)}$ of up to -0.90±0.37.

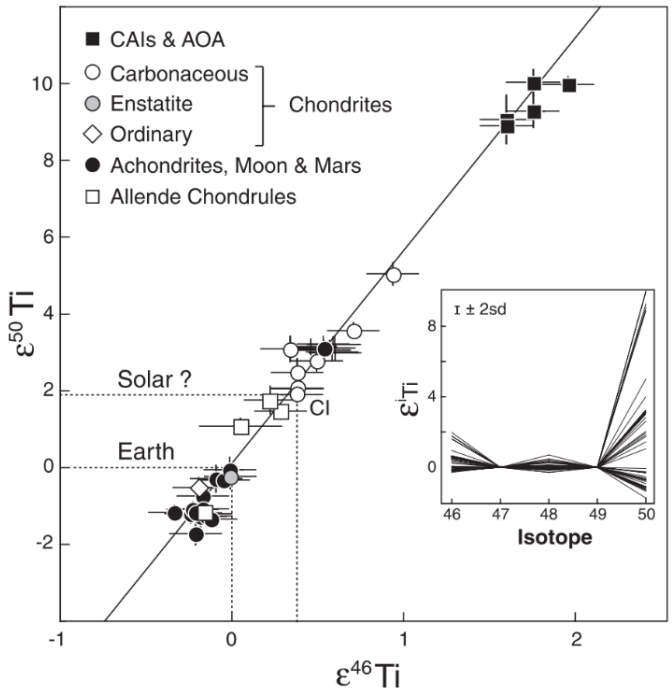

Figure 3.5. Titanium isotope measurements of bulk solar system materials by Trinquier et al. (2009) shown as $\varepsilon^{46/47}Ti_{(49/47)}$ and $\varepsilon^{50/47}Ti_{(49/47)}$. Error bars represent the external reproducibility or the internal precision, whichever is larger.

Sequential leachates: Leya et al. (2008) implemented leaching experiments at 2 g of Allende, applying 50% HAc (= CH_3COOH) in the first leach step, 4 M HNO_3 in the second leach step, 6 M HCl in the third leach step and 13.5 M HF + 3 M HCl in the fourth leach step. Results showed positive $\varepsilon^{46/47}Ti_{(49/47)}$ and $\varepsilon^{48/47}Ti_{(49/47)}$ for the first leach step of 3.7±2.0 and 2.3±0.3 respectively. Values of $\varepsilon^{50/47}Ti_{(49/47)}$ are about 3.3 in the third and fourth step. All other leachates have normal values. Trinquier et al. (2009) applied several leaching steps to Orgueil (CI1) using

procedures adapted from Podosek et al. (1997). During leach step *3a* and *3b*, 0.5 M and 1 M HNO_3 respectively, were applied, during leach step *3c*, 4 M HNO_3 was applied, for leach step *3d*, 8 M HNO_3 was used, for leach step *3e*, 6 M HCl was used and for leach step *3f*, 6 M HCl was applied combined with high temperature of 80°C. In leach step *4*, 6 M HCl + 27 M HF was applied at 100°C. Results are shown in Figure 3.6 since their paper does not report tabulated values. The plot reveals a stepwise increase of $\varepsilon^{46/47}Ti_{(49/47)}$ up to ~0.8 and $\varepsilon^{50/47}Ti_{(49/47)}$ up to ~4, with a slight decrease in leach step *3f*. In leachate *4*, $\varepsilon^{50/47}Ti_{(49/47)}$ rises to ~10 while $\varepsilon^{46/47}Ti_{(49/47)}$ remains ~0.5.

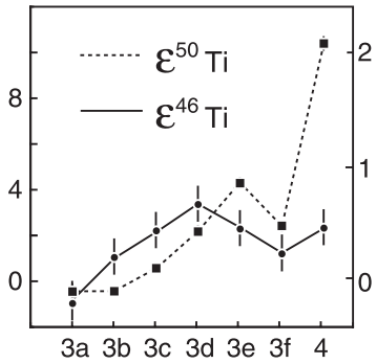

Figure 3.6. Titanium isotope measurements of sequential leached Murchison by Trinquier et al. (2009) shown as $\varepsilon^{46/47}Ti_{(49/47)}$ and $\varepsilon^{50/47}Ti_{(49/47)}$. Error bars represent the external reproducibility or the internal precision, whichever is larger.

Refractory inclusions: Analyses of Allende FUN inclusions by Niederer et al. (1981) and Papanastassiou and Brigham (1989) revealed $\varepsilon^{47/48}Ti_{(46/48)}$ ranging from 6.4 to 13.1, $\varepsilon^{49/48}Ti_{(46/48)}$ ranging from -14.9 to 20.1 and $\varepsilon^{50/48}Ti_{(46/48)}$ ranging from -203.3 to 38.9. Allende (and two Leoville (CV3)) non-FUN CAI analyses by Niederer et al. (1981); Niederer et al. (1985) and Birck and Allègre (1984) showed $\varepsilon^{47/48}Ti_{(46/48)}$ of -3.8 to 2.0, $\varepsilon^{49/48}Ti_{(46/48)}$ of -4.5 to 0.7 and $\varepsilon^{50/48}Ti_{(46/48)}$ of 2.4 to 17.0. These results are in good agreement with results by (Niemeyer and Lugmair, 1981) for Allende inclusions with $\varepsilon^{47/46}Ti_{(49/46)}$ of -2.9 to -0.1, $\varepsilon^{48/46}Ti_{(49/46)}$ of -1.4 to 2.1 and $\varepsilon^{50/46}Ti_{(49/46)}$ of 6.6 to 31.2. Leya et al. (2009); Trinquier et al. (2009); Williams et al. (2016) and Simon et al. (2017) analyzed Allende (plus one NWA (CV3) and two Efremovka (CV3)) non-FUN CAIs and reported $\varepsilon^{46/47}Ti_{(49/47)}$ ranging from -1.9 to 4.0, $\varepsilon^{48/47}Ti_{(49/47)}$ ranging from -3.91 to 1.4 and $\varepsilon^{50/47}Ti_{(49/47)}$ ranging from 0.4 to 41.6. One exception was Allende CAI grain CMS-1 analyzed by Williams et al. (2016) with values of -13.9±1.7, 0.2±0.7 and -51.3±6.9 for $\varepsilon^{46/47}Ti_{(49/47)}$, $\varepsilon^{48/47}Ti_{(49/47)}$ and $\varepsilon^{50/47}Ti_{(49/47)}$ respectively.

1.2.3. Chromium isotopes

Bulk chondrites: Carbonaceous chondrites were analyzed for nucleosynthetic Cr isotope anomalies by Birck and Allègre (1984); Papanastassiou (1986); Rotaru et al. (1992); Shukolyukov and Lugmair (2006); Trinquier et al. (2007); Qin et al. (2010) and Petitat et al. (2011). Their measurements covered 19 carbonaceous chondrites including Allende, Murchison and Orgueil. All results of $\varepsilon^{53/52}Cr_{(50/52)}$ were zero within error. Results of $\varepsilon^{54/52}Cr_{(50/52)}$ showed a slightly positive value of up to 1.7. Trinquier et al. (2007) and Qin et al. (2010) also analyzed ordinary and enstatite chondrites. Results for eight ordinary chondrites, including L, LL and H chondrites, showed $\varepsilon^{53/52}Cr_{(50/52)}$ of 0.19 to 0.21 and $\varepsilon^{54/52}Cr_{(50/52)}$ of -0.47 to -0.28. From eleven analyzed enstatite chondrites, none of them showed anomalies in $\varepsilon^{54/52}Cr_{(50/52)}$. Only for six enstatite chondrites $\varepsilon^{53/52}Cr_{(50/52)}$ data was evaluated and showed slightly positive values from 0.14 to 0.21.

Sequential leachates: Rotaru et al. (1992) implemented stepwise dissolution of chondrite samples for Cr isotope analyses and found consistent Cr isotope pattern for different chondrite groups. Analyzed CI1 chondrites were Orgueil, Alais and Ivuna. Leachates of CI1 chondrites gained from acetic acid showed a slightly positive $\varepsilon^{53/52}Cr_{(50/52)}$ up to ~4. Leachates gained from nitric acid, showed a normal $\varepsilon^{53/52}Cr_{(50/52)}$. Leachates gained from acetic and nitric acid, respectively, showed negative $\varepsilon^{54/52}Cr_{(50/52)}$ of up to ~-7.5. By using HCl + HF or HBr(or HNO_3)+HF respectively, $\varepsilon^{53/52}Cr_{(50/52)}$ changed to negative values of up to ~-1.4 and $\varepsilon^{54/52}Cr_{(50/52)}$ showed positive values of up to ~101. Analyzed CM2 chondrites were Murchison, Murray and B-7904. Leachates of CM2 chondrites show a similar pattern for $\varepsilon^{54/52}Cr_{(50/52)}$ from ~-17.6 using acetic acid up to ~+27.5 in following leach steps, with highest values using HBr+HF. CM2 leachates show normal $\varepsilon^{53/52}Cr_{(50/52)}$. Other carbonaceous chondrites revealed positive $\varepsilon^{53/52}Cr_{(50/52)}$ of up to ~4.3 in leachates only from acetic acid (Allende CV3, Felix CO3.3) or in leachates from acetic and nitric acid (Karoonda CK4, Coolidge C4-ung.) of up to ~32. $\varepsilon^{54/52}Cr_{(50/52)}$ for named chondrites varies from 0 to ~13.5 with highest values gained by using acetic acid. Podosek et al. (1997) analyzed sequential leachates from Orgueil (CI1) and did not find any anomalies for $\varepsilon^{53/52}Cr_{(50/52)}$. Results for $\varepsilon^{54/52}Cr_{(50/52)}$ followed a similar pattern as seen in previous experiments, with negative values of up to ~-7 when using 50% acetic or 4 M nitric acid respectively, and positive values of up to ~126 using 6 M HCl. Trinquier et al. (2007) analyzed leachates from Orgueil (CI1), Murchison (CM2), Renazzo (CR2), Leoville (CV3), Allende (CV3), Felix (CO3) and Lance (CO3) following the leaching procedure by Rotaru et al. (1992) and a second procedure adapted from Podosek et al. (1997) for a second experiment with Orgueil. Experiments revealed $\varepsilon^{54/52}Cr_{(50/52)}$ pattern similar to those by Rotaru

et al. (1992), showing a sequence from negative values of up to ~-14 to positive values of up to ~52 or ~90 in Orgueil experiment II, respectively for all analyzed chondrites except Allende, Felix and Lance. Allende, Felix and Lancé revealed positive values from ~4 in the first leach step, decreasing with every further leach step to ~0 in the residue for $\varepsilon^{54/52}Cr_{(50/52)}$. Wang et al. (2011) were leaching ordinary chondrite Semarkona (LL3) and carbonaceous chondrites Orgueil (CI1) and Murchison (CM2) using different procedures per chondrite. Using 50% acetic acid and 25 % HNO3, respectively at room temperature for the first two leachates of all three chondrites, results show negative $\varepsilon^{54/52}Cr_{(50/52)}$ from -2.5 to -15.5. For third leachates, 6 M HCl was used. Semarkona and Orgueil showed negative $\varepsilon^{54/52}Cr_{(50/52)}$ of up to -5, Murchison showed a positive value of ~14.5. For leach step four and five, they used 6 M HCl at 40°C and gained positive results for $\varepsilon^{54/52}Cr_{(50/52)}$ of ~4.4 and ~8 for Semarkona and Orgueil respectively. Murchison showed a higher value of ~34.2. Their fifth leachate using 6 M HCl at 80°C showed $\varepsilon^{54/52}Cr_{(50/52)}$ of ~3.5, ~71 and 21.1 for Semarkona, Orgueil and Murchison, respectively. A sixth leach step only was applied to Semarkona using concentrated HF + HCl at 100°C showing $\varepsilon^{54/52}Cr_{(50/52)}$ of ~1 and Orgueil using 9 M HCl at 80°C showing $\varepsilon^{54/52}Cr_{(50/52)}$ of ~98. Residues were digested using concentrated HF+HNO_3 at room temperature for Semarkona and concentrated HF + HCl at 100°C for Orgueil. Semarkona showed normal $\varepsilon^{54/52}Cr_{(50/52)}$ within error, Orgueil showed $\varepsilon^{54/52}Cr_{(50/52)}$ of ~33. All leachates from all three chondrites gave normal $\varepsilon^{53/52}Cr_{(50/52)}$ except Semarkona had slightly positive values from 0.38 to 0.99 in leachates one (acetic acid), two (HNO_3) and six (conc. HF + HCl). Petitat et al. (2011) leached carbonaceous chondrites Orgueil (CI1) and Targish Lake (CI2) and gained a negative $\varepsilon^{54/52}Cr_{(50/52)}$ in leachates one and two using acetic acid and leachate three using 4 M HNO_3 of -16.14 to -5.13. Largest anomalies were revealed in leachate four using 6 M HCl with $\varepsilon^{54/52}Cr_{(50/52)}$ of up to 139. Leachate five using HNO_3 + HF also revealed positive $\varepsilon^{54/52}Cr_{(50/52)}$ of up to 18.25. In both chondrites $\varepsilon^{53/52}Cr_{(50/52)}$ was slightly positive in first and second leachates with values from 1.00 to 11.47, normal within error in the third leachates and negative in the fourth and fifth leachates with values of -1.45 to -0.64.

Refractory inclusions: Refractory FUN inclusions from Allende (CV3) were analyzed by Papanastassiou (1986) and Papanastassiou and Brigham (1989) and revealed positive $\varepsilon^{53/52}Cr_{(50/52)}$ from 0.6 to 16.2 and a wide range of $\varepsilon^{54/52}Cr_{(50/52)}$ with values from -151.0 to 48.5. Non-FUN inclusions from Allende (CV3) were analyzed by Birck and Allègre (1984); Papanastassiou (1986); Birck and Lugmair (1988); Trinquier et al. (2007) and Chen and Papanastassiou (2014) with $\varepsilon^{53/52}Cr_{(50/52)}$ ranging from -2.1 to -0.4 and $\varepsilon^{54/52}Cr_{(50/52)}$ ranging from 0.46 to 9.72.

It should be noted, that due to the decay of the short-lived radionuclide ^{53}Mn to ^{53}Cr, Cr isotope variations are independent of each other (Rotaru et al., 1992). Except for FUN inclusions, of which large ^{53}Cr isotope effects are related to nucleosynthetic effects (Papanastassiou, 1986), ^{53}Cr variations are assumed to be generally related to the Mn/Cr elemental ratio (Birck et al., 1999). One explanation for a variable ^{53}Cr isotope distribution in the solar system is given by Birck et al. (1999) and Trinquier et al. (2008) who claim a Mn/Cr fractionation within the protoplanetary disk. A second explanation is given by Shukolyukov and Lugmair (2000) who suggested radial heterogeneity of ^{53}Mn in the early solar system.

1.2.4. Nickel isotopes

Bulk chondrites: Morand and Allègre (1983) analyzed several carbonaceous chondrites, ordinary chondrites and enstatite chondrites for nucleosynthetic Ni isotope anomalies. Results for $\varepsilon^{61/60}Ni_{(58/60)}$, $\varepsilon^{62/60}Ni_{(58/60)}$ and $\varepsilon^{64/60}Ni_{(58/60)}$ did not show any anomalies within error. More precise measurements by Regelous et al. (2008) revealed $\varepsilon^{60/61}Ni_{(58/61)}$ for carbonaceous chondrites ranging from -0.216 in NWA 801 (CR2) to -0.004 in Orgueil (CI1) and $\varepsilon^{62/61}Ni_{(58/61)}$ ranging from 0.049 in Leoville (CV3) to 0.253 in Orgueil (CI1). Further, they analyzed ordinary and enstatite chondrites, which showed $\varepsilon^{60/61}Ni_{(58/61)}$ ranging from -0.065 in Chainpur (LL3.3) to +0.004 in Krymka (LL3.1) and $\varepsilon^{62/61}Ni_{(58/61)}$ ranging from -0.089 in Abee (EH4) to +0.050 in St. Mark's (EH5). Bizzarro et al. (2007) analyzed carbonaceous chondrites Orgueil (CI1), Allende (CV3), Renazzo (CR2) and Murchison which showed normal $\varepsilon^{60/58}$Ni and an average $\varepsilon^{62/58}$Ni of 0.335±0.054. Tang and Dauphas (2012) presented two Ni data sets, one internal normalised to $^{61/58}$Ni and one internal normalised to $^{63/58}$Ni. Allende (CV3) and Murchison (CM2) showed a negative $\varepsilon^{60/58}Ni_{(61/58)}$ of -0.14 to -0.13, Khairpur (EL6), St. Mark's (EH5) and Chainpur (LL3.4) were zero within error. Results were similar for $\varepsilon^{60/58}Ni_{(62/58)}$ with -0.20 to -0.17 for the two carbonaceous chondrites. All analyzed chondrites showed normal $\varepsilon^{61/58}Ni_{(62/58)}$ and $\varepsilon^{62/58}Ni_{(61/58)}$. Positive $\varepsilon^{64/58}Ni_{(61/58)}$ and $\varepsilon^{64/58}Ni_{(62/58)}$ was found for Allende and Murchison with values up to 0.30 and 0.15 respectively. For Khairpur and St. Mark's those values were normal. They did not publish ^{64}Ni data for Chainpur.

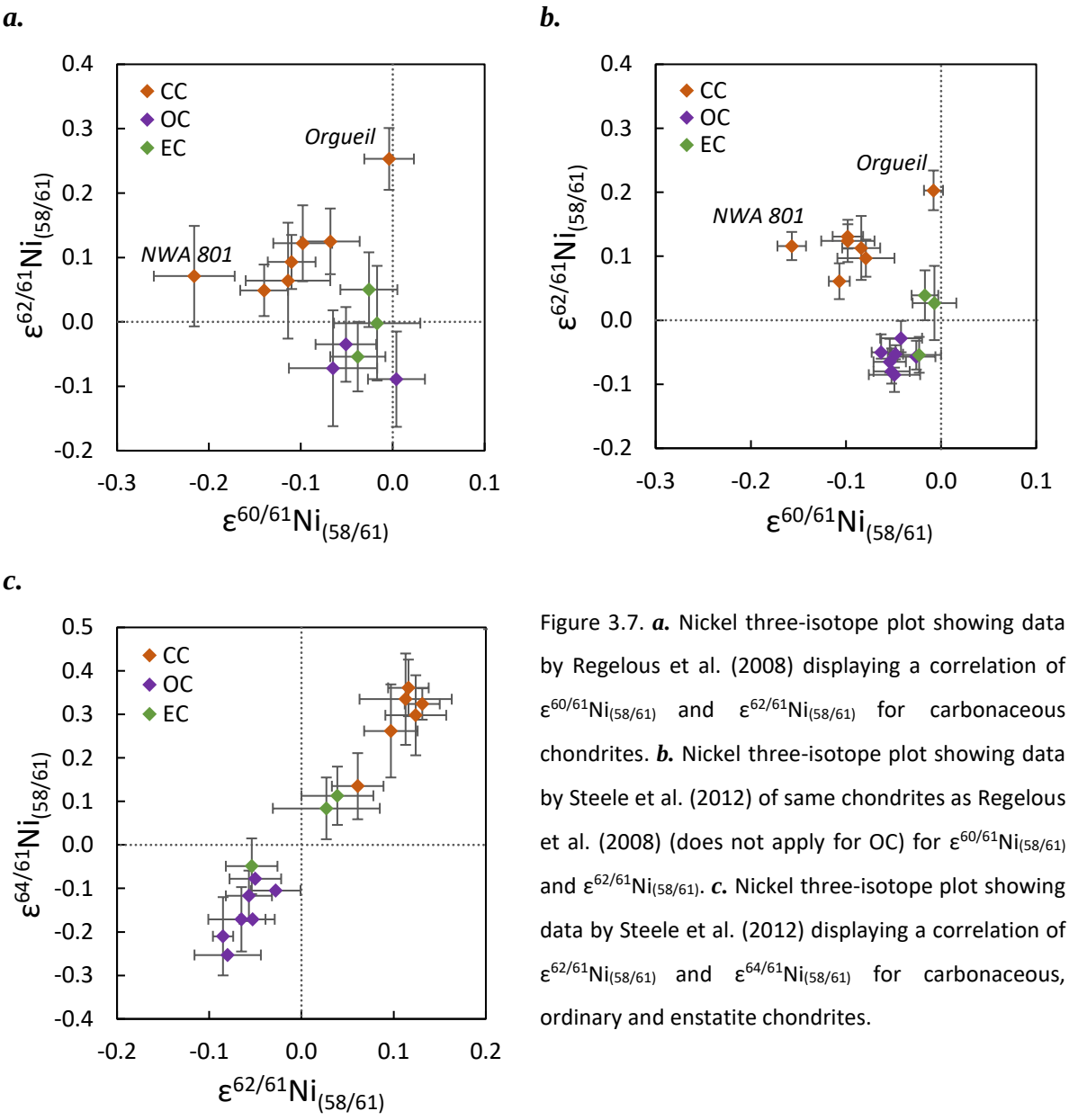

Figure 3.7. ***a.*** Nickel three-isotope plot showing data by Regelous et al. (2008) displaying a correlation of $\varepsilon^{60/61}Ni_{(58/61)}$ and $\varepsilon^{62/61}Ni_{(58/61)}$ for carbonaceous chondrites. ***b.*** Nickel three-isotope plot showing data by Steele et al. (2012) of same chondrites as Regelous et al. (2008) (does not apply for OC) for $\varepsilon^{60/61}Ni_{(58/61)}$ and $\varepsilon^{62/61}Ni_{(58/61)}$. ***c.*** Nickel three-isotope plot showing data by Steele et al. (2012) displaying a correlation of $\varepsilon^{62/61}Ni_{(58/61)}$ and $\varepsilon^{64/61}Ni_{(58/61)}$ for carbonaceous, ordinary and enstatite chondrites.

Only carbonaceous chondrites showed positive $\varepsilon^{62/61}Ni_{(58/61)}$ ranging from 0.049 to 0.253. The Ni three-isotope plot shows a correlation between $\varepsilon^{60/61}Ni_{(58/61)}$ and $\varepsilon^{62/61}Ni_{(58/61)}$ for carbonaceous chondrite samples (Figure 3.7a). Steele et al. (2012) analyzed the same carbonaceous and enstatite chondrite as Regelous et al. (2008), but seven ordinary chondrites of which only two are similar to studies of Regelous et al. (2008). The more precise results show similar pattern as previous studies, with negative $\varepsilon^{60/61}Ni_{(58/61)}$ for all chondrite samples, carbonaceous chondrites ranging from -0.157 to -0.008, ordinary chondrites ranging from -0.063 to -0.026 and enstatite chondrites ranging from -0.023 to -0.007. Results for $\varepsilon^{62/61}Ni_{(58/61)}$ are positive for carbonaceous chondrites ranging from 0.061 to 0.203, negative for ordinary chondrites ranging from -0.085 to -0.028 and zero within error for enstatite chondrites. The

same pattern applies for $\varepsilon^{64/61}Ni_{(58/61)}$ with positive values for carbonaceous chondrites ranging from 0.135 to 0.585, negative values for ordinary chondrites ranging from -0.253 to -0.0078 and normal values for enstatite chondrites. The Ni three-isotope plot shows a distinct correlation of $\varepsilon^{62/61}Ni_{(58/61)}$ and $\varepsilon^{64/61}Ni_{(58/61)}$ (Figure 3.7b and Figure 3.7c).

Refractory inclusions: Morand and Allègre (1983) analyzed nine non-FUN inclusions of Allende and could not resolve any anomalies in $\varepsilon^{61/60}Ni_{(58/60)}$, $\varepsilon^{62/60}Ni_{(58/60)}$ and $\varepsilon^{64/60}Ni_{(58/60)}$. More precise measurements by Birck and Lugmair (1988) revealed small anomalies in non-FUN Allende inclusions in at least three of nine samples, with $\varepsilon^{60/58}Ni_{(61/58)}$ of up to 2.04, $\varepsilon^{62/58}Ni_{(61/58)}$ of up to 2.4 and $\varepsilon^{64/58}Ni_{(61/58)}$ of up to 3.4. Allende FUN inclusions analyzed by Chen and Papanastassiou (2014) revealed large anomalies in 2 of 3 FUN inclusion with $\varepsilon^{64/58}Ni_{(61/58)}$ of up to 58.2.

2. METHODS

2.1. Leaching and sample preparation

All samples were powdered in an agate ball mill for 1.5 minutes. About 100 to 1200 mg of a terrestrial basalt sample from La Palma (LP8), chondrites (Cold Bokkeveld CM2, Allende CV3, Kainsaz CO3, QUE 97008 L3, Indarch EH4) and 5 g of Murchison (CM2) were used for the leaching experiments. To this end, the samples were dissolved in acid mixtures of increasing strengths and temperature, thereby dissolving variable combinations of increasingly refractory chondrite phases.

The three different leaching procedures applied are described below and listed in Table 3.1. After each leaching step, the dissolved portion was dried down three times with 2 droplets of 16 M HNO_3, followed by 2 droplets of 6 M HCl. All L2 leachates and all residues were further treated with 1 ml $HClO_4$ to oxidize organic material and re-dissolve secondary fluoride precipitates. An additional Allende CV3 bulk sample was dissolved using 14 M HNO_3 + 29 M HF in a 1:1 mixture at 180°C for 3 days in Savillex™ beakers placed inside Parr™ pressure digestion vessels. Then each leachate, residue and bulk sample was dried down in 14 M HNO_3 three times, followed by re-dissolution and drying down in 6 M HCl. An aliquot of the solution was then equilibrated in 6 M HCl + 0.06 HF for bulk chondrite measurements.

Aliquots of these solutions and the un-leached bulk Allende solution were then used for element concentration measurements.

The following three leaching recipes were used:

a. The first leachate was obtained from dissolving the sample in 6 M HCl and 0.06 M HF on a hotplate at 80°C for 24 h and then split into leachate L1 and the remaining residue. For the second leachate, the remaining sample residue was dissolved in 14 M HNO_3 and 24 M HF in a proportion of 20:1 and placed on a hotplate at 120°C for 24 h and then split into leachate L2 and residue R. Residues R were completely dissolved in Savillex™ beakers placed inside Parr™ pressure digestion vessels for 3-4 days at 180°C using 14 M HNO_3 and 24 M HF in a 1:1 ratio. This last step of treating the residues R is the same for the leachate procedures of ***b.*** and ***c.***.

b. The second recipe is very similar to the first and was used only for Kainsaz. No HF was used for L1 leaching. In the second leach step, 14 M HNO_3 and 24 M HF in a proportion of 3:1 was added to the remaining residue.

c. The third recipe consisted of four leaching steps and was applied to Murchison only. In the first leach step, the sample was treated with 0.1 M HCl and 0.001 M HF for 24 h at room temperature and then split into leachate L1 and a residue. For the next leach step, the remaining residue was treated with 4 M HNO_3 and 0.001 M HF for 5 days at room temperature and then split into leachate L2 and the residue. For the third leach step, the residue was treated with 6 M HCl and 0.001 M HF at 80°C for 24 h and split into leachate L3 and the residue. For the last leach step, the residue was treated with 3 M HCl and 14 M HF at 120°C for 3 days and then split into L4 and residue R.

Table 3.1. Leaching procedure for chondritic and terrestrial powder samples.

	a.		
L1	6 M HCl + 0.06 M HF	80°C	24 h
L2	14 M HNO3 + 24 M HF (20:1)	120°C	24 h
R	14 M HNO3 + 24 M HF (1:1)*	180°C	3-4 d

	b.		
L1	6 M HCl	80°C	24 h
L2	14 M HNO3 + 24 M HF (3:1)	120°C	24 h
R	14 M HNO3 + 24 M HF (1:1)*	180°C	3-4 d

	c.		
L1	0.1 M HCl+0.001 M HF	20°C	24 h
L2	4 M HNO3 + 0.001 M HF	20°C	5 d
L3	6 M HCl + 0.001 M HF	80°C	24 h
L4	3 M HCl + 14 M HF	120°C	3 d
R	14 M HNO3 + 24 M HF (1:1)*	180°C	3-4 d

a. applied to La Palma basalt 8, Allende, Cold Bokkeveld, Indarch and QUE 97008; ***b.*** applied to Kainsaz; ***c.*** used for Murchison.
*pressure digestion

More details on the leaching procedures and sample treatment can be found in Elfers et al. (2018).

2.2. Iron separation via column chemistry

Iron was separated via column chromatography using 1 ml AG1-X8 anion exchange resin in *Biorad* columns following modified separation procedures by Dauphas et al. (2004). The columns were loaded with 500 µl sample solution with Fe concentrations as listed in Table A.3. By far most matrix elements were eluted from the column with a total of 7.5 ml (6 ml for Indarch which was separated during an earlier batch of chemistry and a slightly varied procedure) 6 M HCl. Then 0.4 ml of 0.4 M HCl was added to the column to check for premature elution of Fe before the main cut. Iron was subsequently eluted using a total of 4.5 ml of 0.4 M HCl (4 ml of 0.05 M HCl for Indarch; Table 3.2). The Fe cuts were treated with HNO_3 and H_2O_2 to remove possible organic remnants, and diluted for isotope ratio measurements in 0.28 M HNO_3.

Table 3.2. Chemical separation procedures for iron.

a.

	ml	acid
load	0.5	6 M HCl
matrix	1.5	6 M HCl
	3.0	6 M HCl
	3.0	6 M HCl
	0.4	0.4 M HCl
Fe	1.5	0.4 M HCl
	3.0	0.4 M HCl

a. used for LP 8, Allende, Kainsaz, Cold Bokkeveld, QUE 97008 and Murchison.
b. used for Indarch.

b.

	ml	acid
load	0.5	6 M HCl
matrix	0.5	6 M HCl
	0.5	6 M HCl
	1.0	6 M HCl
	2.0	6 M HCl
	2.0	6 M HCl
Fe	0.5	0.05 M HCl
	0.5	0.05 M HCl
	1.0	0.05 M HCl
	2.0	0.05 M HCl

2.3. Mass spectrometry

Element concentration measurements were carried out using the Thermo ElementXR sector-field ICP-MS equipped with a PFA Scott type spray chamber at the Steinmann Institute Bonn, Germany using methods similar to those in Braukmüller et al. (2018). Iron concentrations are given in µg Fe and are listed in Table A.3, together with the fraction of Fe in each leachate or residue, respectively, and the amount of µg Fe loaded onto the column for chemical separation.

Iron isotopes were measured using the Neptune multiple collector-inductively coupled plasma mass spectrometer (MC-ICP-MS) at the Steinmann Institute in Bonn, Germany. The instrument was operated with an Elemental Scientific SC-2 autosampler, a Thermo SIS glass spray

chamber, standard Al cones and a MicroMist glass nebulizer with an uptake rate of about 150 µl min^{-1}. Ion beams were collected in Faraday detectors using amplifiers with different resistors in their feedback loops: ^{53}Cr (L3; 10^{12} Ω), ^{54}Fe (L2; 10^{11} Ω), ^{56}Fe (center cup; 10^{10} Ω), ^{57}Fe (H1; 10^{11} Ω), ^{58}Fe (H2; 10^{11} Ω) and ^{60}Ni (H4; 10^{12} Ω). Gain calibration and 1000 s baseline measurements were repeated daily. Analyses were conducted in medium resolution mode to screen out polyatomic interferences (Weyer and Schwieters, 2003). To this end, all ion beams were collected near the low mass edge of the Faraday cups. Before every measurement session, the Faraday cups were positioned such that all interference free peak shoulders (plateaus) in high and low mass cups overlapped well with that of ^{56}Fe in the center cup. To ensure perfectly similar measurement conditions, several aliquots of 1000 µg of the in-house Alfa Aesar Fe standard (Lot: 61201004), were processed through the chemistry in Table 3.2a along with the samples and all measurement solutions were prepared using the same batch of acid (0.28 M HNO_3). The in-house Fe standard solution used for sample bracketing was also used to center the ^{56}Fe ion beam in the center cup. Using a measurement routine, we then inferred which center cup mass position provides the most reproducible results (usually 55.901 or 55.902). During the measurements, peak centers were repeated about every 3 hours, always using the Fe standard solution. To correct for possible background contributions, background solutions (0.28 M HNO_3) were run for 126 s right before the 60 s uptake of sample and standard solutions. Samples and standards were then integrated for 8.4 minutes (120 cycles of 4.2 s). After measurements, the system was rinsed for 4 minutes, again with 0.28 M HNO_3.

To achieve high intensities, in particular for ^{58}Fe, solutions were prepared with up to 25 µg/ml Fe. Measured intensities ranged from 236 to 470 V* for ^{56}Fe (Table A.4) and from 0.77 to 1.53 V for ^{58}Fe. Note that V* refers to the voltages displayed by the instrument software, i.e. calculated as if 10^{11} Ω resistors were applied rather than real measured voltages (Pfeifer et al., 2017), which facilitates easy comparison. Sample and standard solutions were well matched in intensity. In only five cases did the intensity differ by more than 10 % and up to 32 % (Table A.4).

Ion beams for ^{53}Cr and ^{60}Ni were monitored to correct for the isobaric interferences of ^{54}Cr on ^{54}Fe and ^{58}Ni on ^{58}Fe. Mass discrimination correction was based on the exponential law (Russell et al., 1978) using $^{57/54}Fe = 0.36255$. To mimic the instrumental mass discrimination that affects the natural $^{54/53}Cr$ and $^{58/60}Ni$ ratios used for the interference correction, these ratios were "biased" again using the exponential law and the not interference corrected ratio of $^{57/54}Fe$. All data evaluation was made offline.

Data of $^{56/54}$Fe and $^{58/54}$Fe are reported in δ‘ and μ notation, according to:

$$\delta'\left(^{x/54}Fe\right)_{sample} = ln\left(\frac{\left(^{x/54}Fe\right)_{sample}}{\left(^{x/54}Fe\right)_{standard}}\right) * 1000 \quad (4)$$

$$\mu\left(^{x/54}Fe_{(57/54)}\right)_{sample} = \left[\left(\frac{R_{\left(^{x/54}Fe\right)_{sample}}}{R_{\left(^{x/54}Fe\right)_{standard}}}\right) - 1\right] * 1\,000\,000 \quad (5)$$

with:

$$R_{\left(^{x/54}Fe\right)_{measured}} = \left(^{x/54}Fe\right)_{measured} * \left(\frac{m_{(^{x}Fe)}}{m_{(^{54}Fe)}}\right)^{f_{\left(^{57/54}Fe\right)}} \quad (6)$$

and:

$$f_{\left(^{57/54}Fe\right)} = ln\left(\frac{\left(^{57/54}Fe\right)_{natural}}{\left(^{57/54}Fe\right)_{measured}}\right) \Big/ ln\left(\frac{m_{(^{57}Fe)}}{m_{(^{54}Fe)}}\right) \quad (7)$$

where x = ^{56}Fe or ^{58}Fe, respectively and $(^{57/54}Fe)_{natural}$ = 0.36255.

The effect of interference correction for ^{54}Cr does not exceed 100 ppm except for QUE R-6, which showed an effect of 229 ppm. Interference corrections for ^{54}Cr and ^{58}Ni on $^{58/54}$Fe show a much higher effect with a maximum of 1652 ppm on COBO L2-3 (Table A.4). Test calculations showed that deviations of ±1 % from the assumed natural $^{54/53}$Cr produce only insignificant deviations of up to ±0.7 ppm for $\mu^{56/54}Fe_{(57/54)}$. Likewise, ±1 % deviations from the assumed natural $^{58/60}$Ni produce systematic offsets up to 14 to 16 ppm for the $\mu^{58/54}Fe_{(57/54)}$ ratios for the three measurements with the largest interference correction, ALL R, CO BO L2 and CO BO L2 vs. L1 (Table A.4). The calculated offsets approve that corrections with given “true” Ni and Cr ratios are accurate. The mass-dependent variations of the Fe isotopes are also provided as linearized δ‘-values (Hulston and Thode, 1965).

The precision of the sample measurements is given as twice the standard error of the mean (s.e. in μ or δ‘-notation). However, the samples are measured relative to the average of two standard measurements. To include the uncertainty associated with the average standard value, the average of the two bracketing standard s.e. values were multiplied with 0.70711 ($= \sqrt{120}/\sqrt{240}$, where 120 = number of integrations for one standard measurement) to account for the fact that the standard deviation of the mean improves if 240 rather than 120 integrations are made. The s.e. uncertainties of the standard average and sample measurement were then propagated. This calculation appears reasonable for the internally normalized data in

μ-notation but provides only a lower limit for the uncertainty of the stable isotope measurements (δ-values), as it does not take possible drift or matrix effects into account. A better representation of the intermediate precision of the stable isotope measurements is the data. For n = 12, with measurements distributed over several months, analyses of a 25 µg ml^{-1} IRMM-014 Fe standard solution resulted in an intermediate precision of 2 s.d. = 0.16 ‰ for $\delta'^{56/54}Fe$ and 0.34 ‰ for $\delta'^{58/54}Fe$. For $\mu^{56/54}Fe_{(57/54)}$ 2 s.d. = 13 ppm and for $\mu^{58/54}Fe_{(57/54)}$ 2 s.d. = 16 ppm.

Two data sets were evaluated, one with and one without subtraction of the background signal. The effect of background correction for $\mu^{56/54}Fe_{(57/54)}$ is significant and reduces the small offset observed for terrestrial samples relative to the bracketing standard solution. With few exceptions, almost all chondrite leachate and residue samples are shifted closer to zero and offsets are lowered. With the exception of bulk Allende samples, the background correction causes a reduced scatter for $\mu^{56/54}Fe_{(57/54)}$. However, subtraction of background noise on $\mu^{58/54}Fe_{(57/54)}$ increases the scatter for repeated sample measurements but does not change the general pattern of the data cloud (Figure 3.8). Therefore, data set for $\mu^{58/54}Fe_{(57/54)}$ refers to that without subtraction of background signals.

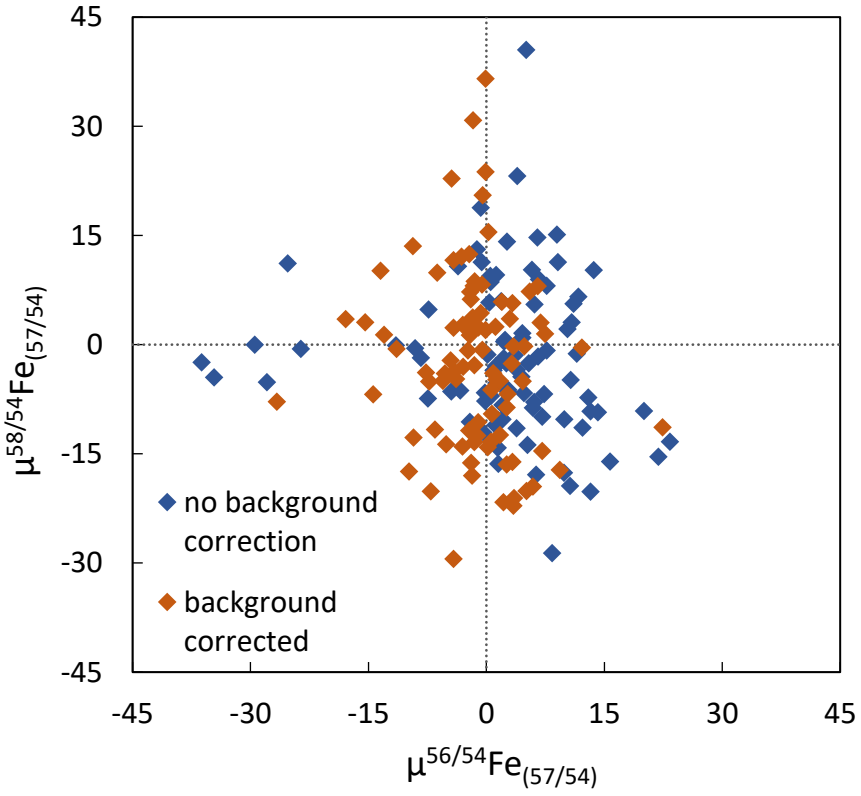

Figure 3.8. $\mu^{56/54}Fe_{(57/54)}$ vs. $\mu^{58/54}{}_{(57/54)}$ without and without background subtraction.

Additional measurements were performed to see if possible matrix material in the solutions affects the results and cause a difference between Fe standard and samples. Therefore, Murchison L1, L3, L4 and R was bracketed with L2 of Murchison, Cold Bokkeveld L2 was bracketed with L1 of Cold Bokkeveld and Indarch L2 and R were bracketed with L1 Indarch.

3. RESULTS

3.1. Iron fractions in the leachates and residues

The total amounts of Fe, measured in bulk samples, leachates and residues of six chondrites and one terrestrial sample are given in Table A.3 in µg. Also listed in Table A.3 and illustrated in Figure 3.9 is the distribution of Fe over the leach and residue fractions in % of bulk Fe.

Sequential acid leaching of five out of the six chondrite powder samples and one terrestrial powder sample produced two leachates (L1, L2) and one residue (R) per sample. For the sixth chondrite powder, Murchison, a larger amount of material was available, and a leaching procedure could be applied that produced four leachates L1, L2, L3, L4 and a residue R.

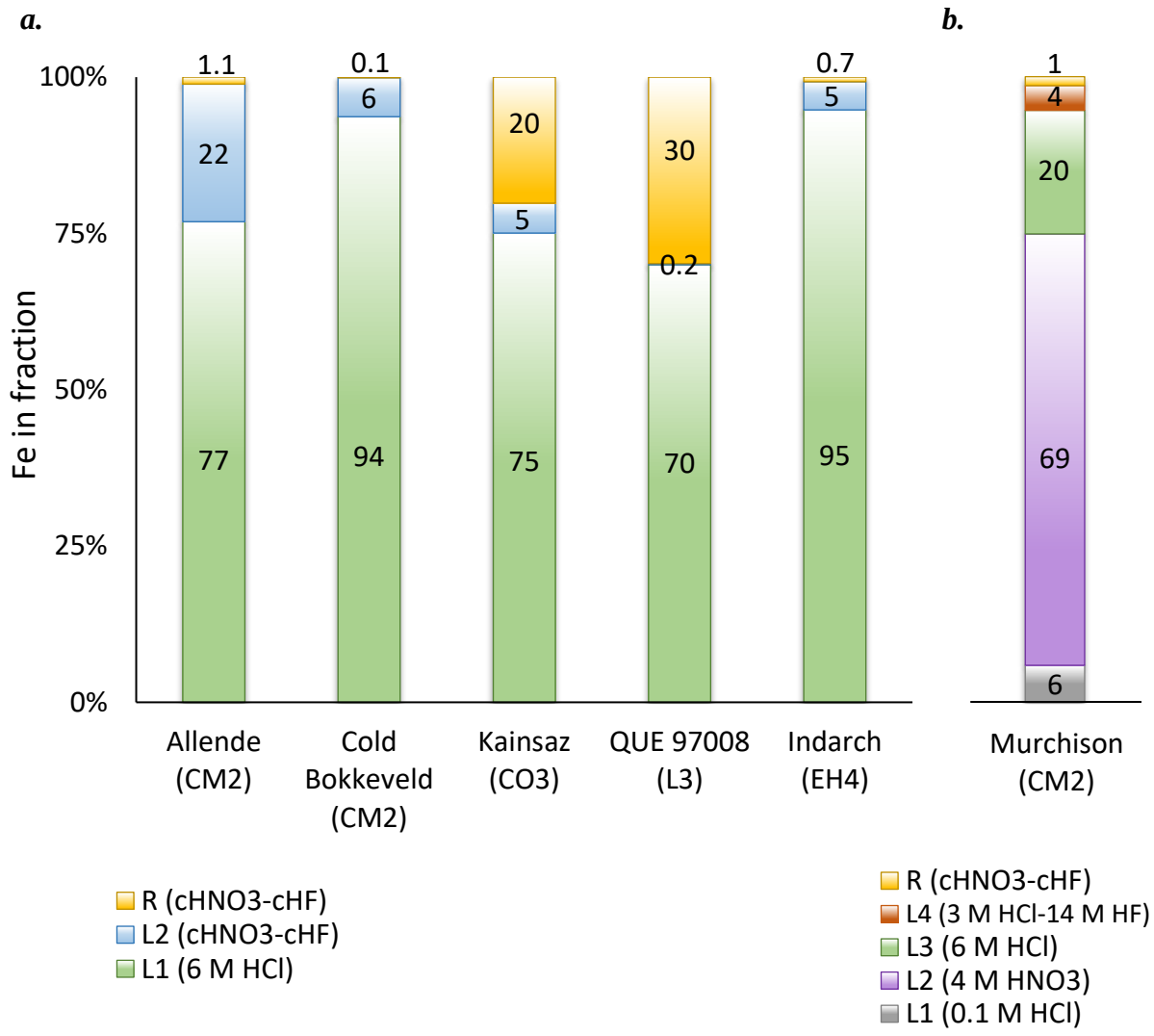

Figure 3.9. Iron distribution in % of bulk Fe in leachate and residue fractions (c in acid name: concentrated).

The relative Fe recovery in the first leachate L1 of all twice leached chondrites was between 70 and 96 % of the bulk Fe content (green sections in the columns of Figure 3.9a). The second leach step, L2 (blue sections in the columns of Figure 3.9a), had much more variable Fe fractions. In QUE a fraction of only 0.2 % Fe was recovered, in Cold Bokkeveld, Kainsaz and Indarch a fraction of 5-6 % was recovered, while for Allende, the recovery was the highest with a fraction of 22 % Fe. The Fe fractions in the residues R (yellow sections in columns of Figure 3.9a), were very small and ranged from 0.1 to 1.1 %, except for Kainsaz, with a fraction of 20 % and for QUE, with a high Fe fraction of 30 %.

In Murchison (Figure 3.9b), the iron fraction of the first leachate L1 (grey section) was 6 %. In the second leachate L2 (purple section) the major fraction (69 %) was released. Both steps, L1 and L2, applied weaker acids than the first leaching step applied to the other samples. In the third leaching step 6 M HCl was used, the same acid used as the first leaching step for the other samples. As a large fraction of Fe was already leached from Murchison before L3, leachate L3 (green section) contained only a fraction of 20 % of the bulk Fe. The fourth leachate L4 (red section) contained a fraction of 4 % of the bulk Fe and in the residue R (yellow section), only a fraction of 1 % Fe was found.

3.2. Stable Fe isotope compositions

Iron isotope ratios are shown in linearized δ'-notation in Figure 3.10 and Table A.5, both relative to the Fe in-house standard. Table A.6 gives the results in δ'-notation calculated relative to IRMM-014, for better comparison to literature data.

Data for $\delta'^{56/54}$Fe versus $\delta'^{58/54}$Fe of all sample leachates and residues, as well as bulk samples and standard material, plot on a single mass-dependent fractionation line with a slope of 1.9468±0.0015 (Figure 3.10). This slope is in excellent agreement with the theoretical value of 1.948. The size of the error bars equals the size of the symbols. As there are no visible deviations from the mass-dependent fractionation line, large mass-independent Fe isotope anomalies can be ruled out for ^{54}Fe, ^{56}Fe or ^{58}Fe. More detailed observations regarding nucleosynthetic anomalies are provided in the following section.

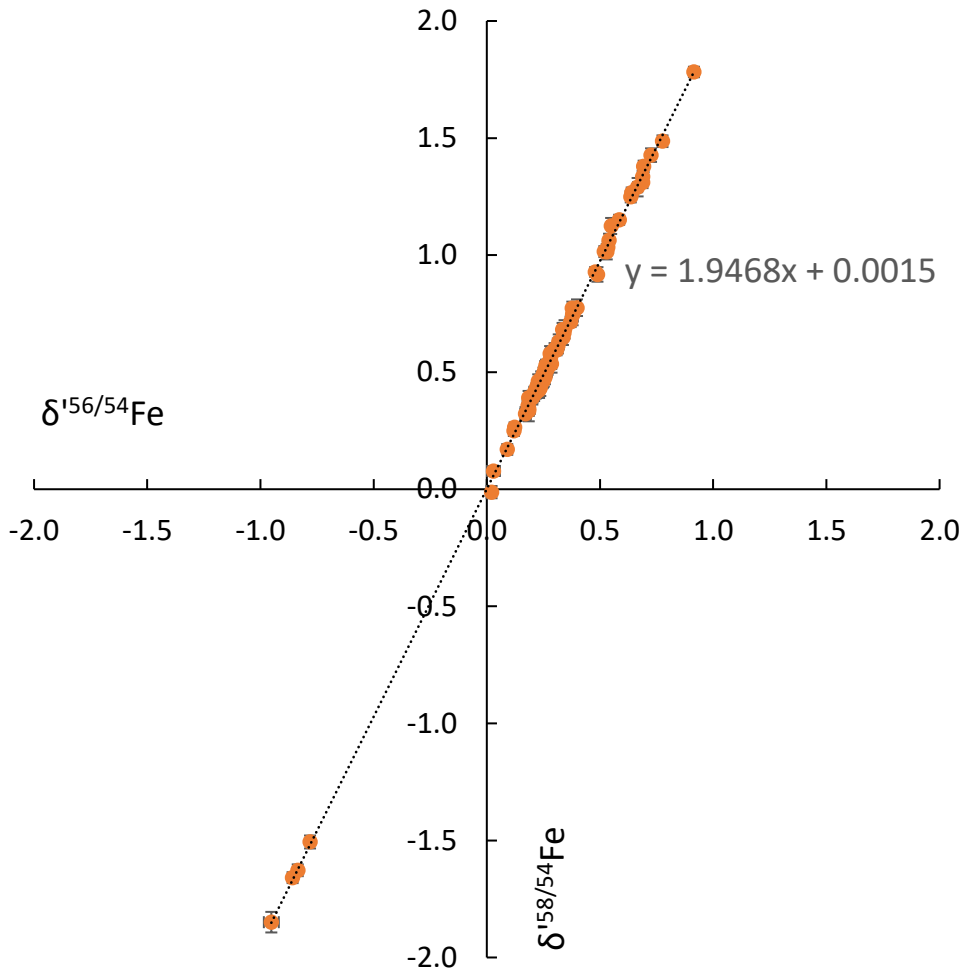

Figure 3.10. Three-isotope plot for meteorite data showing $\delta'^{56/54}Fe$ versus $\delta'^{58/54}Fe$ relative to IRMM Fe.

3.3. Mass-*in*dependent Fe isotope variations

Iron isotope data in the μ-notation for $^{56/54}Fe_{(57/54)}$ and $^{58/54}Fe_{(57/54)}$ are listed in Table 3.3 and shown in Figures 3.11 and 3.12 respectively. Each data point represents a single measurement, i.e., each leachate, residue and bulk sample has been repeatedly measured, typically three times per sample. The grey bar in Figures 3.11 and 3.12 represent the intermediate precision (2 s.d.) for $\mu^{56/54}Fe_{(57/54)}$ and $\mu^{58/54}Fe_{(57/54)}$, respectively. The error bars represent the combined 2 s.e. values as explained in section 2. Because we combined the 2 s.e. from sample and bracketing standard measurements, the error bars should overlap with $^{56/54}Fe_{(57/54)} = 0$ and $^{58/54}Fe_{(57/54)} = 0$, if no anomaly is present. Results of this study are compared to previous results by Wang et al. (2011), which are also plotted in Figures 3.11 and 3.12.

1.2.5. $\mu^{56/54}Fe_{(57/54)}$

The $\mu^{56/54}Fe_{(57/54)}$ of almost all chondrite and terrestrial leachates and residues, as well as bulk samples and the IRMM-014 standard agree within the combined 2 s.e. with that of the standard.

The IRMM-014 standards were measured during five different sessions and have a narrow range from -3 to +7 ppm, except one out of the 12 IRMM-014 analysis which displays a higher $\mu^{56/54}Fe_{(57/54)}$ of +22±12 ppm and hence displays an apparent anomaly. This serves as a note of caution, that single measurements may occasionally represent outliers.

Of the remaining 77 $\mu^{56/54}Fe_{(57/54)}$ values for chondrite and basalt leachates and residues and the Allende bulk sample measurements, only six clearly do not agree with the standard within error. Four analyses for Murchison leachates (2 x L1, L3, L4) display slightly lower $\mu^{56/54}Fe_{(57/54)}$ values, while two out of three analyses of the Indarch residue display slightly higher values. However, during the final measurement session the outlying Murchison leachates and Indarch residues were bracketed with Murchison L2 and Indarch L1, respectively and no anomalies outside 2 s.e. were observed. Consequently, the leaching experiments on do not reveal any nucleosynthetic anomalies for ^{54}Fe, ^{56}Fe and ^{57}Fe in the carbonaceous, enstatite or ordinary chondrite samples studied here.

1.2.6. $\mu^{58/54}Fe_{(57/54)}$

The $\mu^{58/54}Fe_{(57/54)}$ compositions of all samples show only slightly larger scatter in comparison to the $\mu^{56/54}Fe_{(57/54)}$ compositions with an intermediate precision of ±16 ppm, as obtained from 12 analysis of IRMM-014. The $\mu^{56/54}Fe_{(57/54)}$ for only six out of 89 data do not agree within the combined 2 s.e. with that of the standard. In the case of one LP8 residue, one Allende L2, one Murchison L3 and one QUE 97008 L1 analysis, at least two more measurements of the same samples agree within the combined 2 s.e. with the bracketing standards. For the Indarch residue, one out of three analyses relative to the in-house standard and one out of two Indarch residue measurements relative to Indarch L1 display slightly lower $\mu^{56/54}Fe_{(57/54)}$ values. We consider these “single measurement anomalies” as insignificant. However, the residue of Cold Bokkeveld displays the largest among all “anomalies” with $\mu^{58/54}Fe_{(57/54)}$ = 41±11 ppm. The residue contained only a fraction of 0.1% of the bulk Cold Bokkeveld Fe, which allowed only for a single measurement. The low Fe content of the Cold Bokkeveld residue makes this the most promising sample to reveal a nucleosynthetic anomaly, but also the sample that is most prone to matrix effects or other artifacts. Thus, we consider the “anomaly” observed for the

Cold Bokkeveld residue as a possible hint for a resolvable, but small ^{58}Fe isotope enrichment that requires further investigation.

Compared to the analytical precision of 150 ppm reported by Wang et al. (2011) for $^{58/54}Fe_{(57/54)}$, our intermediate precision of 16 ppm represents an almost 10-fold improvement. Nevertheless, no unambiguous ^{58}Fe isotope anomalies were found in the studied carbonaceous, enstatite or ordinary chondrite fractions.

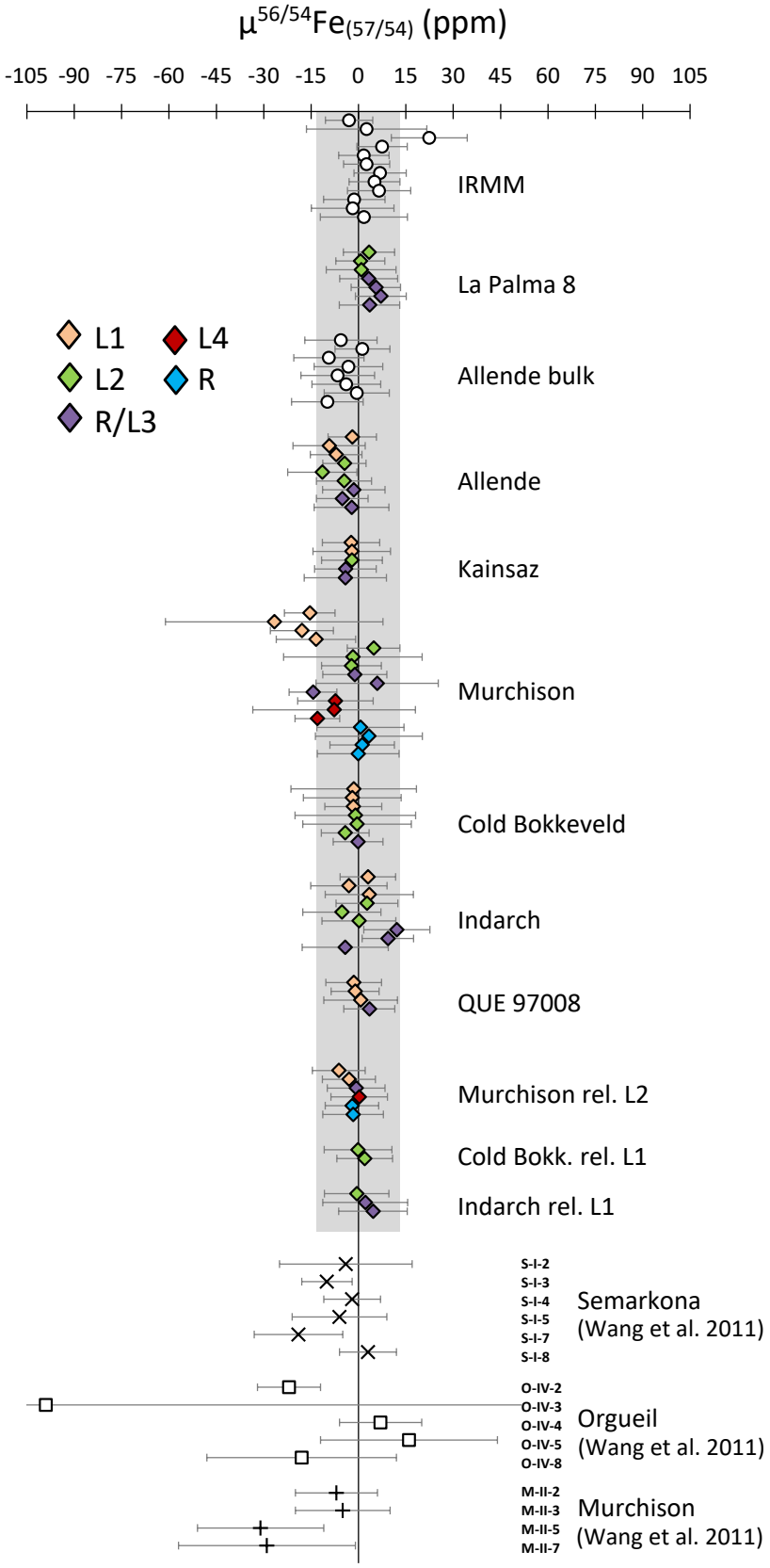

Figure 3.11. Fe isotope results as $\mu^{56/54}Fe_{(57/54)}$ of this study and from Wang et al. (2011). The grey bar represents the intermediate precision (2 s.d.) of 13 ppm for IRMM-0014 Fe over several months. The error bars refer to the combined 2 se uncertainty of samples and bracketing standards and should hence overlap with $\mu^{56/54}Fe_{(57/54)} = 0$ if no anomaly is present. The error bars for Wang et al. refer to 2 s.e. of their sample measurements.

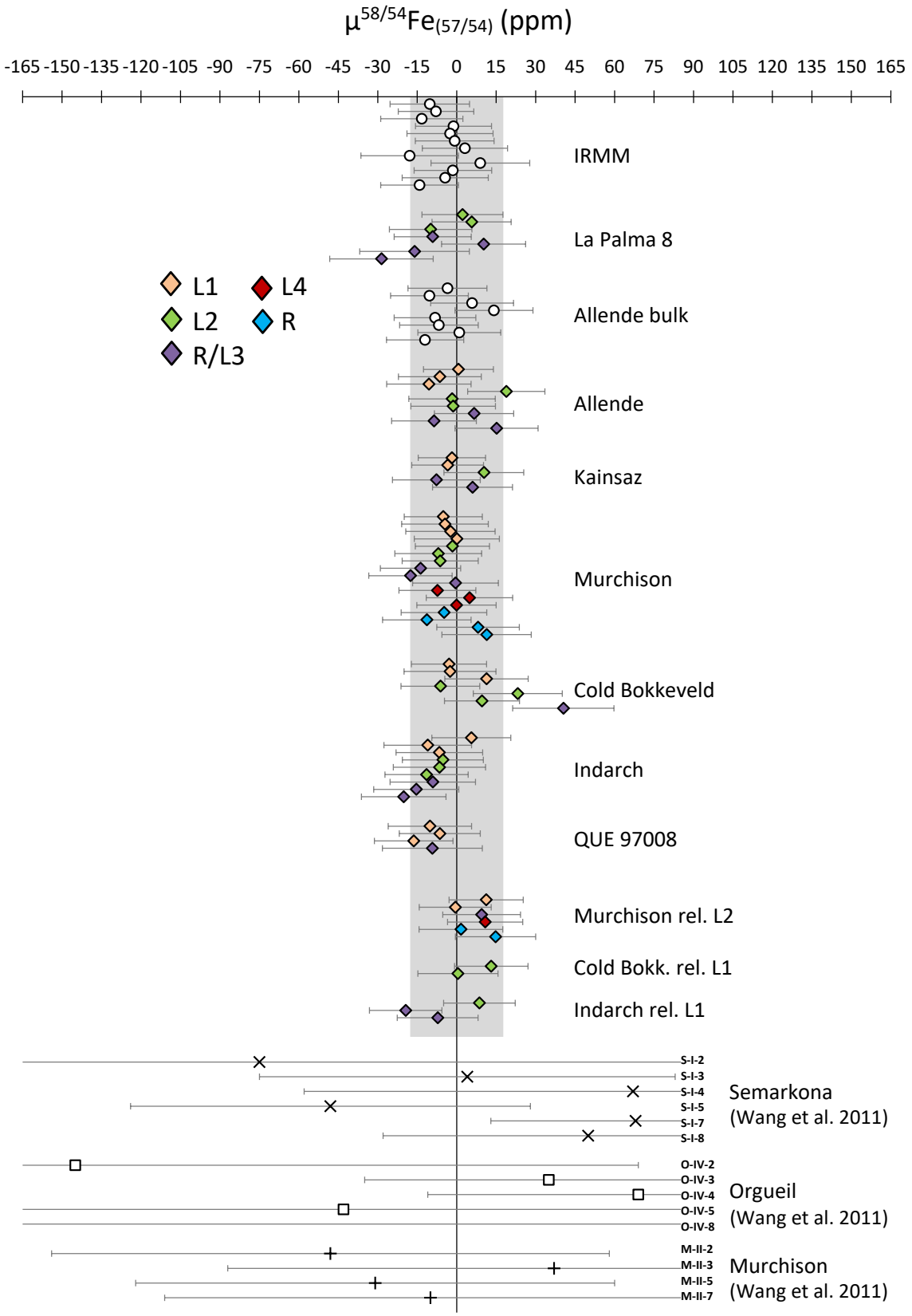

Figure 3.12. Fe isotope results as $\mu^{58/54}Fe_{(57/54)}$ of this study compared to results of Wang et al. (2011). The grey bar represents the intermediate precision (2 s.d.) of 16 ppm for IRMM-0014 Fe over several months. The error bars refer to the combined 2 s.e. uncertainty of samples and bracketing standards and should hence overlap with $\mu^{58/54}Fe_{(57/54)}$ = 0, if no anomaly is present. The error bars for Wang et al. refer to 2 s.e. of their sample measurements.

Table 3.3. Fe isotope results as $\mu^{56/54}Fe_{(57/54)}$ and $\mu^{58/54}Fe_{(57/54)}$.

sample	$\mu^{56/54}Fe_{(57/54)}$	2se	$\mu^{58/54}Fe_{(57/54)}$	2se
IRMM-014				
IRMM-3	-3	8	-10	15
IRMM-3	3	19	-8	14
IRMM-3	22	12	-13	16
IRMM-4	7	8	-1	14
IRMM-5	2	8	-3	16
IRMM-5	3	7	-1	15
IRMM-5	7	8	3	16
IRMM-6	5	8	-18	19
IRMM-6	7	10	9	19
IRMM-7	-1	10	-1	15
IRMM-7	-2	13	-4	16
IRMM-7	2	14	-14	15
LP8 basalt				
LP8 L2-4	3	8	2	15
LP8 L2-5	1	8	6	15
LP8 L2-7	1	11	-10	16
LP8 R-4	3	9	-9	15
LP8 R-5	6	8	10	16
LP8 R-6	7	8	-16	21
LP8 R-6	3	10	-29	20
Allende CV3 bulk				
ALL-2	-6	11	-4	15
ALL-2	1	9	-10	15
ALL-2	-9	11	6	16
ALL-2	-3	11	14	15
ALL-2	-7	12	-8	16
ALL-2	-4	11	-7	15
ALL-2	-1	10	1	16
ALL-2	-10	11	-12	15
Allende CV3				
ALL L1-5	-2	8	1	13
ALL L1-7	-9	11	-6	16
ALL L1-8	-7	8	-11	16
ALL L2-5	-4	7	19	15
ALL L2-7	-11	11	-2	16
ALL L2-8	-5	9	-1	16
ALL R-4	-2	10	7	15
ALL R-5	-5	8	-9	16
ALL R-8	-2	12	15	16

sample	$\mu^{56/54}Fe_{(57/54)}$	2se	$\mu^{58/54}Fe_{(57/54)}$	2se
Kainsaz CO3				
KAIN R-7	-4	13	6	15
KAIN L1-2	-2	9	-2	13
KAIN L1-7	-2	12	-3	14
KAIN L2-2	-2	10	10	15
KAIN R-2	-4	10	-8	17
Murchison CM2				
MUR L1-3	-15	8	-5	15
MUR L1-3	-27	34	-4	16
MUR L1-5	-18	10	-2	17
MUR L1-7	-13	13	0	16
MUR L2-3	5	8	-2	14
MUR L2-3	-2	22	-7	16
MUR L2-5	-2	9	-6	14
MUR L3-3	-1	10	-14	15
MUR L3-3	6	19	-18	16
MUR L3-5	-14	8	0	16
MUR L4-3	-7	12	-7	15
MUR L4-3	-8	26	5	16
MUR L4-5	-13	7	0	15
MUR R-3	1	14	-5	16
MUR R-3	3	17	-11	17
MUR R-5	1	10	8	16
MUR R-7	0	13	11	17
Cold Bokkeveld CM2				
CO BO L1-3	-2	20	-3	14
CO BO L1-3	-2	15	-3	17
CO BO L1-5	-2	9	11	16
CO BO L2-3	-1	19	-6	15
CO BO L2-3	0	17	23	17
CO BO L2-5	-4	8	10	14
CO BO R-6	0	8	41	19
Indarch EH4				
IND L1-4	3	9	6	15
IND L1-7	-3	12	-11	17
IND L1-8	3	14	-7	16
IND L2-4	3	10	-5	15
IND L2-7	-5	12	-7	18
IND L2-8	0	12	-11	16
IND R-4	12	10	-9	16
IND R-5	9	8	-15	16
IND R-7	-4	14	-20	16

sample	$\mu^{56/54}Fe_{(57/54)}$	2se	$\mu^{58/54}Fe_{(57/54)}$	2se
QUE 97008 L3.05				
QUE L1-4	-2	9	-10	16
QUE L1-5	-1	8	-6	15
QUE L1-8	1	12	-16	15
QUE R-6	3	8	-9	19
Murchison CM2[a]				
MUR L1-9	-6	8	11	14
MUR L1-9	-3	8	-1	14
MUR L3-9	-1	9	9	15
MUR L4-9	0	9	11	14
MUR R-9	-2	8	2	16
MUR R-9	-2	10	15	15
Cold Bokkeveld CM2[b]				
CO BO L2-9	0	11	13	14
CO BO L2-9	2	9	0	15
Indarch EH4[c]				
IND L2-9	-1	10	9	14
IND R-9	2	13	-19	14
IND R-9	5	11	-7	15

All samples measured using Fe in-house standard for sample-standard bracketing, except: [a] bracketed using Murchison L2; [b] bracketed using Cold Bokkeveld L1; [c] bracketed using Indarch L1.

4. DISCUSSION

4.1. Mass-dependent Fe isotope fractionation in leachates and residues

Leachates and residues of all analyzed chondrites, with the exception of Indarch, display systematic Fe isotope fractionations between leach steps. First leach steps show light Fe isotope compositions whereas residues show heavy Fe isotope compositions. The largest range of $\delta^{56/54}$Fe shows Murchison with an average variation between Mur L1 and Mur R of 1.49 ‰. These variations could result from the leaching process, but more likely reflect the different Fe isotope compositions of the different phases dissolved in each step. Easy soluble phases like sulfides tend to be enriched in light Fe isotopes whereas refractory phases like spinel contain heavy Fe isotopes (Steinhoefel et al., 2009). Former phases are dissolved during the first leach step while the latter refractory mineral phases remain in the sample until the residue gets dissolved completely.

The regression yields a slope of 1.3202±0.0056 at the 95% confidence level. In the following, the observed slope is compared to slopes expected, based on experiments and theory. Slopes given in brackets were calculated for FeO as the molecular masses in motion, which constitutes a minor gas species during evaporation/condensation of Fe (Fedkin et al., 2006). Within uncertainty, the observed slope is consistent with slopes predicted by the Rayleigh law of Zhang et al. (2014), which described the experimental evaporation of Ca and TiO_2 and which predicts a slope of 1.3157 (1.3195). The observed slope is also in agreement with the slope of 1.3214 (1.3240) expected for kinetic isotope fractionation, but not with the slope expected for equilibrium isotope fractionation of 1.3272. This evaluation appears to suggest that most of the Fe isotope fractionation revealed in the studied meteorite samples and in particular in the leachates and residues is consistent with kinetic isotope fractionation related to evaporation and condensation, but not with equilibrium isotope partitioning between phases.

4.2. Mass-independent (nucleosynthetic) Fe isotope compositions: Homogeneous iron vs. dichotomy of Fe-peak element isotopes

All iron isotope compositions in bulk chondrites and in chondrite leachates and residues, shown as $\mu^{56/54}Fe_{(57/54)}$ and $\mu^{58/54}Fe_{(57/54)}$ agree with that of the Earth (Figure 3.11 and Figure 3.12, Table 3.3). Despite high precision of the data, clear nucleosynthetic isotope anomalies are

neither resolved within chondrite samples nor within the planetary scale. In contrast to the other Fe-peak elements, Cr and Ni as well as Ca and Ti, no excess or deficits of neutron-rich nuclei were found in bulk or leached samples. The distribution of the neutron-rich nuclei ^{50}Ti, ^{54}Cr and ^{64}Ni in bulk samples of carbonaceous and non-carbonaceous group solar system materials show a dichotomy, which means positive anomalies are found in carbonaceous chondrites and related materials and negative or no anomalies, respectively, are found in non-carbonaceous materials (Warren, 2011; Dauphas and Schauble, 2016, Figure 3.13). There is no intermediate composition of ε^{50}Ti, ε^{54}Cr and ε^{54}Ni but a clear separation between the two different trends. The fact that Fe does not follow this dichotomic pattern leads to the assumption that Fe must have taken a different path from its nucleosynthesis towards the distribution in our solar system than its neighboring elements of similar mass.

Whether type II supernovae nor rare neutron-rich massive type Ia supernovae are able to produce neutron-rich Fe-peak element isotopes without creating an excess in neutron-rich Fe isotopes (Wang et al., 2011; Kodolányi et al., 2018). It is possible though, that the synthesized material underwent element fractionation before or during mixing and grain condensation (Kodolányi et al., 2018).

Restraints in nucleosynthesis and solar system formation allow for two main theories in order to explain the origin of isotope anomalies for Ti, Cr and Ni, but not for Fe: I. The redistribution of corresponding carrier phases during solar system formation or II. the injection and heterogeneous distribution of anomalous presolar dust into the early solar system or its parental molecular cloud whereby Fe isotope composition became homogenized at the grain and planetary scale but Ti, Cr and Ni isotope heterogeneities survived.

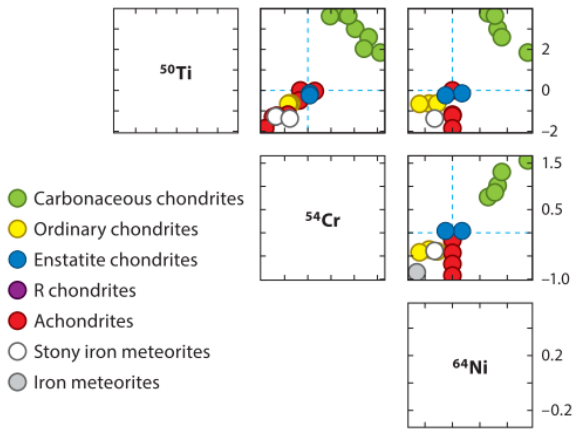

Figure 3.13. Dichotomy of ε^{48}Cr, ε^{50}Ti and ε^{54}Cr anomalies in bulk planetary materials with composition of silicate Earth at the intersection of the blue dashed lines (Dauphas and Schauble, 2016)

4.3. Theory I: Redistribution of carrier phases

When elements condense into different types of dust in supernova shells, calculations show that Ti and Cr condense at higher temperatures than Fe and form refractory phases (e.g. TiC, Cr bearing spinel (Davis, 2011)), while Fe condenses as metallic Fe, FeS or FeO at lower temperatures, lower pressure and in zones with zero H abundance, respectively (Lattimer and Grossman, 1978). In the outer shells of Si- and Ni-burning zones in supernovae, metallic Fe can be the initial condensate, accompanied by Ni and Ti, forming Fe-Ni alloys, metallic Ti, NiTi and FeTi (Fedkin et al., 2010). The condensation temperature of Fe is independent of C/O ratios in the different shells in contrast to most other element condensation temperatures (Lattimer and Grossman, 1978; Fedkin et al., 2010). If Fe is mainly present in less refractory phases, a decoupling from more refractory, Fe-peak element bearing phases would be possible through evaporation during high-temperature events. Thermal processing of presolar components could destroy fragile carrier phases to varying degrees (Huss, 2004; Trinquier et al., 2009).

Correlations of mass-independent anomalies of isotopes with different nucleosynthetic origins suggest that the presolar dust inherited from the molecular cloud was well mixed when the first solar system solids formed (Trinquier et al., 2009). During the formation of the solar system, initially homogeneously distributed refractory carrier phases of anomalous Cr, Ti and Ni may have been sorted after density or grain-size due to turbulences and differences in velocity and aerodynamic (Kuebler et al., 1999; Cuzzi and Zahnle, 2004; Cuzzi and Alexander, 2006; Dauphas and Schauble, 2016). This may have caused the observed dichotomy in the solar system, while gaseous Fe mixed and homogenized within the gas phase, leaving no detectable nucleosynthetic Fe isotope anomaly in solar system materials except in rare presolar grains (e.g. Tripa et al., 2002; Marhas et al., 2008)) with minor significance for the Fe budget. As a consequence, parent bodies formed in different areas of the solar nebula reflect nucleosynthetic Ti, Cr and Ni isotope anomalies due to the redistribution of refractory grains.

4.4. Theory II: Injection and heterogeneous distribution of anomalous presolar dust

In the absence of size sorting and redistribution of carrier phases, an initially homogeneous molecular cloud or protosolar disk would need an external source for nucleosynthetic anomalies. An injection of material with anomalous Fe-peak element isotope composition into the solar nebula before the formation of lager solids would locally alter the isotopic composition

of solar material. An enrichment of neutron-rich isotopes in the outer solar nebula, detectable in Fe-peak element isotopes of carbonaceous chondrites, may have caused the isotopic heterogeneity and the dichotomy between the inner regions and outer regions. The dichotomy could be persevered for Fe-peak element isotopes if injected Ti, Cr and Ni are carried by refractory phases while injected Fe isotopes are embedded in less stable phases that get destroyed more easily. Heating events during the solar system formation could cause evaporation of Fe bearing material and enable the gaseous Fe to be mixed and homogeneously distributed via turbulences in the entire solar nebula. Only a very small amount of anomalous Fe in presolar grains, mainly SiC (Ong and Floss, 2015), survived the high-temperature events and provide detectable Fe isotope anomalies in single grains. Due to the mass budget of Fe in the solar system, detection of remaining anomalous presolar Fe isotopes in bulk rock samples or in leaching experiments would not be possible.

If injected material, that caused anomalies in Fe-peak elements, did not induce anomalous Fe into the solar system at all, the added material must have undergone decoupling processes that separated Fe during the transport through the interstellar medium before injection. Possibly, a high-temperature event occurred already during the transport of matter in the ISM to destroy Fe carrier phases before the material got injected into the solar nebula.

5. CONCLUSION

This chapter presents high-precision Fe isotope data for a bulk rock carbonaceous chondrite sample (Allende CV3), a bulk rock terrestrial basalt sample and sequentially leached samples of carbonaceous, ordinary and enstatite chondrites. Stable Fe isotope data shown as $\delta'^{56/54}Fe$ and $\delta'^{58/54}Fe$, as well as nucleosynthetic Fe compositions shown as $\mu^{56/54}Fe_{(57/54)}$ and $\mu^{58/54}Fe_{(57/54)}$ of analyzed bulk samples, leachates and residues are documented.

Differences in stable Fe isotope composition span up to 1.5 ‰ in $^{56}Fe/^{54}Fe$ typically with the leachates enriched in the light and residues enriched in the heavy isotopes. The stable isotope composition most likely reflects that of dissolved phases in the different leach steps. The observed slopes between different Fe isotope ratios are in good agreement with predictions for kinetic isotope fractionation.

In bulk rock samples and chondrite leachates and residues, no resolvable nucleosynthetic Fe isotope anomaly was found. This raises the question if and how Fe was decoupled from Fe-peak elements that show nucleosynthetic isotope anomalies at the planetary scale and for chondrite leachates and residues.

Two theories are suggested to explain the homogeneous distribution of Fe isotopes in chondrites and on a planetary scale accompanied by resolvable nucleosynthetic Fe-peak element isotope anomalies:

Theory I suggests a redistribution of refractory carrier phases that bear anomalous Fe-peak elements within an initially homogeneous solar nebula. This redistribution could have taken place via grain-size or density sorting, driven by turbulences, velocity and aerodynamics.

Theory II suggests an injection and heterogeneous distribution of anomalous presolar dust before the accumulation of solar material into larger bodies. Anomalous Fe of the injected material could have been vaporized due to its less refractory carrier phases and homogeneous distributed in the solar nebula whereas anomalous Fe-peak elements and their refractory carrier phases became enriched in the outer solar system.

At which exact point between injection into the ISM and solar system formation, iron was separated from its “neighbor” elements to become homogeneously distributed in the solar system on a bulk rock and planetary scale is still a question that needs to be answered.

References

Abouchami W., Galer S. J. G., Horner T. J., Rehkämper M., Wombacher F., Xue Z., Lambelet M., Gault-Ringold M., Stirling C. H., Schönbächler M., Shiel A. E., Weis D. and Holdship P. F. (2013) A Common Reference Material for Cadmium Isotope Studies - NIST SRM 3108. *Geostand. Geoanalytical Res.* **37**, 5–17.

Alexander C. M. O. (2001) The Early Evolution of the Inner Solar System: A Meteoritic Perspective. *Science (80-.).* **293**, 64–68.

Alexander C. M. O., Grossman J. N., Ebel D. S. and Ciesla F. J. (2008) The formation conditions of chondrules and chondrites. *Science (80-.).* **320**, 1617–1619.

Alexander C. M. O., Grossman J. N., Wang J., Zanda B., Bourot-Denise M. and Hewins R. H. (2000) The lack of potassium-isotopic fractionation in Bishunpur chondrules. *Meteorit. Planet. Sci.* **35**, 859–868.

Alexander C. M. O. and Hewins R. H. (2004) Mass fractionation of Fe and Ni isotopes in metal in Hammadah al Hamrah 237. *Meteorit. Planet. Sci.* **39**.

Amari S., Nittler L. R., Zinner E., Gallino R., Lugaro M. and Lewis R. S. (2001) Presolar SiC Grains of Type Y: Origin from Low-Metallicity Asymptotic Giant Branch Stars. *Astrophys. J.* **546**, 248–266.

Amelin Y., Kaltenbach A., Iizuka T., Stirling C. H., Ireland T. R., Petaev M. and Jacobsen S. B. (2010) U-Pb chronology of the Solar System's oldest solids with variable 238U/235U. *Earth Planet. Sci. Lett.* **300**, 343–350.

Australia Telescope National Facility Post-Main Sequence Stars. *Outreach/Astrophysics Sr. Phys.* Available at: https://www.atnf.csiro.au/outreach//education/senior/astrophysics/stellarevolution_postmain.html.

Baker R. G. A., Rehkämper M., Hinkley T. K., Nielsen S. G. and Toutain J. P. (2009) Investigation of thallium fluxes from subaerial volcanism—Implications for the present and past mass balance of thallium in the oceans. *Geochim. Cosmochim. Acta* **73**, 6340–6359.

Beckett J. R., Live D., Tsay F. D., Grossman L. and Stolper E. (1988) Ti3+in meteoritic and synthetic hibonite. *Geochim. Cosmochim. Acta* **52**, 1479–1495.

Behrens R. G. and Mason C. F. V (1981) A mass spectrometric investigation of the vaporization thermodynamics and vapor composition of cadmium oxide. *J. Less Common Met.* **77**, 169–184.

Birck J. L. (2004) An Overview of Isotopic Anomalies in Extraterrestrial Materials and Their Nucleosynthetic Heritage. *Rev. Mineral. Geochemistry* **55**, 25–64.

Birck J. L. and Allègre C. J. (1984) Chromium Isotopic Anomalies in Allende Refractory Inclusions. *Geophys. Res. Lett.* **11**, 943–946.

Birck J. L. and Lugmair G. W. (1988) Nickel and chromium isotopes in Allende inclusions. *Earth Planet. Sci. Lett.* **90**, 131–143.

Birck J. L., Rotaru M. and Allègre C. J. (1999) 53Mn-53Cr evolution of the early solar system. *Geochim. Cosmochim. Acta* **63**, 4111–4117.

Bizzarro M., Ulfbeck D., Trinquier A., Thrane K., Connelly J. N. and Meyer B. S. (2007) Evidence for a Late Supernova Injection of 60Fe into the Protoplanetary Disk. *Science (80-.).* **316**, 1178–1181.

Boss A. P. and Ciesla F. J. (2013) 2.3 - The Solar Nebula. In *Treatise on Geochemistry* Elsevier Ltd. pp. 37–53.

Bourdon B., Fitoussi C. and Wang X. (2017) Isotope fractionation during partial condensation. In *Goldschmidt 2017*

Bouvier A. and Wadhwa M. (2010) The age of the Solar System redefined by the oldest Pb-b age of a meteoritic inclusion. *Nat. Geosci.* **3**, 637–641.

Braukmüller N., Wombacher F., Hezel D. C., Escoube R. and Münker C. (2018) The chemical composition of carbonaceous chondrites: Implications for volatile element depletion, complementarity and alteration. *Geochim. Cosmochim. Acta* **239**, 17–48.

Busso M., Roberto G. and Wasserburg G. J. (1999) Nucleosynthesis in Asymptotic Giant Branch Stars: Relevance for Galactic Enrichment and Solar System Formation. *Annu. Rev. Astron. Astrophys.* **37**, 239–309.

Calvet N., Hartmann L. and Strom S. E. (1999) Evolution of Disk Accretion. , 1–28.

Canup R. M., Visscher C., Salmon J. and Fegley Jr B. (2015) Lunar volatile depletion due to incomplete accretion within an impact-generated disk. *Nat. Geosci.* **8**, 918–921.

Chambers J. E. (2013) 2.4 - Planet Formation. In *Treatise on Geochemistry* Elsevier Ltd. pp. 55–72.

Chen J. H. and Papanastassiou D. A. (2014) Endemic 64Ni Effects in Allende Ca-Al-rich Inclusions. In *Lunar and Planetary Science Conference* p. Abstract #2327.

Clayton D. D. (2003) *Handbook of Isotopes in the Cosmos: Hydrogen to Gallium.*, Cambridge University Press, Cambridge, U.K.

Clayton D. D. and Nittler L. R. (2004) Astrophysics With Presolar Stardust. *Annu. Rev. Astron. Astrophys.* **42**, 39–78.

Cloquet C., Carignan J., Libourel G., Sterckeman T. and Perdrix E. (2006) Tracing source pollution in soils using cadmium and lead isotopes. *Environ. Sci. Technol.* **40**, 2525–2530.

Craig H. and Gordon L. I. (1965) Deuterium and oxygen 18 variations in the ocean and the marine atmosphere. In *Symposium on Marine Geochemistry* University of Rhode Island Publication. pp. 277–374.

Cuzzi J. N. and Alexander C. M. O. (2006) Chondrule formation in particle-rich nebular regions at least hundreds of kilometres across. *Nature* **441**, 483–485.

Cuzzi J. N. and Zahnle K. J. (2004) Material Enhancement in Protoplanetary Nebulae by Particle Drift through Evaporation Fronts. *Astrophys. J.* **614**, 490–496.

Dauphas N., Janney P. E., Mendybaev R. A., Wadhwa M., Richter F. M., Davis A. M., van Zuilen M., Hines R. and Foley C. N. (2004) Chromatographic separation and multicollection-ICPMS analysis of iron. Investigating mass-dependent and -independent isotope effects. *Anal. Chem.* **76**, 5855–63.

Dauphas N. and Rouxel O. (2006) Mass spectrometry and natural variations of iron isotopes. *Mass Spectrom. Rev.* **25**, 515–520.

Dauphas N. and Schauble E. A. (2016) Mass Fractionation Laws, Mass-Independent Effects, and Isotopic Anomalies. *Annu. Rev. Earth Planet. Sci.* **44**, 709–783.

Davis A. M. (2011) Stardust in meteorites. *Proc. Natl. Acad. Sci.* **108**, 19142–19146.

Davis A. M., Hashimoto A., Clayton R. N. and Mayeda T. K. (1990) Isotope mass fractionation during evaporation of Mg2SiO4. *Nature* **347**, 655–658.

Davis A. M. and Richter F. M. (2013) 1.10 - Condensation and Evaporation of Solar System Materials. In *Treatise on Geochemistry* Elsevier Ltd. pp. 335–360.

Dingwell D. B., O'Neill H. S. C., Ertel W. and Spettel B. (1994) The solubility and oxidation state of nickel in silicate melt at low oxygen fugacities: Results using a mechanically assisted equilibration technique. *Geochim. Cosmochim. Acta* **58**, 1967–1974.

Ebel D. S. and Grossman L. (2000) Condensation in dust-enriched systems. *Geochim. Cosmochim. Acta* **64**, 339.

Eiler J. M., Bergquist B., Bourg I., Cartigny P., Farquhar J., Gagnon A., Guo W., Halevy I., Hofmann A., Larson T. E., Levin N., Schauble E. A. and Stolper D. (2014) Frontiers of stable isotope geoscience. *Chem. Geol.* **372**, 119–143.

Elfers B. M., Sprung P., Pfeifer M., Wombacher F., Peters S. T. and Münker C. (2018) Variable distribution of s-process Hf and W isotope carriers in chondritic meteorites – Evidence from174Hf and180W. *Geochim. Cosmochim. Acta* **239**, 346–362.

Ertel-Ingrisch W. and Dingwell D. (2010a) Temperature- and fO2-Dependence of the Volatility and Condensation Behaviour of Volatile Elements: Experimental Results. In *AGU Fall Meeting* San Francisco. p. Abstract 966650.

Ertel-Ingrisch W. and Dingwell D. B. (2010b) The Volatility and condensation behaviour of elements in dependence of T and fO2 : a novel experimental approach. *EGU Gen. Assem. Conf. Abstr.* **12**, 11289.

Esat T. M. (1988) Physicochemical isotope anomalies*. *Geochim. Cosmochim. Acta* **52**, 1409–1424.

Esat T. M., Spear R. H. and Taylor S. R. (1986) Isotope anomalies induced in laboratory distillation. *Nature* **319**, 576–578.

Esat T. M. and Taylor S. R. (1999) Isotope fractionation in the solar system. *Int. Geol. Rev.* **41**, 31–46.

Fedkin A. V, Grossman L. and Ghiorso M. S. (2006) Vapor pressures and evaporation coefficients for melts of ferromagnesian chondrule-like compositions. *Geochim. Cosmochim. Acta* **70**, 206–223.

Fedkin A. V, Meyer B. S. and Grossman L. (2010) Condensation and mixing in supernova ejecta. *Geochim. Cosmochim. Acta* **74**, 3642–3658.

Floss C., Stadermann F. J. and Bose M. (2008) Circumstellar Fe Oxide from the Acfer 094 Carbonaceous Chondrite. *Astrophys. J.* **672**, 1266–1271.

Friedrich J. M., Weisberg M. K., Ebel D. S., Biltz A. E., Corbett B. M., Iotzov I. V, Khan W. S. and Wolman M. D. (2015) Chondrule size and related physical properties: A compilation and evaluation of current data across all meteorite groups. *Chemie der Erde - Geochemistry* **75**, 419–443.

Friend P., Hezel D. C., Barrat J.-A., Zipfel J., Palme H. and Metzler K. (2018) Composition, petrology, and chondrule-matrix complementarity of the recently discovered Jbilet Winselwan CM2 chondrite. *Meteorit. Planet. Sci.* **2491**, 2470–2491.

Galy A., Young E. D., Ash R. D. and O'Nions R. K. (2000) The formation of chondrules at high gas pressures in the solar nebula. *Science (80-.).* **290**, 1751–1753.

Gammie C. F. (1996) Layered accretion in T Tauri disks. *Astrophys. J.* **457**, 355–362.

Glemser O. and Stöcker U. (1963) Das Dissoziationsgleichgewicht CdO(s)=Cd(g) + 0,5O2(g). *Berichte der Bunsengesellschaft für Phys. Chemie* **67**, 505–509.

Goodwin S. (2013) Star formation. In *Planets, Stars and Stellar Systems* pp. 243–277.

Greshake A., Krot A. N., Meibom A., Weisberg M. K., Zolensky M. E. and Keil K. (2002) Heavily-hydrated lithic clasts in CH chondrites and the related, metal-rich chondrites Queen Alexandra Range 94411 and Hammadah al Hamra 237. *Meteorit. Planet. Sci.* **37**, 281–293.

Grossman L. (1972) Condensation in the primitive solar nebula. *Geochim. Cosmochim. Acta* **36**, 597–619.

Hawley J. F., Gammie C. F. and Balbus S. A. (1995) Local three-dimensional magnetohydrodynamic simulations of accretion disks. *Astrophys. J.* **440**, 742–763.

Heger A., Fröhlich C. and Truran J. W. (2013) 2.1 - Origin of the Elements. In *Treatise on Geochemistry* pp. 1–14.

Herzog G. F., Alexander C. M. O., Berger E. L., Delaney J. S. and Glass B. P. (2008) Potassium isotope abundances in Australasian tektites and microtektites. *Meteorit. Planet. Sci. Arch.* **43**, 1641–1657.

Hewins R. H., Connolly H. C. and Libourel G. (2005) Experimental Constraints on Chondrule Formation. *Chondrites Protoplanetary Disk* **341**, 286.

Hewins R. H., Jones R. H. and Scott E. R. D. (1996) *Chondrules and the protoplanetary disk.*, Cambridge University Press.

Hezel D. C. (2014) A big message from small grains: Constraints for solar nebula conditions from primitive meteorites. Habilitation, Universität zu Köln.

Hezel D. C. (2019) Bindungsenergien der Isotope. *Online-class Teach. Mater.*

Hezel D. C., Needham A. W., Armytage R., Georg B., Abel R. L., Kurahashi E., Coles B. J., Rehkämper M. and Russell S. S. (2010) A nebula setting as the origin for bulk chondrule Fe isotope variations in CV chondrites. *Earth Planet. Sci. Lett.* **296**, 423–433.

Hezel D. C., Russell S. S., Ross A. J. and Kearsley A. T. (2008) Modal abundances of CAIs: Implications for bulk chondrite element abundances and fractionations. *Meteorit. Planet. Sci.* **43**, 1879–1894.

Hirth J. P. and Pound G. M. (1960) Coefficients of evaporation and condensation. *J. Phys. Chem.* **64**, 619–626.

Hoppe P., Leitner J. and Kodolányi J. (2017) The stardust abundance in the local interstellar cloud at the birth of the Solar System. *Nat. Astron.* **1**, 617–620.

Hoppe P. and Ott U. (1997) Mainstream silicon carbide grains from meteorites. In *Astrophysical implications of the laboratory study of presolar materials* ASCE. pp. 27–58.

Hoppe P., Strebel R., Eberhardt P., Amari S. and Lewis R. S. (2000) Isotopic properties of silicon carbide X grains from the Murchison meteorite in the size range 0.5-1.5 μm. *Meteorit. Planet. Sci.* **35**, 1157–1176.

Hulston J. R. and Thode H. G. (1965) Variations in the S33, S34 and S36 Contents of Meteorites and Their Relation to Chemical and Nuclear Effects. *J. Geophys. Res.* **70**, 3475–3484.

Humayun M. and Cassen P. (2000) Processes Determining the Volatile Abundances of the Meteorites and Terrestrial Planets. *Orig. earth moon*, 3–23.

Humayun M. and Clayton R. N. (1995) Potassium isotope cosmochemistry: Genetic implications of volatile element depletion. *Geochim. Cosmochim. Acta* **59**, 2131–2148.

Huss G. R. (2004) Implications of isotopic anomalies and presolar grains for the formation of the solar system. *Antart. Meteor. Res.* **17**, 132–152.

International Astronomical Union (2012) RESOLUTION B2 on the re-definition of the astronomical unit of lenght. In *The XXVIII General Assembly of International Astronomical Union*

Iwamoto K., Brachwitz F., Nomoto K., Kishimoto N., Umeda H., Hix W. R. and Thielemann F. (1999) Nucleosynthesis in Chandrasekhar Mass Models for Type Ia Supernovae and Constraints on Progenitor Systems and Burning-Front Propagation. *Astrophys. J. Suppl. Ser.* **125**, 439–462.

Jeans J. H. (1902) I. The Stability of a Spherical Nebula. *Philos. Trans.* **199**, 1–53.

Jones R. H., Lee T., Connolly, Junior H. C., Love S. G. and Shang H. (2000) Formation of Chondrules and CAIs: Theory vs. observation. *Protostars Planets IV*, 927–962.

Kato C. and Moynier F. (2017) Gallium isotopic evidence for the fate of moderately volatile elements in planetary bodies and refractory inclusions. *Earth Planet. Sci. Lett.* **479**, 330–339.

Kehm K., Hauri E. H., Alexander C. M. O. and Carlson R. W. (2003) High precision iron isotope measurements of meteoritic material by cold plasma ICP-MS. *Geochim. Cosmochim. Acta* **67**, 2879–2891.

Knudsen M. (1911) Die molekulare Wärmeleitung der Gase und der Akkommodationskoeffizient. *Ann. Phys.* **339**, 593–656.

Kodolányi J., Stephan T., Trappitsch R., Hoppe P., Pignatari M., Davis A. M. and Pellin M. J. (2018) Iron and nickel isotope compositions of presolar silicon carbide grains from supernovae. *Geochim. Cosmochim. Acta* **221**, 127–144.

Kööp L., Stephan T., Davis A. M., Trappitsch R., Pellin M. J. and Heck P. R. (2016) Iron and Nickel Isotope Measurements in Hibonite using CHILI. In *Annual Meeting of the Meteoritical Society* p. Abstract #6456.

Kuebler K. E., McSween H. Y., Carlson W. D. and Hirsch D. (1999) Sizes and Masses of Chondrules and Metal-Troilite Grains in Ordinary Chondrites: Possible Implications for Nebular Sorting. *Icarus* **141**, 96–106.

Langmuir I. (1913) Der Dampfdruck metallischen Wolframs (The Vapor Pressure of Metallic Tungsten). *Phys. Z.* **14**, 1273–1280.

Lattanzio J. C. (2002) AGB stars: Summary and warning. *New Astron. Rev.* **46**, 469–474.

Lattanzio J. C. and Lugaro M. (2005) What we do and do not know about the s-process in AGB stars. *Nucl. Phys. A* **758**, 477–484.

Lattimer J. M. and Grossman L. (1978) Chemical Condensation sequences in Supernova Ejecta. *Moon Planets* **19**, 169–184.

Leya I., Schönbächler M., Krähenbühl U. and Halliday A. N. (2009) New Titanium Isotope Data for Allende and Efremovka CAIs. *Astrophys. J.* **702**, 1118–1126.

Leya I., Schönbächler M., Wiechert U., Krähenbühl U. and Halliday A. N. (2008) Titanium isotopes and the radial heterogeneity of the solar system. *Earth Planet. Sci. Lett.* **266**, 233–244.

Lord Rayleigh (1896) L. Theoretical considerations respecting the separation of gases by diffusion and similar processes. *London, Edinburgh Dublin Philos. Mag. J. Sci.* **42**, 493–498.

Luck J.-M., Othman D. Ben and Albarède F. (2005) Zn and Cu isotopic variations in chondrites and iron meteorites: Early solar nebula reservoirs and parent-body processes. *Geochim. Cosmochim. Acta* **69**, 5351–5363.

Lugaro M. (2005) *Stardust from Meteorites - An Introduction to Presolar Grains*. World Scie. ed. J. V. Narlikar, World Scientific, Singapore.

Lunine J. I. (2006) Origin of Water Ice in the Solar System. In *Meteorites and the Early Solar System II* (eds. D. S. Lauretta and H. Y. J. McSween). University of Arizona Press, Tucson. pp. 309–319.

Maréchal C. N., Télouk P. and Albarède F. (1999) Precise analysis of copper and zinc isotopic compositions by plasma-source mass spectrometry. *Chem. Geol.* **156**, 251–273.

Marhas K. K., Amari S., Gyngard F., Zinner E. and Roberto G. (2008) Iron and Nickel Isotopic Ratios in Presolar {SiC} Grains. *Astrophys. J.* **689**, 622–645.

Matsumura S. and Pudritz R. E. (2006) Dead zones and extrasolar planetary properties. **584**, 572–584.

McSween H. Y. J. and Huss G. R. (2010) *Cosmochemistry*. 1st ed., Cambridge University Press, Cambridge.

Molini-Vlesko C., Mayeda T. K. and Clayton R. N. (1986) Isotopic composition of silicon in meteorites. *Geochim. Cosmochim. Acta* **50**, 2719–2726.

Mook W. G. (2000) *Environmental Isotopes in the Hydrological Cycle: Principles and Applications Vol.1*., Amsterdam.

Morand P. and Allègre C. J. (1983) Nickel isotopic studies in meteorites. *Earth Planet. Sci. Lett.* **63**, 167–176.

Mostefaoui S. and Hoppe P. (2004) Discovery of abundant in situ silicate and spinel grains from red giant stars in a primitive meteorite. *Astrophys. J.* **613**, L149–L152.

Moynier F., Beck P., Jourdan F., Yin Q.-Z., Reimold U. and Koeberl C. (2009) Isotopic fractionation of zinc in tektites. *Earth Planet. Sci. Lett.* **277**, 482–489.

Moynier F., Bouvier A., Blichert-Toft J., Telouk P., Gasperini D. and Albarède F. (2006) Europium isotopic variations in Allende CAIs and the nature of mass-dependent fractionation in the solar nebula. *Geochim. Cosmochim. Acta* **70**, 4287–4294.

Moynier F., Koeberl C., Beck P., Jourdan F. and Telouk P. (2010) Isotopic fractionation of Cu in tektites. *Geochim. Cosmochim. Acta* **74**, 799–807.

NASA Jet Propulsion Laboratory Stellar Evolution. *Calif. Inst. Technol. JPL Infographics*. Available at: https://www.jpl.nasa.gov/infographics/infographic.view.php?id=10737.

Nguyen A. N. and Messenger S. (2014) Resolving the stellar sources of isotopically rare presolar silicate grains through Mg and Fe isotopic analyses. *Astrophys. J.* **784**, 1–15.

Nguyen A. N., Stadermann F. J., Zinner E., Stroud R. M., Alexander C. M. O. and Nittler L. R. (2007) Characterization of presolar silicate and oxide grains in primitive carbonaceous chondrites. *Astrophys. J.* **656**, 1223–1240.

Niederer F. R., Papanastassiou D. A. and Wasserburg G. J. (1985) Absolute isotopic abundances of Ti in meteorites. *Geochim. Cosmochim. Acta* **49**, 835–851.

Niederer F. R., Papanastassiou D. A. and Wasserburg G. J. (1981) The isotopic composition of titanium in the Allende and Leoville meteorites. *Geochim. Cosmochim. Acta* **45**, 1017–1031.

Niemeyer S. and Lugmair G. W. (1981) Ubiquitous isotopic anomalies in Ti form normal Allende inclusions. *Earth Planet. Sci. Lett.* **53**, 211–225.

Nomoto K., Iwamoto K., Nakasato N., Thielemann F., Brachwitz F., Tsujimoto T., Kubo Y. and Kishimoto N. (1997) Nucleosynthesis in Type Ia Supernovae. *Nucl. Phys. A* **621**, 467c–476c.

Ong W. J. and Floss C. (2015) Iron isotopic measurements in presolar silicate and oxide grains from the Acfer 094 ungrouped carbonaceous chondrite. *Meteorit. Planet. Sci.* **50**, 1392–1407.

Pagel B. E. J. (2008) Neutron capture processes. In *Nucleosynthesis and Chemical Evolution of Galaxies* Cambridge University Press. pp. 206–224.

Palme H. and Boynton W. V (1993) Meteoritic constraints on conditions in the solar nebula. *Protostars planets III* **A93-42937**, 979–1004.

Palme H., Larimer J. W. and Lipschutz M. E. (1988) Moderately volatile elements. In *Meteorites and the early solar system* Tucson. pp. 436–461.

Papanastassiou D. A. (1986) Chromium Isotopic Anomalies in the Allende Meteorite. *Astrophys. J.* **308**, L27–L30.

Papanastassiou D. A. and Brigham C. A. (1989) The Identification of Meteorite Inclusions with Isotope Anomalies. *Astrophys. J.* **338**, L37–L40.

Petitat M., Birck J. L., Luu T. H. and Gounelle M. (2011) The Chromium Isotopic Composition of the Ungrouped Carbonaceous Chondrite Tagish Lake. *Astrophys. J.* **736**, 23.

Pfeifer M., Lloyd N. S., Peters S. T., Wombacher F., Elfers B. M., Schulz T. and Münker C. (2017) Tantalum isotope ratio measurements and isotope abundances determined by MC-ICP-MS using amplifiers equipped with 1010, 1012and 1013Ohm resistors. *J. Anal. At. Spectrom.* **32**, 130–143.

Pignatari M., Gallino R., Heil M., Wiescher M., Käppeler F., Herwig F. and Bisterzo S. (2010) The weak s-process in massive stars and its dependence on the neutron capture cross sections. *Astrophys. J.* **710**, 1557–1577.

Piso A. A., Pegues J. and Oberg K. I. (2016) The role of ice compositions for snowlines and the C/N/O ratios in active disks. *Astrophys. J.* **833**, 203–211.

Podosek F. A., Ott U., Brannon J. C., Neal C. R., Bernatowicz T. J., Swan P. and Mahan S. E. (1997) Thoroughly anomalous chromium in Orgueil. *Meteorit. Planet. Sci.* **32**, 617–627.

Pringle E. A., Moynier F., Beck P., Paniello R. and Hezel D. C. (2017) The origin of volatile element depletion in early solar system material: Clues from Zn isotopes in chondrules. *Earth Planet. Sci. Lett.* **468**, 62–71.

Qin L., Alexander C. M. O., Carlson R. W., Horan M. F. and Yokoyama T. (2010) Contributors to chromium isotope variation of meteorites. *Geochim. Cosmochim. Acta* **74**, 1122–1145.

Regelous M., Elliott T. and Coath C. (2008) Nickel isotope heterogeneity in the early Solar System. *Earth Planet. Sci. Lett.* **272**, 330–338.

Richter F. M. (2004) Timescales determining the degree of kinetic isotope fractionation by evaporation and condensation. *Geochim. Cosmochim. Acta* **68**, 4971–4992.

Richter F. M., Dauphas N. and Teng F.-Z. (2009) Non-traditional fractionation of non-traditional isotopes: Evaporation, chemical diffusion and Soret diffusion. *Chem. Geol.* **258**, 92–103.

Richter F. M., Davis A. M., Ebel D. S. and Hashimoto A. (2002) Elemental and isotopic fractionation of type B calcium-, aluminum-rich inclusions: Experiments, theoretical considerations, and constraints on their thermal evolution. *Geochim. Cosmochim. Acta* **66**, 521–540.

Richter F. M., Huss G. R. and Mendybaev R. A. (2014) Iron and Nickel Isotopic Fractionation Across Metal Grains from Three CBb Meteorites. In *Lunar and Planetary Science Conference* p. 1346.

Richter F. M., Janney P. E., Mendybaev R. A., Davis A. M. and Wadhwa M. (2007) Elemental and isotopic fractionation of Type B CAI-like liquids by evaporation. *Geochim. Cosmochim. Acta* **71**, 5544–5564.

Richter F. M., Mendybaev R. A., Christensen J. N., Ebel D. S. and Gaffney A. (2011) Laboratory experiments bearing on the origin and evolution of olivine-rich chondrules. *Meteorit. Planet. Sci.* **46**, 1152–1178.

Rotaru M., Birck J. L. and Allègre C. J. (1992) Clues to early Solar System history from chromium isotopes in carbonaceous chondrites. *Nature* **355**, 242–244.

Russell W. A., Papanastassiou D. A. and Tombrello T. A. (1978) Ca isotope fractionation on the Earth and other solar system materials. *Geochim. Cosmochim. Acta* **42**, 1075–1090.

Scherstén A., Elliott T., Hawkesworth C., Russell S. and Masarik J. (2006) Hf-W evidence for rapid differentiation of iron meteorite parent bodies. *Earth Planet. Sci. Lett.* **241**, 530–542.

Van Schmus W. R. and Wood J. A. (1967) A chemical-petrologic classification for the chondritic meteorites. **31**, 747–765.

Scott E. R. D. and Krot A. N. (2013) 1.2 - Chondrites and Their Components. In *Treatise on Geochemistry* Elsevier Ltd. pp. 65–137.

Shipman J. T., Wilson J. D. and Higgins C. A. (2012) *An introduction to physical science*., Brooks/Cole, Cengage Learning.

Shollenberger Q. R., Brennecka G. A., Schuth S. and Weyer S. (2016) Iron isotope systematics of refractory inclusions. In *Annual Meeting of the Meteoritical Society* p. Abstract #6364.

Shollenberger Q. R., Brennecka G. A., Schuth S. and Weyer S. (2017) Iron Isotope Systematics of Refractory Inclusions and the Search for the Source of Nucleosynthetic Anomalies. In *Lunar and Planetary Institute Conference Abstracts* p. Abstract #1867.

Shukolyukov A. and Lugmair G. W. (2006) Manganese-chromium isotope systematics of carbonaceous chondrites. *Earth Planet. Sci. Lett.* **250**, 200–213.

Shukolyukov A. and Lugmair G. W. (2000) On the 53Mn Heterogeneity in the Early Solar System. *Sp. Sci. Rev.* **92**, 225–236.

Simon J. I., Cuzzi J. N., McCain K. A., Cato M. J., Christoffersen P. A., Fisher K. R., Srinivasan P., Tait A. W., Olson D. M. and Scargle J. D. (2018) Particle size distributions in chondritic meteorites: Evidence for pre-planetesimal histories. *Earth Planet. Sci. Lett.* **494**, 69–82.

Simon J. I., Jordan M. K., Tappa M. J., Schauble E. A., Kohl I. E. and Young E. D. (2017) Calcium and titanium isotope fractionation in refractory inclusions: Tracers of condensation and inheritance in the early solar protoplanetary disk. *Earth Planet. Sci. Lett.* **472**, 277–288.

Simon J. I. and Young E. D. (2007) Evaporation and Mg Isotope Fractionation: Model Constraints for CAIs. In *Lunar and Planetary Institute Conference Abstracts* p. Abstract #2424.

Steele R. C. J., Coath C., Regelous M., Russell S. and Elliott T. (2012) Neutron-Poor Nickel Isotope Anomalies in Meteorites. *Astrophys. J.* **758**, 59.

Steinhoefel G., Horn I. and Blanckenburg F. Von (2009) Matrix-independent Fe isotope ratio determination in silicates using UV femtosecond laser ablation. *Chem. Geol.* **268**, 67–73.

Stevenson D. J. and Lunine J. I. (1988) Rapid Formation of Jupiter by Diffusive Redestribution of Water Vapor in the Solar Nebula. **75**, 146–155.

Straniero O., Gallino R. and Cristallo S. (2006) S Process in Low-Mass Asymptotic Giant Branch Stars. *Nucl. Phys. A* **777**, 311–339.

Supulver K. D. and Lin D. N. C. (2000) Formation of Icy Planetesimals in a Turbulent Solar Nebula. *Icarus* **146**, 525–540.

Tang H. and Dauphas N. (2012) Abundance, distribution, and origin of 60Fe in the solar protoplanetary disk. *Earth Planet. Sci. Lett.* **359**–**360**, 248–263.

Thielemann F. (1984) Nucleosynthesis in Type I and Type II Supernovae. *Adv. Sp. Res.* **4**, 67–73.

Toutain J.-P., Sonke J., Munoz M., Nonell A., Polvé M., Viers J., Freydier R., Sortino F., Joron J.-L. and Sumarti S. (2008) Evidence for Zn isotopic fractionation at Merapi volcano. *Chem. Geol.* **253**, 74–82.

Trappitsch R., Stephan T., Savina M. R., Davis A. M., Pellin M. J., Rost D., Gyngard F., Gallino R., Bisterzo S., Cristallo S. and Dauphas N. (2018) Simultaneous iron and nickel isotopic analyses of presolar silicon carbide grains. *Geochim. Cosmochim. Acta* **221**, 87–108.

Trinquier A., Birck J. L. and Allègre C. J. (2007) Widespread 54Cr Heterogeneity in the Inner Solar System. *Astrophys. J.* **655**, 1179–1185.

Trinquier A., Birck J. L., Allègre C. J., Göpel C. and Ulfbeck D. (2008) 53Mn–53Cr systematics of the early Solar System revisited. *Geochim. Cosmochim. Acta* **72**, 5146–5163.

Trinquier A., Elliott T., Ulfbeck D., Coath C., Krot A. N. and Bizzarro M. (2009) Origin of nucleosynthetic isotope heterogeneity in the solar protoplanetary disk. *Science (80-.).* **324**, 374–376.

Tripa C. E., Pellin M. J., Savina M. R., Davis A. M., Lewis R. S. and Clayton R. N. (2002) Fe Isotopic Composition of Presolar SiC Mainstream Grains. In *Lunar and Planetary Science Conference* p. Abstract #1975.

Uyeda C., Tsuchiyama A. and Okano J. (1991) Magnesium isotopic fractionation of silicates produced in condensation experiments. *Earth Planet. Sci. Lett.* **107**, 138–147.

Voelkening J. and Papanastassiou D. A. (1989) Iron isotope anomalies. *Astrophys. J.* **347**, L43–L46.

Vollmer C. and Hoppe P. (2010) First Fe Isotopic Measurement of a highly 17O-enriched Stardust Silicate. In *Lunar and Planetary Science Conference* p. Abstract #1200.

Walsh K. J., Morbidelli A., Raymond S. N., O'Brien D. P. and Mandell A. M. (2011) A low mass for Mars from Jupiter's early gas-driven migration. *Nature* **475**, 206–209.

Wang K. and Jacobsen S. B. (2016) Potassium isotopic evidence for a high-energy giant impact origin of the Moon. *Nature* **538**, 487–490.

Wang K., Moynier F., Barrat J. A., Zanda B., Paniello R. C. and Savage P. S. (2013) Homogeneous distribution of Fe isotopes in the early solar nebula. *Meteorit. Planet. Sci.* **48**, 354–364.

Wang K., Moynier F., Podosek F. A. and Foriel J. (2011) 58 Fe and 54 Cr in early Solar System Materials. *Astrophys. J.* **739**, L58.

Warren P. H. (2011) Stable-isotopic anomalies and the accretionary assemblage of the Earth and Mars: A subordinate role for carbonaceous chondrites. *Earth Planet. Sci. Lett.* **311**, 93–100.

Wasserburg G. J., Trippella O. and Busso M. (2015) Isotopic anomalies in Cr, Fe and Ni from "s" processin in AGB stars. In *Lunar and Planetary Science Conference* p. Abstract #1204.

Wasson J. T. and Kallemeyn G. W. (1988) Compositions of Chondrites. *Philos. Trans.* **325**, 535–544.

Weyer S. and Schwieters J. B. (2003) High precision Fe isotope measurements with high mass resolution MC-ICPMS. *Int. J. Mass Spectrom.* **226**, 355–368.

Weyrauch M., Zipfel J. and Weyer S. (2017) Formation conditions of zoned and unzoned metal grains in CB and CH chondrites. In *Annual Meeting of the Meteoritical Society* p. 6192.

Williams C. D., Janney P. E., Hines R. R. and Wadhwa M. (2016) Precise titanium isotope compositions of refractory inclusions in the Allende CV3 chondrite by LA-MC-ICPMS. *Chem. Geol.* **436**, 1–10.

Wombacher F., Rehkämper M. and Mezger K. (2004) Determination of the mass-dependence of cadmium isotope fractionation during evaporation. *Geochim. Cosmochim. Acta* **68**, 2349–2357.

Wombacher F., Rehkämper M., Mezger K., Bischoff A. and Münker C. (2008) Cadmium stable isotope cosmochemistry. *Geochim. Cosmochim. Acta* **72**, 646–667.

Wombacher F., Rehkämper M., Mezger K. and Münker C. (2003) Stable isotope compositions of cadmium in geological materials and meteorites determined by multiple-collector ICPMS. *Geochim. Cosmochim. Acta* **67**, 4639–4654.

Woosley S. E. (1997) Neutron-rich Nucleosynthesis in Carbon Deflagration Supernovae. *Astrophys. J.* **476**, 801–810.

Zambardi T., Sonke J. E., Toutain J. P., Sortino F. and Shinohara H. (2009) Mercury emissions and stable isotopic compositions at Vulcano Island (Italy). *Earth Planet. Sci. Lett.* **277**, 236–243.

Zhang B., Chang R. and Peng Q. (1998) Evolution of the surface abundance of a 3 M⊙ AGB star. *Chinese Astron. Astrophys.* **22**, 49–55.

Zhang J., Dauphas N., Davis A. M. and Pourmand A. (2011) A new method for MC-ICPMS measurement of titanium isotopic composition: Identification of correlated isotope anomalies in meteorites. *J. Anal. At. Spectrom.* **26**, 2197.

Zhang J., Huang S., Davis A. M., Dauphas N., Hashimoto A. and Jacobsen S. B. (2014) Calcium and titanium isotopic fractionations during evaporation. *Geochim. Cosmochim. Acta* **140**, 365–380.

Zhu X. K., Guo Y., O'Nions R. K., Young E. D. and Ash R. D. (2001) Isotopic homogeneity of iron in the early solar nebula. *Nature* **412**, 311–313.

Zinner E. (2013) 1.4 - Presolar Grains. In *Treatise on Geochemistry* Elsevier Ltd. pp. 181–213.

Zinner E., Amari S., Guinness R., Jennings C., Mertz A. F., Nguyen A. N., Gallino R., Hoppe P., Lugaro M., Nittler L. R. and Lewis R. S. (2007) NanoSIMS isotopic analysis of small presolar grains: Search for Si3N4 grains from AGB stars and Al and Ti isotopic compositions of rare presolar SiC grains. *Geochim. Cosmochim. Acta* **71**, 4786–4813.

Zipfel J. and Weyer S. (2007) In Situ Analyses of Fe Isotopes in Zoned Metal Grains of Hammadah Al Hamra 237. In p. 1927.

Appendix

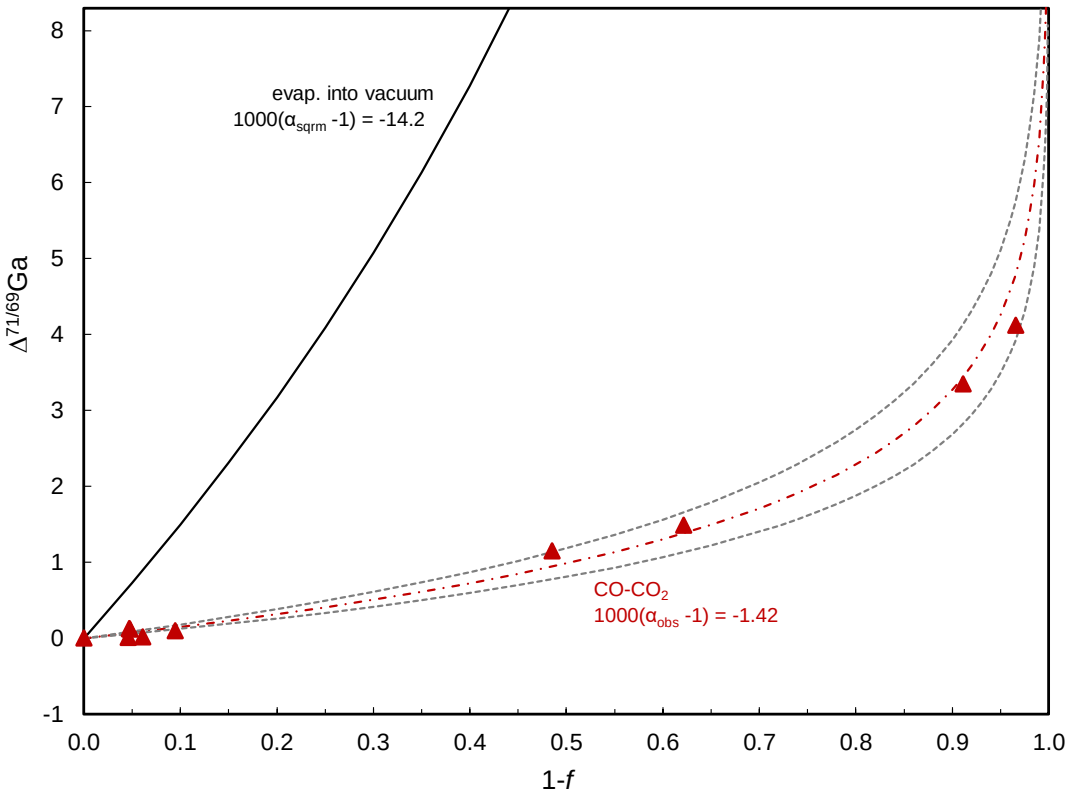

Figure A.1. Rayleigh fractionation of Ga due to evaporation, where f is the mass fraction of Ga left in residues. Red dashed curve fitted to red triangles for experiment 1 (CO-CO_2); the black solid curve is for evaporation into vacuum as calculated using $\alpha_{kin} = \frac{\gamma_2}{\gamma_1}\sqrt{\frac{m_1}{m_2}}$ with $\gamma_1/\gamma_2 = 1$.

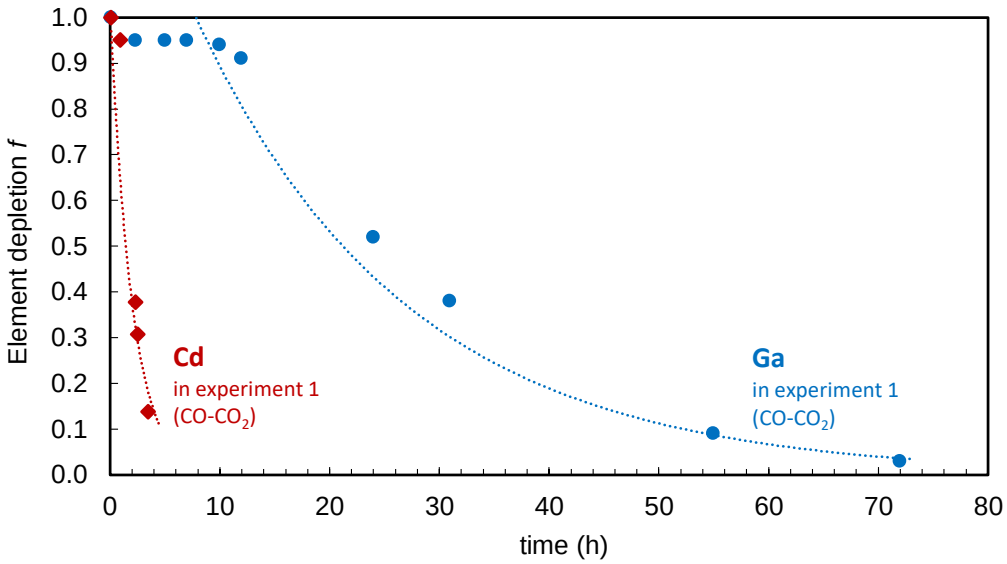

Figure A.2. Element depletion of Cd and Ga vs. time in experiment 1 (CO-CO_2).

Gallium was separated from melt residue samples and condensates (Table A.1) and analyzed using a Thermo Scientific Neptune multi-collector ICP-MS in high resolution and glassware sample introduction. External mass bias correction was done using $^{66}Zn/^{67}Zn$. For $\delta^{71/69}Ga$ 2 s.d. = ± 0.10 ‰.

Table A.1. Cadmium and gallium separation via column chromatography adapted from Maréchal et al. (1999) and Wombacher et al. (2003) and Cd clean-up.

a.

	ml	**acid**
load	1	10 M HCl
matrix	2 x 1	10 M HCl
	2 x 3	10 M HCl
(Cu)	3 x 3	5 M HCl
Ga (Fe,Te)	2 x 2.5	1 M HCl
(Zn, Sn)	2 x 2.5	0.05 M HCl
Cd	2 x 2	0.56 M HNO_3

b.

	ml	**acid**
load + collect **Cd**	0.2	8 M HCl
Cd	0.2	8 M HCl
Cd	2 x 1	6 M HCl

a. Gallium and Cd separation procedure using 1 ml MP1 anion exchanger.
b. Cd clean-up procedure using 150 µl Eichrom TRU resin and 150 µl pre-filter.

Table A.2. Melt residue samples of experiment 1

Sample	**t (h)**	**depletion *f***	**$\Delta^{71/69}Ga$**
1-0	0.10	1.00	0.000
1-9	2.32	0.95	0.005
1-15	5.00	0.95	0.115
1-18	6.99	0.95	0.127
1-21	9.99	0.94	0.019
1-23	11.99	0.91	0.096
1-24	24.03	0.52	1.149
1-25	31.00	0.38	1.483
1-27	55.00	0.09	3.344
1-28	72.00	0.03	4.123

$\Delta^{71/69}Ga$ normalized to first sample 1-0.

Table A.3. Iron concentration, Fe fraction in percent of bulk sample and amount of Fe loaded for separation.

sample	µg Fe	% fraction	µg Fe loaded
LP8 basalt			
bulk	88617		
LP L2	7273	8.2	1000
LP R	256	0.3	256
Allende CV3			
bulk	252321		
ALL L1	193975	77	1000
ALL L2	55520	22	1000
ALL R	2826	1.1	1000
Kainsaz CO3.2			
bulk	2611		
KAIN L1	1960	75	392
KAIN L2	125	4.8	125
KAIN R	526	20	421
Cold Bokkeveld CM2			
bulk	37208		
CO BO L1	34852	94	1000
CO BO L2	2315	6.2	1000
CO BO R	40	0.1	40
Murchison CM2			
bulk	1070175		
MUR L1	63296	5.9	1000
MUR L2	737917	69	1000
MUR L3	211396	20	1000
MUR L4	42359	4.0	1000
MUR R	15206	1.4	1000
Indarch EH4			
bulk	298865		
IND L1	283187	95	1000
IND L2	13459	4.5	1000
IND R	2220	0.7	1000
QUE 97008 L3.05			
bulk	26789		
QUE L1	18863	70	1000
QUE R	51	0.2	51

Table A.4. Iron-56 intensities in V* and effect of interference correction for ^{54}Cr and ^{58}Ni in ppm.

sample	^{56}Fe (V*)	Intensity dev. (%)	^{54}Cr on $^{57}Fe/^{54}Fe$	^{54}Cr, ^{58}Ni on $^{58}Fe/^{54}Fe$
IRMM-014				
IRMM-3	425	4.4	1	-26
IRMM-3	384	4.6	0	-28
IRMM-3	370	11.7	0	-24
IRMM-4	395	4.3	1	-38
IRMM-5	367	-2.5	1	-37
IRMM-5	359	-1.0	1	-41
IRMM-5	355	1.3	1	-39
IRMM-6	241	-4.7	1	-67
IRMM-6	236	-4.1	1	-63
IRMM-7	377	5.8	0	-42
IRMM-7	361	4.1	0	-45
IRMM-7	362	2.0	0	-45
La Palma basalt 8				
LP L2-4	399	6.8	1	-36
LP L2-5	352	0.2	1	-44
LP L2-7	349	-0.1	1	-43
LP R-4	384	3.9	3	-63
LP R-5	360	2.9	3	-65
LP R-6	255	1.6	3	-105
LP R-6	254	2.4	3	-108
Allende CV3 bulk				
ALL-2	425	1.7	15	-217
ALL-2	425	1.9	15	-219
ALL-2	418	1.9	15	-212
ALL-2	415	1.4	15	-211
ALL-2	411	1.8	15	-217
ALL-2	406	0.9	15	-213
ALL-2	402	0.1	15	-215
ALL-2	399	-0.3	15	-214
Allende CV3				
ALL L1-5	390	4.1	41	-130
ALL L1-7	374	8.1	41	-131
ALL L1-8	362	-2.8	41	-137
ALL L2-5	422	13.4	5	-106
ALL L2-7	363	4.5	5	-110
ALL L2-8	348	-4.9	5	-109
ALL R-4	406	9.7	13	-1574
ALL R-5	373	0.5	13	-1568
ALL R-8	326	-9.9	14	-1549

sample	^{56}Fe (V*)	Intensity dev. (%)	^{54}Cr on ^{57}Fe/^{54}Fe	^{54}Cr, ^{58}Ni on ^{58}Fe/^{54}Fe
Kainsaz CO3.2				
KAIN L1-2	416	1.6	3	-118
KAIN L1-7	470	31.8	3	-112
KAIN L2-2	414	2.5	10	-384
KAIN R-2	416	2.1	30	-402
KAIN R-7	456	28.8	29	-415
Murchison CM2				
MUR L1-3	387	-4.0	2	-284
MUR L1-3	343	-3.1	2	-277
MUR L1-5	351	-5.5	2	-281
MUR L1-7	342	-1.1	2	-280
MUR L2-3	381	-4.4	1	-102
MUR L2-3	332	-1.5	1	-102
MUR L2-5	352	-5.3	1	-117
MUR L3-3	382	-2.5	1	-128
MUR L3-3	343	2.8	1	-123
MUR L3-5	356	-4.4	2	-136
MUR L4-3	393	1.5	98	-79
MUR L4-3	345	1.4	98	-71
MUR L4-5	365	-2.1	99	-83
MUR R-3	377	-0.8	23	-24
MUR R-3	341	2.3	23	-25
MUR R-5	355	1.1	24	-36
MUR R-7	344	-0.3	23	-29
Cold Bokkeveld CM2				
CO BO L1-3	370	-1.5	1	-158
CO BO L1-3	327	-0.5	1	-155
CO BO L1-5	355	1.0	1	-165
CO BO L2-3	379	1.4	5	-1640
CO BO L2-3	326	2.5	5	-1652
CO BO L2-5	368	4.9	5	-1603
CO BO R-6	250	0.1	78	-121
Indarch EH4				
IND L1-4	371	0.8	1	-139
IND L1-7	347	1.0	1	-136
IND L1-8	346	-2.8	1	-134
IND L2-4	363	-1.4	10	-613
IND L2-7	337	-2.5	10	-614
IND L2-8	337	-5.2	10	-599
IND R-4	360	-2.6	3	-156
IND R-5	349	-0.3	3	-151
IND R-7	337	-2.1	2	-168

sample	^{56}Fe (V*)	Intensity dev. (%)	^{54}Cr on ^{57}Fe/^{54}Fe	^{54}Cr, ^{58}Ni on ^{58}Fe/^{54}Fe
QUE 97008 L3.05				
QUE L1-4	350	-5.4	1	-211
QUE L1-5	342	-2.4	1	-205
QUE L1-8	327	-9.0	1	-251
QUE R-6	245	-1.9	229	-25
Murchison CM2[a]				
MUR L1-9	416	2.4	1	-255
MUR L1-9	407	2.3	2	-254
MUR L3-9	410	2.1	1	-120
MUR L4-9	423	5.8	99	-64
MUR R-9	405	0.4	23	-37
MUR R-9	400	1.0	23	-29
Cold Bokkeveld CM2[b]				
CO BO L2-9	422	2.2	5	-1546
CO BO L2-9	424	3.2	5	-1543
Indarch EH4[c]				
IND L2-9	408	-0.5	10	-585
IND R-9	399	-2.7	2	-144
IND R-9	400	-2.7	2	-147

All samples measured using Fe inhouse standard for sample-standard bracketing, except: [a] bracketed using Murchison L2; [b] bracketed using Cold Bokkeveld L1; [c] bracketed using Indarch L1.

Table A.5. Linearized δ'-values of mass-dependent Fe isotope ratios relative to Fe in-house standard.

sample	$\delta'^{56}Fe$	2se	$\delta'^{57}Fe$	2se	$\delta'^{58}Fe$	2se
IRMM-014						
IRMM-3	0.210	0.012	0.317	0.015	0.414	0.024
IRMM-3	0.171	0.024	0.251	0.021	0.322	0.029
IRMM-3	0.021	0.016	-0.002	0.016	-0.012	0.026
IRMM-4	0.249	0.017	0.359	0.024	0.473	0.036
IRMM-5	0.314	0.015	0.465	0.023	0.612	0.032
IRMM-5	0.243	0.012	0.358	0.018	0.470	0.026
IRMM-5	0.228	0.013	0.329	0.017	0.435	0.026
IRMM-6	0.231	0.016	0.336	0.022	0.423	0.033
IRMM-6	0.230	0.014	0.333	0.018	0.440	0.028
IRMM-7	0.282	0.022	0.421	0.032	0.557	0.042
IRMM-7	0.340	0.017	0.509	0.017	0.666	0.025
IRMM-7	0.286	0.021	0.423	0.028	0.535	0.037
La Palma basalt 8						
LP L2-4	0.380	0.016	0.560	0.022	0.749	0.032
LP L2-5	0.540	0.013	0.803	0.018	1.064	0.028
LP L2-7	0.343	0.020	0.510	0.028	0.683	0.039
LP R-4	0.479	0.013	0.708	0.013	0.928	0.021
LP R-5	0.519	0.011	0.764	0.015	1.015	0.023
LP R-6	0.530	0.016	0.778	0.022	1.014	0.033
LP R-6	0.489	0.015	0.722	0.019	0.918	0.031
Allende CV3 bulk						
ALL-2	0.258	0.019	0.392	0.023	0.512	0.035
ALL-2	0.336	0.016	0.498	0.022	0.647	0.031
ALL-2	0.379	0.022	0.578	0.032	0.744	0.044
ALL-2	0.398	0.018	0.598	0.025	0.775	0.036
ALL-2	0.185	0.027	0.285	0.040	0.344	0.054
ALL-2	0.236	0.018	0.357	0.024	0.433	0.035
ALL-2	0.257	0.016	0.383	0.021	0.480	0.031
ALL-2	0.247	0.016	0.382	0.018	0.460	0.028
Allende CV3						
ALL L1-5	0.261	0.013	0.392	0.018	0.520	0.026
ALL L1-7	0.280	0.018	0.430	0.022	0.580	0.032
ALL L1-8	0.240	0.015	0.368	0.021	0.473	0.030
ALL L2-5	0.185	0.014	0.281	0.020	0.391	0.029
ALL L2-7	0.335	0.017	0.515	0.020	0.682	0.028
ALL L2-8	0.227	0.013	0.345	0.016	0.449	0.023
ALL R-4	0.640	0.013	0.955	0.013	1.267	0.022
ALL R-5	0.636	0.012	0.954	0.017	1.249	0.024
ALL R-8	0.693	0.015	1.034	0.016	1.379	0.024

sample	$\delta'^{56}Fe$	2se	$\delta'^{57}Fe$	2se	$\delta'^{58}Fe$	2se
Kainsaz CO3.2						
KAIN L1-2	0.222	0.016	0.334	0.021	0.438	0.028
KAIN L1-7	0.250	0.016	0.376	0.019	0.493	0.027
KAIN L2-2	0.119	0.012	0.181	0.012	0.249	0.021
KAIN R-2	0.244	0.013	0.369	0.013	0.473	0.024
KAIN R-7	0.262	0.016	0.396	0.016	0.530	0.023
Murchison CM2						
MUR L1-3	-0.858	0.012	-1.254	0.015	-1.659	0.023
MUR L1-3	-0.952	0.033	-1.377	0.028	-1.849	0.044
MUR L1-5	-0.781	0.014	-1.135	0.019	-1.507	0.028
MUR L1-7	-0.835	0.016	-1.223	0.018	-1.627	0.025
MUR L2-3	0.308	0.012	0.451	0.015	0.595	0.022
MUR L2-3	0.266	0.025	0.398	0.019	0.510	0.029
MUR L2-5	0.243	0.015	0.365	0.020	0.473	0.028
MUR L3-3	0.370	0.012	0.552	0.012	0.715	0.022
MUR L3-3	0.185	0.021	0.267	0.013	0.336	0.022
MUR L3-5	0.378	0.013	0.583	0.018	0.774	0.028
MUR L4-3	0.090	0.015	0.145	0.014	0.170	0.023
MUR L4-3	0.030	0.028	0.055	0.013	0.078	0.021
MUR L4-5	0.123	0.010	0.202	0.012	0.265	0.020
MUR R-3	0.688	0.017	1.023	0.016	1.335	0.025
MUR R-3	0.534	0.018	0.790	0.015	1.033	0.025
MUR R-5	0.585	0.012	0.868	0.012	1.151	0.021
MUR R-7	0.725	0.017	1.080	0.018	1.427	0.029
Cold Bokkeveld CM2						
CO BO L1-3	0.182	0.024	0.273	0.021	0.357	0.028
CO BO L1-3	0.238	0.017	0.357	0.013	0.459	0.021
CO BO L1-5	0.299	0.012	0.448	0.016	0.599	0.025
CO BO L2-3	0.201	0.023	0.301	0.020	0.391	0.029
CO BO L2-3	0.285	0.019	0.424	0.017	0.582	0.027
CO BO L2-5	0.227	0.014	0.344	0.020	0.462	0.029
CO BO R-6	0.549	0.016	0.819	0.023	1.124	0.034
Indarch EH4						
IND L1-4	0.220	0.011	0.324	0.013	0.433	0.022
IND L1-7	0.280	0.015	0.421	0.016	0.552	0.025
IND L1-8	0.226	0.018	0.331	0.020	0.422	0.028
IND L2-4	0.216	0.014	0.317	0.016	0.412	0.025
IND L2-7	0.318	0.018	0.480	0.020	0.629	0.032
IND L2-8	0.255	0.014	0.380	0.013	0.489	0.020
IND R-4	0.688	0.012	1.006	0.017	1.311	0.025
IND R-5	0.776	0.013	1.141	0.016	1.487	0.025
IND R-7	0.915	0.015	1.368	0.013	1.782	0.022

sample	$\delta'^{56}Fe$	2se	$\delta'^{57}Fe$	2se	$\delta'^{58}Fe$	2se
QUE 97008 L3.05						
QUE L1-4	0.215	0.012	0.322	0.016	0.412	0.023
QUE L1-5	0.209	0.013	0.313	0.017	0.404	0.027
QUE L1-8	0.252	0.016	0.374	0.020	0.468	0.030
QUE R-6	0.666	0.020	0.986	0.027	1.290	0.039
Murchison CM2[a]						
MUR L1-9	-1.203	0.012	-1.781	0.014	-2.346	0.022
MUR L1-9	-1.211	0.012	-1.798	0.014	-2.380	0.022
MUR L3-9	0.026	0.013	0.040	0.015	0.062	0.023
MUR L4-9	-0.303	0.013	-0.452	0.014	-0.582	0.021
MUR R-9	0.399	0.012	0.597	0.014	0.787	0.023
MUR R-9	0.450	0.013	0.673	0.013	0.898	0.021
Cold Bokkeveld CM2[b]						
CO BO L2-9	0.040	0.013	0.060	0.013	0.084	0.020
CO BO L2-9	-0.037	0.013	-0.057	0.014	-0.077	0.023
Indarch EH4[c]						
IND L2-9	0.000	0.016	0.001	0.018	0.007	0.026
IND R-9	0.568	0.016	0.843	0.014	1.096	0.021
IND R-9	0.507	0.014	0.747	0.013	0.977	0.022

All samples measured using Fe inhouse standard for sample-standard bracketing, except: [a] bracketed using Murchison L2; [b] bracketed using Cold Bokkeveld L1; [c] bracketed using Indarch L1.

Table A.6. Linearized δ'-values of mass-dependent Fe isotope ratios relative to IRMM-014

sample	$\delta'^{56}Fe$	2se	$\delta'^{57}Fe$	2se	$\delta'^{58}Fe$	2se
IRMM-014						
IRMM-3	0.210	0.012	0.317	0.015	0.414	0.024
IRMM-3	0.171	0.024	0.251	0.021	0.322	0.029
IRMM-3	0.021	0.016	-0.002	0.016	-0.012	0.026
IRMM-4	0.249	0.017	0.359	0.024	0.473	0.036
IRMM-5	0.314	0.015	0.465	0.023	0.612	0.032
IRMM-5	0.243	0.012	0.358	0.018	0.470	0.026
IRMM-5	0.228	0.013	0.329	0.017	0.435	0.026
IRMM-6	0.231	0.016	0.336	0.022	0.423	0.033
IRMM-6	0.230	0.014	0.333	0.018	0.440	0.028
IRMM-7	0.282	0.022	0.421	0.032	0.557	0.042
IRMM-7	0.340	0.017	0.509	0.017	0.666	0.025
IRMM-7	0.286	0.021	0.423	0.028	0.535	0.037
La Palma basalt 8						
LP L2-4	0.380	0.016	0.560	0.022	0.749	0.032
LP L2-5	0.540	0.013	0.803	0.018	1.064	0.028
LP L2-7	0.343	0.020	0.510	0.028	0.683	0.039
LP R-4	0.479	0.013	0.708	0.013	0.928	0.021
LP R-5	0.519	0.011	0.764	0.015	1.015	0.023
LP R-6	0.530	0.016	0.778	0.022	1.014	0.033
LP R-6	0.489	0.015	0.722	0.019	0.918	0.031
Allende CV3 bulk						
ALL-2	0.258	0.019	0.392	0.023	0.512	0.035
ALL-2	0.336	0.016	0.498	0.022	0.647	0.031
ALL-2	0.379	0.022	0.578	0.032	0.744	0.044
ALL-2	0.398	0.018	0.598	0.025	0.775	0.036
ALL-2	0.185	0.027	0.285	0.040	0.344	0.054
ALL-2	0.236	0.018	0.357	0.024	0.433	0.035
ALL-2	0.257	0.016	0.383	0.021	0.480	0.031
ALL-2	0.247	0.016	0.382	0.018	0.460	0.028
Allende CV3						
ALL L1-5	0.261	0.013	0.392	0.018	0.520	0.026
ALL L1-7	0.280	0.018	0.430	0.022	0.580	0.032
ALL L1-8	0.240	0.015	0.368	0.021	0.473	0.030
ALL L2-5	0.185	0.014	0.281	0.020	0.391	0.029
ALL L2-7	0.335	0.017	0.515	0.020	0.682	0.028
ALL L2-8	0.227	0.013	0.345	0.016	0.449	0.023
ALL R-4	0.640	0.013	0.955	0.013	1.267	0.022
ALL R-5	0.636	0.012	0.954	0.017	1.249	0.024
ALL R-8	0.693	0.015	1.034	0.016	1.379	0.024

sample	$\delta'^{56}Fe$	2se	$\delta'^{57}Fe$	2se	$\delta'^{58}Fe$	2se
Kainsaz CO3.2						
KAIN L1-2	0.222	0.016	0.334	0.021	0.438	0.028
KAIN L1-7	0.250	0.016	0.376	0.019	0.493	0.027
KAIN L2-2	0.119	0.012	0.181	0.012	0.249	0.021
KAIN R-2	0.244	0.013	0.369	0.013	0.473	0.024
KAIN R-7	0.262	0.016	0.396	0.016	0.530	0.023
Murchison CM2						
MUR L1-3	-0.858	0.012	-1.254	0.015	-1.659	0.023
MUR L1-3	-0.952	0.033	-1.377	0.028	-1.849	0.044
MUR L1-5	-0.781	0.014	-1.135	0.019	-1.507	0.028
MUR L1-7	-0.835	0.016	-1.223	0.018	-1.627	0.025
MUR L2-3	0.308	0.012	0.451	0.015	0.595	0.022
MUR L2-3	0.266	0.025	0.398	0.019	0.510	0.029
MUR L2-5	0.243	0.015	0.365	0.020	0.473	0.028
MUR L3-3	0.370	0.012	0.552	0.012	0.715	0.022
MUR L3-3	0.185	0.021	0.267	0.013	0.336	0.022
MUR L3-5	0.378	0.013	0.583	0.018	0.774	0.028
MUR L4-3	0.090	0.015	0.145	0.014	0.170	0.023
MUR L4-3	0.030	0.028	0.055	0.013	0.078	0.021
MUR L4-5	0.123	0.010	0.202	0.012	0.265	0.020
MUR R-3	0.688	0.017	1.023	0.016	1.335	0.025
MUR R-3	0.534	0.018	0.790	0.015	1.033	0.025
MUR R-5	0.585	0.012	0.868	0.012	1.151	0.021
MUR R-7	0.725	0.017	1.080	0.018	1.427	0.029
Cold Bokkeveld CM2						
CO BO L1-3	0.182	0.024	0.273	0.021	0.357	0.028
CO BO L1-3	0.238	0.017	0.357	0.013	0.459	0.021
CO BO L1-5	0.299	0.012	0.448	0.016	0.599	0.025
CO BO L2-3	0.201	0.023	0.301	0.020	0.391	0.029
CO BO L2-3	0.285	0.019	0.424	0.017	0.582	0.027
CO BO L2-5	0.227	0.014	0.344	0.020	0.462	0.029
CO BO R-6	0.549	0.016	0.819	0.023	1.124	0.034
Indarch EH4						
IND L1-4	0.220	0.011	0.324	0.013	0.433	0.022
IND L1-7	0.280	0.015	0.421	0.016	0.552	0.025
IND L1-8	0.226	0.018	0.331	0.020	0.422	0.028
IND L2-4	0.216	0.014	0.317	0.016	0.412	0.025
IND L2-7	0.318	0.018	0.480	0.020	0.629	0.032
IND L2-8	0.255	0.014	0.380	0.013	0.489	0.020
IND R-4	0.688	0.012	1.006	0.017	1.311	0.025
IND R-5	0.776	0.013	1.141	0.016	1.487	0.025
IND R-7	0.915	0.015	1.368	0.013	1.782	0.022

sample	$\delta'^{56}Fe$	2se	$\delta'^{57}Fe$	2se	$\delta'^{58}Fe$	2se
QUE 97008 L3.05						
QUE L1-4	0.215	0.012	0.322	0.016	0.412	0.023
QUE L1-5	0.209	0.013	0.313	0.017	0.404	0.027
QUE L1-8	0.252	0.016	0.374	0.020	0.468	0.030
QUE R-6	0.666	0.020	0.986	0.027	1.290	0.039
Murchison CM2[a]						
MUR L1-9	-1.203	0.012	-1.781	0.014	-2.346	0.022
MUR L1-9	-1.211	0.012	-1.798	0.014	-2.380	0.022
MUR L3-9	0.026	0.013	0.040	0.015	0.062	0.023
MUR L4-9	-0.303	0.013	-0.452	0.014	-0.582	0.021
MUR R-9	0.399	0.012	0.597	0.014	0.787	0.023
MUR R-9	0.450	0.013	0.673	0.013	0.898	0.021
Cold Bokkeveld CM2[b]						
CO BO L2-9	0.040	0.013	0.060	0.013	0.084	0.020
CO BO L2-9	-0.037	0.013	-0.057	0.014	-0.077	0.023
Indarch EH4[c]						
IND L2-9	0.000	0.016	0.001	0.018	0.007	0.026
IND R-9	0.568	0.016	0.843	0.014	1.096	0.021
IND R-9	0.507	0.014	0.747	0.013	0.977	0.022

All samples measured using Fe inhouse standard for sample-standard bracketing, except: [a] bracketed using Murchison L2; [b] bracketed using Cold Bokkeveld L1; [c] bracketed using Indarch L1.

Acknowledgements

I want to thank Frank Wombacher for making this thesis possible. Thank you for believing in this project, for supervising me throughout all those years, for giving me the chance to develop my scientific skills, for sharing your knowledge and for countless discussions. You made me not only be a scientist but also a cleverer, braver person.

Thank you both, Frank and Carsten, for the great opportunity to learn from you.

Many thanks also to Dominik for his help, his interest in my work and his positivity.

Thanks also to Werner Ertel-Ingrisch for providing the experimental samples.

Special thanks to Bo for working with me and providing samples, his time and knowledge and not at least entertainment. Oink oink!

Further, I want to thank all my colleagues, especially Pia, Julia, Ninja, Christiane, Markus H., Markus P., Claudia and Stefan, who supported me with lively discussions and heart-warming encouragement during my time at the Institute. I am very happy you were around!

Aurelia was the person that kept me laughing, even on difficult days. I can’t thank her enough for being such a good friend.

Pat was always there for me when I needed a pep talk. I thank her so much for inspiring me.

I thank my friends Silke, Marie and Janina for literally everything and I am very thankful that all of my friends always believed in me!

Many thanks also to my family for their patience and support. Look, I finally made it!

And most importantly, the biggest thank you belongs to Krischan!

Erklärung

Ich versichere, dass ich die von mir vorgelegte Dissertation selbständig angefertigt, die benutzten Quellen und Hilfsmittel vollständig angegeben und die Stellen der Arbeit − einschließlich Tabellen, Karten und Abbildungen −, die anderen Werken im Wortlaut oder dem Sinn nach entnommen sind, in jedem Einzelfall als Entlehnung kenntlich gemacht habe; dass diese Dissertation noch keiner anderen Fakultät oder Universität zur Prüfung vorgelegen hat; dass sie − abgesehen von unten angegebenen Teilpublikationen − noch nicht veröffentlicht worden ist, sowie, dass ich eine solche Veröffentlichung vor Abschluss des Promotionsverfahrens nicht vornehmen werde. Die Bestimmungen der Promotionsordnung sind mir bekannt. Die von mir vorgelegte Dissertation ist von Prof. Dr. Carsten Münker betreut worden.

Nachfolgend genannter Teil wurde zur Publikation eingereicht:

Zippmann V., Wombacher F., Ertel-Ingrisch W., Dingwell D. B., Wennrich V., Heuser A., Münker C. *Cadmium stable isotope fractionation during evaporation and recondensation at atmospheric pressure.* Geochimica et Cosmochimica Acta (submitted)

Datum Unterschrift

Lebenslauf

Persönliche Daten

Name:	Victoria Elisabeth Zippmann
Adresse:	[redacted]
Mobil:	[redacted]
E-Mail:	v.zippmann@outlook.com

Nationalität:	österreichisch
Geburtsdatum:	[redacted]

Sprachen:	deutsch - Muttersprache englisch - fließend

Akademische Laufbahn

seit 10/2012	Geowissenschaften, Promotion Universität Köln
10/2005 – 04/2012	Mineralogie, Abgeschlossen mit Diplom Universität Köln
10/2004 – 03/2005	Russisch für Dolmetscher Karl-Franzens-Universität Graz

Schulische Laufbahn

1996 – 2004	Bundesrealgymnasium Mattersburg Abgeschlossen mit Matura (Allgemeine Hochschulreife Österreich)